Synthetic Aperture Radar Interferometry for Natural Disaster and Reservoir Monitoring

Mokhamad Yusup Nur Khakim

2012

Abstract

This study focuses on the capabilities of a SAR interferometry as a stand-alone technique to detect and quantify ground surface deformations. In order to achieve the accuracy of the deformation estimations from the technique comparable to traditional geodetic measurements, such as GPS and leveling surveys, we had to process carefully in each step of the SAR interferometry processing with considerations of the qualities. In this dissertation, two methods presented in order to estimate the deformations are (1) two-pass differential SAR interferometry (DInSAR) and (2) interefrometric point target analysis (IPTA). For case studies, we applied the technique to monitor (i) land subsidence in Bandung Basin, Indonesia and (ii) surface heave at oil-sand field at Hangingstone, Canada. From (ii) surface heave due to steam assisted gravity drainage (SAGD) at Hangingstone area, we further estimated distribution of reservoir deformation using geomechanical inversion.

Since the subsidence has occurred in most of urban regions, differential SAR interferometry (DInSAR) technique is suitable to estimate the subsidence in Bandung Basin for long time duration between two observations. We generated 32 interferograms from 21 ascending SAR images obtained from ALOS/PALSAR over a period from January 1, 2007 to March 3, 2011. In order to remove topographic phase, we used the 3-arc-second Shuttle Radar Topography Mission (SRTM) digital elevation model (DEM). A detail DInSAR processing to estimate and describe the land subsidence history with time series of interferograms is presented in this dissertation. However, an individual differential interferogram may be deteriorated by atmospheric phase. By cross-comparison of the interferograms, a presence of atmospheric signals can be identified by their specific shapes and magnitude. Assuming the displacements are stationary, we suppressed the noises and estimated the subsidence rate by averaging the interferograms which is the so-called interferogram stacking technique. However, several surface displacements may be not only linear but also nonlinear. The nonlinear displacements may be due to several

factors, such as a variation of production rates and seasonal aquifer recharge and a tectonic activity. In order to estimate the nonlinear displacement IPTA method is adopted. Using IPTA topographic phase, atmospheric phase and phase noise were estimated and suppressed from interferogram phase. Total displacement is the summation of the linear and nonlinear displacement. The displacement rate was also estimated from the linear displacement history. The maximum subsidence of about 12 cm per year which occurred in Cimahi city can successfully be identified by using both DInSAR and IPTA methods. The subsidence pattern and subsidence rate maps are not always correlated with the production well distribution and aquifer zoning maps due to geological structure of investigated area. The largest land subsidence has occurred in industrial regions and it can also be seen from the aquifer zoning map, which the region has experienced damage in the aquifer system. The seasonal characteristic of the land subsidence in Bandung has successfully been investigated based on the nonlinear component of displacement. Results show great potential of differential SAR interferometry to comprehensively monitor the process in developing groundwater in Bandung Basin.

The **s**urface heave rate at oil sands field due to steam assisted gravity drainage (SAGD) has also been estimated by stacking unwrapped differential SAR interferometry. For the case of Hangingstone area in the lookup table creation for geocoding, the refinement of the lookup table was different from that of Bandung Basin area. Commonly, InSAR processing for the refinement of lookup table is enough to make use of a simulated SAR intensity image in order to obtain positioning accuracies at sub-pixel level in the automatic registration with the actual SAR image. For Bandung Basin area, the simulated SAR intensity was reasonably used to obtain at the sub-pixel accuracy. However, the topography of Hangingstone area is poor. It can make the simulated SAR intensity generated from a SRTM DEM not well working used to improve the accuracy up to sub-pixel due to a high decorrelation between both images (SAR intensity from PALSAR and simulated SAR intensity from SRTM DEM). So, we used a Landsat-7 Enhanced Thematic Mapper Plus (ETM+) intensity image instead of that from DEM for coregistration with PALSAR intensity image in order to obtain a high accuracy result. A comparison of three adaptive filtering methods has been further conducted to choose

the suitable method for optimally reducing noises over differential interferograms. Once quadratic phase is removed from unwrapped differential interferogram, the stacking is performed to estimate the surface heave rate which the stacking at the same time also removes atmospheric effects. Finally, the surface heave rate estimate is validated with the result of the network of 54 monument surveys. Our result is in good agreement with the network surveys.

The surface heave induced by SAGD process has valuable information about the dynamic reservoir. We have therefore made use of the heave map to estimate distribution of reservoir deformations and reservoir volume change in the oil sand reservoir by means of an inversion technique. As a geomechanical inversion, we propose two-step inversion scheme based on a tensional rectangular dislocation model. In the first step of the inversion, we use genetic algorithms to estimate the depth and rough deformation of the reservoir. The depth of the oil sand reservoir estimated from the inversion is well consistent with depth of injected point (297 m). Secondly, the least square inversion with the penalty function and smoothing factor is used to efficiently invert the distribution of reservoir deformation and volume change from the surface uplift data. These results demonstrate that the InSAR technology is useful to provide ground surface deformations and accurately monitor reservoir deformation using inversion techniques.

Acknowledgements

First, I would like to express my deepest and most sincere gratitude to my supervisor Professor Toshifumi Matsuoka for their scientific supervision, constant encouragement, precious advices, and patient guidance during my research. I am also grateful to Associate Professor Yamada Yasuhiro and Assistant Professor Takeshi Tsuji for great deal suggestions, valuable information and helps.

I also would like to extend my sincerest thanks to dissertation committee members, Professor Masayuki Tamura and Professor Katsuaki Koike, for their advice and efforts in reviewing this dissertation.

I would like to thank laboratory secretary Miss Kana Moriyama and Miss Daito for kind helps and cooperation. I also need to thank all lab students who create a good atmosphere in the laboratory.

I would like to acknowledge Directorate General of Higher Education Indonesia for the financial support to conduct my study in Kyoto University. My thanks also go to Sriwijaya Univeristy for the permission to carry out studying in Kyoto University and kind cooperation during my study.

I would also like to acknowledge the Earth Remote Sensing Data Analysis Center (ERSDAC) for providing ALOS PALSAR data.

Last but not least, I thank to my family for right from the bottom of my heart, my parents for their love, encouragement and understanding during my study.

Contents

List of Figures

List of Tables

Chapter 1

Introduction

1.1 Background

Nowadays, it is generally appreciated that the InSAR technique in geophysical applications is an appealing and powerful tool for mapping the dynamic change in Earth's topography. The InSAR technique uses the information contained in the phase of SAR images. A SAR interferogram is a superposition of information on the topography, the surface deformation between the two SAR acquisitions, the atmospheric propagation delays, and various noises (Tarayre and Massonnet, 1996). The so-called differential InSAR technique (D-InSAR), which subtracts the topographic phase from the interferogram, is an emerged technique for detection and mapping of surface displacements over large temporal and spatial scales at the accuracy of centimeter or even millimeter level. Other advantages of InSAR are the SAR data availability and competitive cost. This is of great importance for monitoring surface displacements described below.

Land subsidence, lowering of the land surface by groundwater pumping, affects an aggregate area of about 2300 km2 in the Bandung Basin, Indonesia. The subsidence poses severe problems including damage to building and infrastructures. The excessive groundwater extraction can also cause aquifer having a permanently-reduced capacity to hold water (i.e a reservoir compaction). A Global Positioning System (GPS) survey, which is a traditional geodetic technique for land surface leveling with accuracy in order of millimeter, was conducted to investigate the characteristics of Bandung subsidence (Abidin et al., 2008). Abidin et al. (2008) also estimated the subsidence by using InSAR technique. However, they focused on GPS measurements and did not explore in detail the capability of InSAR to estimate the rate of the subsidence. They

estimate the Bandung subsidence from InSAR during the period between June 2006 and March 2007.

Otherwise, surface displacement in term of uplift can occur due to fluid injection in reservoir. SAGD (steam-assisted gravity drainage) is one of enhanced oil recovery (EOR) technique that has been applied to revolutionize the economic recovery of heavy oil and bitumen from the immense oil sands deposits in the Hangingstone field, Canada. This field has about 2.5 trillion barrels of oil in place. With steam injection, reservoir pressures and temperatures rise. These elevated pressure and temperatures alter the rock stresses sufficiently to cause dilatation within and beyond the growing steam chamber which can be observed at surface as displacements. From 1999 to 2008, conventional geodetic measurements, i.e. the network of 54 monuments surveys were carried out to investigate surface heaves in order to map the deformation due to SAGD process at Hangingstone's oil sand field (JACOS 2009). Even though the GPS surveys can provide subsidence information with high accuracy, it is costly, time consuming and sparse spatial resolution for a large and inaccessible area. Of course, both GPS surveys and an InSAR technique have advantages and disadvantages. Therefore, in order to optimize a combination of an accurate result and a cost-effective technique for the land subsidence monitoring it should be considered the InSAR technique as main tool, otherwise GPS surveys is as a validity data.

1.2 Objectives and Methodology

Although InSAR technique is a powerful tool, it has also limitations due to noise, which is caused by decorrelation effects and water vapor in the atmosphere. Commonly, an InSAR processing for a refinement of lookup table is enough to make use of a simulated SAR intensity image in order to obtain positioning accuracies at sub-pixel level in the automatic registration with the actual SAR image. However, one of our study areas has very little topographic relief so that the coregistration becomes not reasonable. It make a simulated SAR intensity generated from a SRTM DEM not well working used to improve the accuracy up to sub-pixel due to a high decorrelation between both images (SAR intensity from PALSAR and simulated SAR intensity from SRTM DEM). In this paper we present how to solve this problem so that the refinement of lookup table significantly improves the accuracy.

Moreover, a main problem in the InSAR processing is presence of residues in the phase unwrapping process. The residues are caused by noise over an interferogram. Goldstein and Werner (1998), Baran *et al*. (2003), and Li *et al*. (2006) developed the filtering method to reduce noise. So far, no literature presents comparison among these filtering methods based on the ability of the filter in reducing residues. Therefore, we need to compare the filtering methods before unwrapping differential interferogram phase, in order to choose a suitable method for optimally reducing noises over differential interferograms. We have also used other statistical parameters, such as sum of the phase difference (SPD) and normalized standard deviation (NSD), to examine these filtering methods for the interferograms.

Another factor which can limit the accuracy of the deformation estimated from individual differential SAR interferometry (DInSAR) is caused by the atmospheric path delay effect. This atmospheric effect is related to the water vapor which causes errors in estimate displacements. We reduce the atmospheric effect using a stacking technique of unwrapped differential SAR interferogram and an interferometric point target analysis (IPTA). By using IPTA we have also estimate the linear and nonlinear displacements.

Because the ground deformation (subsidence or uplift) is induced by reservoir compaction (or expansion), the surface deformation has valuable information about the dynamic reservoir and is most likely to occur in the production of hydrocarbon even if the reservoir is in kilometers deep. Characterization of the surface deformation sources based on the InSAR measurements has therefore become major importance in reservoir monitoring activity, such as EOR, carbon dioxide capture and storage (CCS) project. The amplitude and the rate of surface deformation are key parameters for optimum economical production and for minimum environmental impact. One of the most common applications of these measurements is to numerically or analytically simulate the source of deformation.

There are some source models to be able to simulate the surface deformation, such as the point source (Mogi 1958), the ellipsoidal source (Yang *et al*. 1988), and the rectangular source (Okada 1985). The first two source types are commonly used for volcano and reservoir modeling (Delaney and McTigue 1994; Opplier *et al*. 2005; Fialko and Simons 2000). Meanwhile the last is mostly used for volcanic and earthquake events (Anderssohn *et al*. 2009; Jonsson *et al*. 2002). A pure volumetric

dilation source gives rise to a distribution of monopolar vertical displacement, whereas a shear distortion gives rise to a dipole (Dusseault and Collins 2008). For reasonably well-constrained cases, such as a single flat-flying reservoir, the surface deformation can be inverted to give a distribution of volume changes at the depth of the reservoir horizon. In this study, we propose a two-step inversion from the surface uplift map obtained by InSAR measurement to estimate the distribution of reservoir deformations and reservoir volume change rates where the oil sand reservoir is undergoing steam injection, Steam Assisted Gravity Drainage (SAGD). In the first step, we estimate the geometry of reservoir deformation by inverting the uplift map measured by InSAR adopting Okada source model using genetic algorithm (GA) inversion. In the second step, we use least square method to obtain reservoir deformation, thus reservoir volume changes can then be calculated.

1.3 Dissertation Content and Organization

This dissertation presents the three main scientific chapters along this introduction, literature overview, and general conclusion. The chapters are:

Chapter 1: introduces general descriptions of this study including main topics related to excessive groundwater extraction in Bandung Basin, Indonesia and steam injection using SAGD technique for EOR at the Hangingstone field, Canada, along with this description of dissertation content and organization.

Chapter 2: describes the history of SAR interferometry. In addition, overview of the principle of SAR interferometry is also described.

Chapter 3: presents a case study of land subsidence monitoring in Bandung Basin, Indonesia using differential interferogram. This chapter describes the differential InSAR processing and the interferometric point target analysis (IPTA) for generating time-series subsidence in Bandung Basin. In order to refine a geocoding look-up table, we used a simulated SAR intensity from DEM and real SAR intensity. The accuracy of the registration between the simulated and real SAR intensities shows that the refinement of the look-up table worked well. Beside the time-series subsidence, we also estimated the rate of the subsidence by using the stacking technique of differential interferograms and the interferometric point target analysis. The displacement history including the linear and nonlinear components has also estimated by using the IPTA.

For subsidence analysis we compared the subsidence map to the production well distribution and the aquifer zoning map.

Chapter 4: presents a case study of surface heave monitoring at oil sands field by stacking differential SAR interferometry. In this chapter we examined and compared some filtering methods to choice the best method and filtering parameters to reduce noise phase from differential interferograms. In addition, we introduced the method to refine the geocoding look-up table using Landsat ETM+ instead of the simulated SAR intensity image from DEM. In order to estimate the rate of surface uplift we also applied the interferogram stacking technique which also reduced the atmospheric effects.

Chapter 5: presents the inversion scheme for monitoring the reservoir deformation and volume change rate based on the ground surface deformation obtained from satellite-based radar interferometry data. The surface deformation has been estimated using technique described in Chapter 4. The proposed inversion scheme is used two steps which consist of a genetic algoritm and a least square inversion for first and second step, respectively

Chapter 6: describes summary of this study and future work.

Chapter 2

Literature Overview

2.1 History of SAR Interferometry

Radio detection and ranging (radar) refers to a technique as well as an instrument. The radar instrument emits electromagnetic pulses in the radio and microwave regime and detects the reflections of these pulses from objects in its line of sight. The radar technique uses the two-way travel time of the pulse to determine the range to the detected object and its backscatter intensity to infer physical quantities such as size or surface roughness. Radar has been employed for electronic observing since World War II and ever since has experienced a substantial technique boost. The technical development as well as experiences over many years soon provided the opportunity to construct devices supplying planae images of areas, for example the Synthetic Aperture Radar (SAR).

Although the technology mainly gained momentum through military applications in those early years, civil and scientific applications arose quickly afterward. In particular radio astronomy profited from the advances in technology. Earth-based radars proved ideal for studying celestial bodies such as the Moon, Venus, Mars, and the Sun. Rogers and Ingalls (1969) was the first to use SAR interferometry (InSAR) for observation of the surface of Venus and the Moon from its configurations using antennas on the Earth's surface. For topographic mapping, synthetic aperture radar was the first introduced by Graham (1974). Zebker and Goldstein (1986) presented the first practical results of observations with airborne radar. Goldstein *et al.* (1988) was the first to apply InSAR technique to the spaceborne observations to generate highly accurate digital elevation model (DEM) of the Earth's surface using the SEASAT-A L-band SAR system. With the launch of ERS-1 (1991), JERS-1 (1992), and RADARSAT (1995), spaceborne InSAR study has increased dramatically. With the launch of ERS-2 in 1995, the feasibility of spaceborne SAR interferometry has been greatly improved by the use

of ERS-1 and ERS-2 in the tandem mission that can provide interferometric data at only one-day separation (Duchossois and Martin, 1995).

Technical refinement of InSAR for the generation of Digital Elevation Model (DEM) can be found in Madsen *et al.* (1993) and Zebker *et al.* (1994b). The concept of differential SAR Interferometry (DInSAR) was established by Gabriel *et al.* (1989). Massonnet *et al.* (1993) used a pre-existing DEM to remove the topographic phase from interferogram and retrieved the co-seismic displacement field of the Landers earthquake in California. Zebker *et al.* (1994a) used three-pass DInSAR configurations to remove directly the topographic phase without use of the reference DEM. The use of coherence image for surface stability study is a relatively recent study area in fast development (Massonnet *et al.*, 1995; Hagberg *et al.*, 1995; Rosen *et al.*, 1996; Liu *et al.*, 1997).

2.2 Real-aperture imaging radar systems

Unlike the cameras used to make vertical aerial photographs, imaging radar systems point to the side rather than straight down so the arrival path of the radar signal is oblique to the surface being imaged. This is necessary to better distinguish among targets located at different distances from the radar. Side-looking radar systems are classified as either real-aperture (called SLAR for sidelooking airborne radar or SLR for side-looking radar) or synthetic-aperture radar (SAR). SLR imaging systems use a long, straight antenna mounted on a moving platform, usually an aircraft or satellite, with the antenna's longitudinal axis parallel to the flight path (Figure 2.1). The antenna emits microwave pulses in a beam directed perpendicular to the flight path and obliquely downward toward the surface of the Earth. These pulses strike the surface along a narrow swath and are scattered, usually in many directions, including the direction back to the radar. The antenna captures a very small fraction of the energy it transmits, typically less than 0.0001%, from the returning pulse echoes. The echoes arrive at the antenna at different times, depending mainly on the distance from the antenna to countless natural reflectors on the ground. By keeping track of the arrival times, an SLR profiles its distance from the ground in the direction perpendicular to the flight path (i.e., the cross-track or range direction). Motion of the aircraft or satellite advances the profile in the direction parallel to the flight path (i.e., the along-track or azimuth direction). By overlapping successive swaths, a large area on the ground can be mapped at a resolution

of a few tens of meters (Curlander and McDonough, 1991; Madsen and Zebker, 1998; Hanssen, 2002). The resulting images contain information about surface slopes (i.e., topography) and other factors that influence radar reflectivity, including roughness and moisture content. The dimensions of the antenna determine the spread of the radar beam and thus the size of its footprint on the ground. The angular beam width is $\beta_r \approx \lambda/D$ in the range direction and $\beta_a \approx \lambda/L$ in the azimuth direction, where D and L are the width and length of the antenna, respectively. The corresponding dimensions of the antenna footprint are:

$$W_r \approx \frac{\lambda R_m}{D \cos\theta_m} \tag{2.1}$$

and

$$W_a \approx \frac{\lambda R_m}{L} \tag{2.2}$$

where W_r is the width of the footprint in the range direction (i.e., the swath width), W_a is the width of the footprint in the azimuth direction, λ is the wavelength of the radar, R_m is the slant range from the antenna to the middle of the footprint, and θ_m is the incidence angle at the middle of the footprint (Figure 2.1).

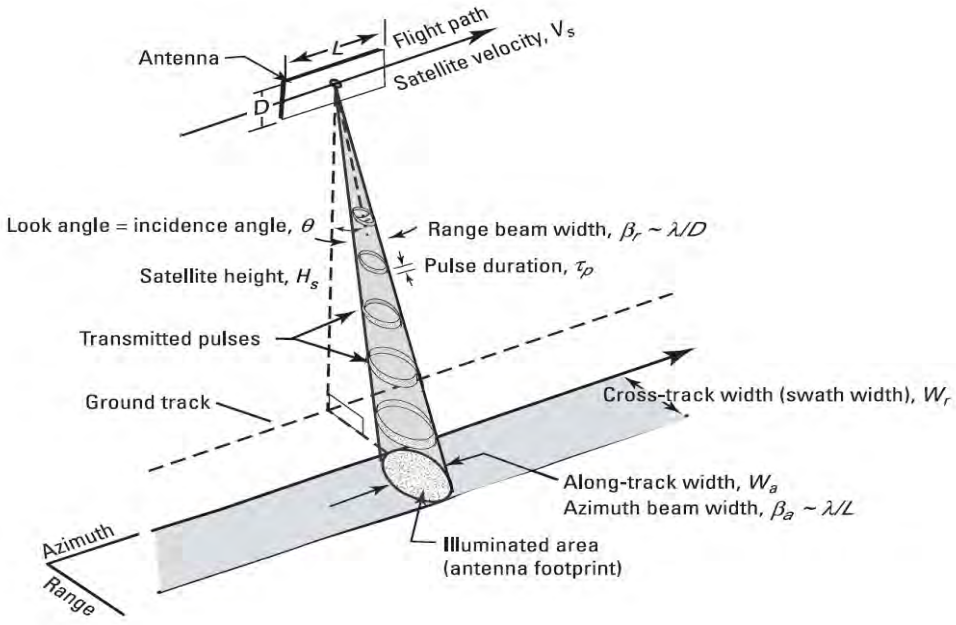

Figure 2.1. Scanning configuration for a right-looking radar

Ground resolution of real aperture radar. The spatial resolution of an imaging radar system depends on different factors in the range and azimuth directions. Intuitively, the range resolution must depend both on the pulse duration and then incidence angle of the radar beam. In the first case, a shorter pulse duration provides a finer probe of the distance from antenna to ground, so range resolution should improve at shorter pulse durations. The situation is akin to measuring the width of this page using a ruler marked off either in millimeters or centimeters − the more-closely-spaced markings give better precision, for the same reason that short-duration radar pulses allow better range resolution than long-duration ones. The angle of incidence of the incoming radar signal must also play a role, because a vertically directed radar would receive return echoes from all objects in the scene at nearly the same time, making it very difficult to distinguish among them. At the other extreme, distances across the ground swath for an SLR with a high angle of incidence (i.e., a grazing beam) would differ by a large amount so the range resolution would be good, but the return signal strength would be poor because most of the signal would be scattered forward away from the radar. The ERS satellites accommodate this tradeoff with a fixed incidence angle of 23^{o} at the middle of the swath. The radar aboard the Canadian RADARSAT-1 satellite can be steered electronically to produce incidence angles from 10 to 59 at the middle of the swath. Two objects can be distinguished in the range direction only if the leading edge of the pulse echo from the more distant object arrives at the antenna later than the trailing edge of the echo from the nearer object. In other words, the two slant ranges must differ by at least half of the pulse length for the objects to be resolvable (Figure 2.2):

$$\Delta R_s \geq \frac{c\tau_p}{2} \tag{2.3}$$

where_Rs is the slant-range difference, c is the speed of light, and τ_p is the pulse duration. Otherwise, theechoes would arrive at the antenna at the end of their round trip separated by less than one pulse length and be indistinguishable. This constraint leads to the following expression for the theoretical groundrange resolution as a function of pulse duration and incidence angle:

$$\Delta R_g = \frac{c\tau_p}{2\sin\theta} \tag{2.4}$$

where ΔR_g is the ground-range resolution and θ is the incidence angle at a particular ground range. The best theoretical ground-range resolution would be produced by a combination of extremely short pulse duration and large incidence angle. For example, an X-band radar operating at a frequency of 10GHz with a pulse duration of 10^{-8} s at an incidence angle of 60^{o} would have a theoretical ground-range resolution of 1.7 m. Unfortunately, there is a catch. The quality of the radar image depends on the ratio of the return signal strength to the ambient system noise. The greater the signalto- noise ratio, the more fidelity the radar image will have. To achieve meter-scale resolution over typical terrain, the pulse duration would have to be too short to generate enough energy to achieve an adequate signal-to-noise ratio. High-incidence angles pose the same problem. For the case of grazing incidence, forward scattering dominates and the return from back scattering is negligible. In other words, engineering constraints and the principles of wave scattering preclude the realization of a shortpulse-duration, high-incidence-angle SLR.

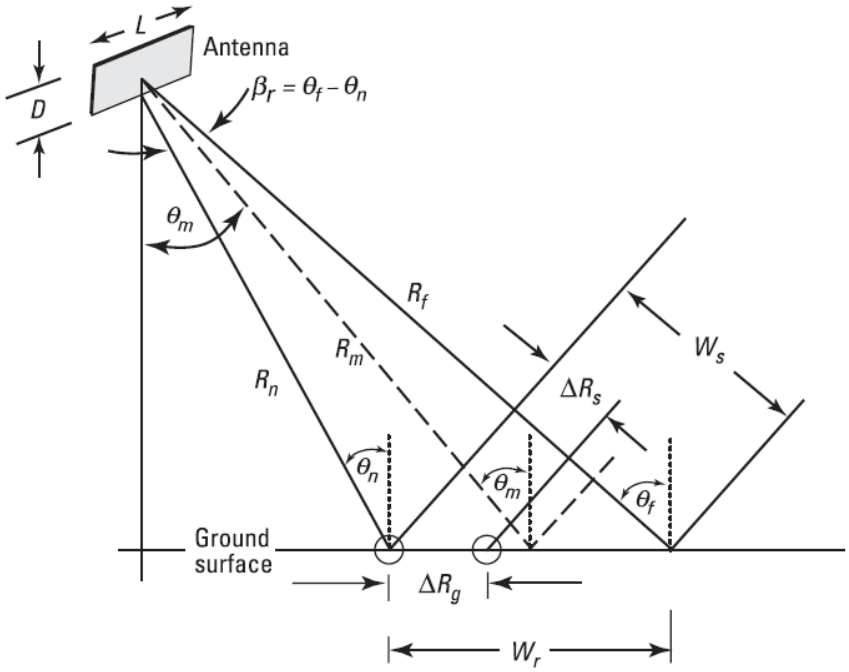

Figure 2.2. The swath width W_r for a real-aperture radar is determined by the wavelength λ, the antenna width D, the slant range at the middle of the antenna footprint $R_{m,}$ and the incidence angle at the middle of the footprint θ_m. The ground-range resolution ΔR_g is related to the pulse duration τ_p and the incidence angle. R_n and R_f are the slant ranges at near range and far range, respectively, and β_r is the angular beam width in the range direction. See text for details. After Olmsted (1993).

This difficulty can be overcome, however, by using a technique known as range compression together with a type of signal processing called matched filtering. A thorough description of these techniques can be found in Curlander and McDonough (1991). For our purposes, suffice it to say that the approach is based on transmitting and receiving not a single frequency but a spread of frequencies in the microwave range. The goal is to correlate specific outgoing and incoming pulses – a daunting task when one considers that a typical X-band radar operates at a frequency of 10 billion cycles per second with a pulse duration of ten one-billionths of a second! To solve this problem, radar engineers use some nifty mathematics and a special kind of pulse called a chirp. The frequency of a typical radar chirp increases linearly with time, say from 9.99 GHz to 10.01 GHz. In the auditory frequency range, such a pulse would sound like a chirp – hence the term. When the returned echo of a linearly frequency modulated pulse (a chirp) is correlated with the known transmitted signal, the autocorrelation function is nearly zero except for a narrow spike that corresponds to the round trip travel time of the pulse. The echo is thus 'compressed' into a form that can be readily identified with an electronic match filter tuned to the appropriate range of travel times. With these techniques it is possible to achieve a ground-range resolution given by:

$$\Delta R_g = \frac{c}{2B\sin\theta} \tag{2.5}$$

where B is the frequency bandwidth of the transmitted radar pulse. The range resolution can be improved by increasing the frequency bandwidth of the pulse or the incidence angle, as long as the signal-to-noise ratio remains high enough. Comparing the ground resolution without range compression (2.4) with that after range compression (2.5), we see that the improvement in ground-range resolution is equal to $\tau_p \; x \; B$, which is commonly called the pulse compression ratio. Nominally, the ground range resolution ΔR_g is slightly larger than the sampling spacing $c/(2f_s \sin\theta)$, where f_s is the sampling frequency in the range direction.

We can see that the range resolution is controlled by the type of frequency modulated waveform and the way in which the returned signal is compressed. Both SLR and SAR systems resolve targets in the range direction in the same way. What distinguishes SLR from SAR is resolution in the azimuth direction (Curlander and McDonough, 1991).

In the azimuth direction, two objects at the same range can only be distinguished if they are not both illuminated by the beam at the same time. Therefore, the best azimuth resolution attainable with a real-aperture radar is, from (2.2) (Curlander and McDonough, 1991):

$$\Delta A_g = W_a = \frac{\lambda R_m}{L} \tag{2.6}$$

where ΔA_g is the ground-azimuth resolution, akin to the ground-range resolution ΔR_g in (2.5). A 3m long antenna operating at a wavelength of 5.6 cm (Cband) on an aircraft flying 1,400m above terrain with a beam incidence angle $\theta_m = 30^o$ (R_m ~ 1,600 m) has an azimuth resolution of about 30 m. The same C-band SLR operated from orbit at a slant range of 850km from terrain would produce an azimuth resolution of about 16 km, which is much too coarse for most applications. To reduce this number to 30m would require an antenna about 1.6km long, which is not likely to be deployed in orbit anytime soon. The solution to this dilemma lies in conjuring up a huge synthetic antenna by taking advantage of the along-track motion of a real antenna and using the Doppler effect to identify signals reflected from specificnparts of the antenna footprint.

2.3 Synthetic aperture radar (SAR)

Carl A. Wiley (1965) was the first to realize that the frequency spread in the echo signal produced by the Doppler effect could be used to synthesize a much larger antenna aperture than is achievable with real aperture radars (hence the term *synthetic-aperture radar*, or SAR) (Figure 2.3). This breakthrough led to dramatic improvement in the resolution of SLRs, paving the way for satellite-borne SARs with meter-scale resolution over swath widths of 50−150 km.

Relative motion between an observer and a source of waves causes a frequency shift known as the Doppler effect. When a source emitting waves with frequency *f* approaches or recedes from the observer at velocity *v*, the observed frequency *f'* is:

$$f' = \sqrt{\frac{1+(v/c)}{1-(v/c)}} \times f \tag{2.7}$$

where c is the speed of light and v is positive for an approaching source and negative for a receding source. Thus, an approaching source exhibits a higher frequency and a receding source a lower frequency than the frequency emitted by the source. This effect

is familiar to anyone who has listened to a passing train whistle or emergency siren, which decreases in pitch as its velocity relative to the observer changes from positive (approaching) to negative (receding).

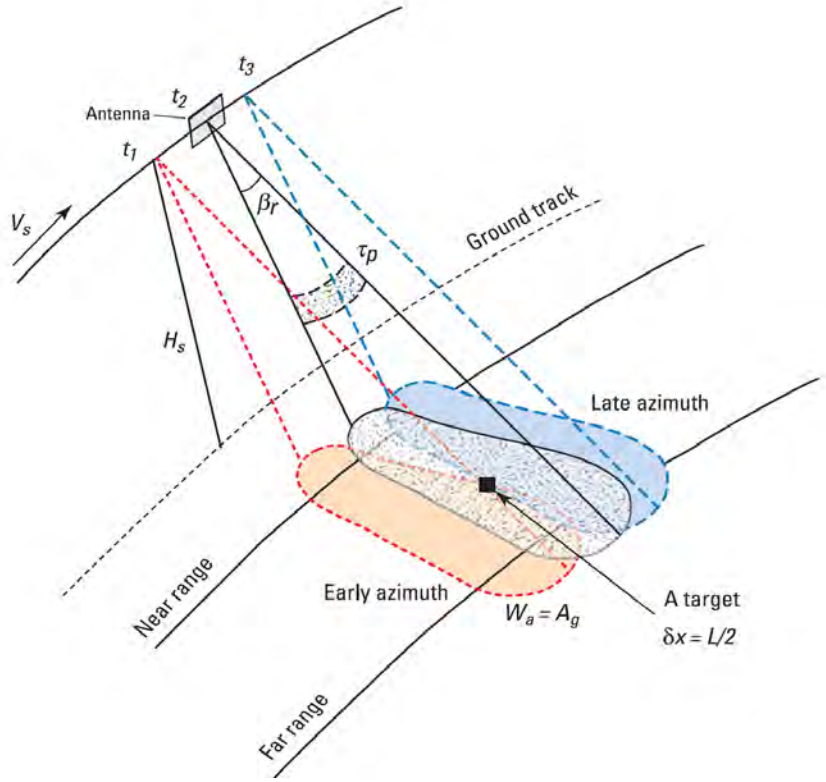

Figure 2.3. At any time t_2, a real aperture radar of length L illuminates a footprint on the ground of dimension $W_a = \lambda R_m / L$ in the azimuth direction. A synthetic aperture radar takes advantage of the fact that the same target is illuminate continuously and remains in the footprint from time t_1 to t_3 as the radar travels along its flight path at velocity V_s. All of these echoes are used to synthesize a much longer antenna with an aimuth resolution improved from $A_g = W_a$ to $\delta_x \sim L/2$ (Curlander and McDonough, 1991).

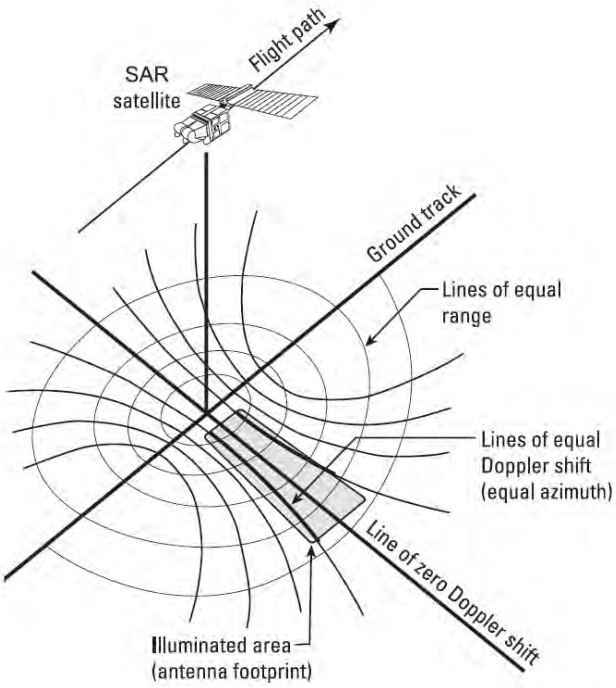

Figure 2.4. SAR images are focused by assigning range and azimuth coordinates to the echoes received from each resolution cell on the ground, which are delinated by the intersections of lines of equal range and lines Doppler shift.

How can we take advantage of this classical principle of wave propagation to transform a small real antenna into a huge synthetic one? Notice from Figure 2.3 that targets in the radar illumination footprint which are located at the same range but different azimuths subtend slightly different angles with respect to the look direction of the antenna. As a result, they have slightly different velocities at any given moment relative to the antenna. At the leading edge of the footprint the radar is approaching the target, while at the trailing edge it is receding. Therefore, the signal echoed from each target will have its frequency shifted a different amount from the transmitted frequency. Recall that the limitation on azimuth resolution for real-aperture radars derives from the requirement that, to be resolvable, two objects at the same range can not be within the beam’s footprint at the same time. The Doppler effect provides a means of distinguishing two such objects, because the antenna will see a return from each that is frequency shifted by an amount that can be attributed to a specific azimuth within the antenna footprint. The procedure is known as azimuth compression. Through the wonders of range and azimuth compression, each of myriad echoes from resolution cells throughout the footprint can be assigned unique coordinates in both range and azimuth to produce a ‘focused’ SAR image (Figure 2.4).

As the radar antenna moves along its flight path its velocity relative to points on the ground changes, inducing a corresponding Doppler shift in the frequency of the echoes (Curlander and McDonough, 1991, p. 17):

$$f_d = \frac{2 \times (v_s \sin \varphi)}{\lambda} \approx \frac{2 v_s x}{\lambda R} \tag{2.8}$$

where f_d is the Doppler shift, v_s is the antenna's velocity relative to a point on the ground, φ is the angle from a line perpendicular to the ground track and is defined on the plane constituted by the flight direction and the point on the ground, x is the alongtrack distance measured from the point of closest approach, R is the slant range, and the factor of 2 arises from the two-way travel time (Figure 2.5). Thus, the Doppler frequency of the echoes can be used to determine the along-track coordinate (azimuth) of a particular echo sample:

$$x = \frac{\lambda R f_d}{2 v_s} \tag{2.9}$$

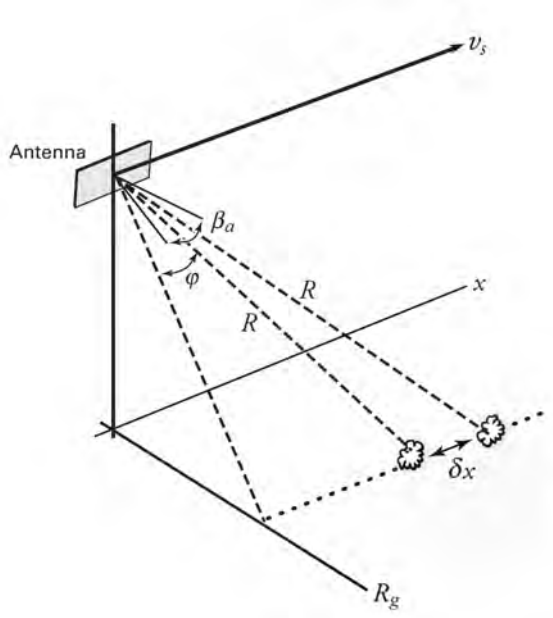

Figure 2.5. Azimuth resolution of a synthetic-aperture radar, after Curlander and McDonough (1991).

As the target passes through the antenna beam, it exhibits a constantly changing Doppler shift that is directly related to the position of the radar and the azimuth position of the target. For each azimuth position there is a unique Doppler history. So the echoes from multiple targets at the same range that are illuminated simultaneously by the beam

can be discriminated on the basis of their Doppler shifts. The focused azimuth resolution δx of a SAR depends on the precision of the Doppler shift measurement:

$$\delta x = \left(\frac{\lambda R}{2 v_s} \right) \times \delta f_d \tag{2.10}$$

where δf_d, the measurement resolution of the Doppler shift, is nominally the inverse of the time span Δt, for which the target remains illuminated (Figure 2.3):

$$\Delta t = t_3 - t_1 = \frac{A_g}{v_s} = \frac{R\lambda}{L v_s} \tag{2.11}$$

Therefore, the azimuth resolution of a focused SAR image is approximately (Curlander and McDonough, 1991, p. 20):

$$\delta x = \left(\frac{\lambda R}{2 v_s} \right) \times \left(\frac{L v_s}{R \lambda} \right) = \frac{L}{2} \tag{2.12}$$

This simple result seems surprising because it shows that the azimuth resolution of a SAR improves as the antenna size decreases, which is opposite to the rule for a real-aperture radar. The smaller, the better would seem to be the rule in this case. This seems like good news, but again there is a catch. The same antenna must act both as a transmitter and as a receiver, so it must alternate between transmitting and listening modes. The effective gain of the antenna is proportional to the square of its real aperture, so reducing the antenna size to improve the azimuth resolution produces a tradeoff with the maximum obtainable signal-to-noise ratio (Henderson and Lewis, 1998). A very small antenna might produce excellent azimuth resolution, but with an unacceptably poor signal-to-noise ratio. The determining factor is the pulse repetition interval PRI=1/PRF, where PRF is the pulse repetition frequency, because the difference in time between echoes from the near range $2R_n/c$ and far range $2R_f/c$ must be less than the time between pulses (Figure 2.2):

$$W_s = R_f - R_n \leq \frac{c}{2 \times PRF} \tag{2.13}$$

Otherwise, far-range echoes from one pulse would be confused with near-range echoes from the next. The maximum swath width is therefore:

$$W_g \approx \frac{c}{2 \times PRF \sin\theta} \tag{2.14}$$

Hence, large swath widths require small PRFs.

To focus a SAR image in azimuth, a SAR processor must be able to relate an observed incremental phase change to a specific Doppler frequency. Curlander and McDonough (1991) show that this requires the bandwidth of the Doppler signal $B_d \approx (2\beta_a v_s / \lambda)$ to be less than the PRF. Recalling that $\beta_a \approx (\lambda / L)$ and $\gamma_x = (L/2)$, we can write:

$$\frac{2v_s}{L} = \frac{v_s}{\delta x} < PRF \tag{2.15}$$

So in the time between successive pulses 1/PRF the antenna must travel a distance along its flight path of no more than half its own length L=2. Combining this result with that from the previous paragraph, we see that although the azimuth resolution dx is increased for smaller antennae, smaller antennae require larger pulse repetition frequencies, which reduce the swath width (Wright, 2000, p. 26). These relationships place a lower bound on the size of a practical SAR antenna. Most SAR systems designed for Earth orbit use an antenna 1−4m wide and 10−15m long, with a look angle in the range 10 to 60 degrees to illuminate a footprint of 50−150 km in range by 5−15km in azimuth, producing a single-look ground resolution of 4−10m in azimuth and 10−20m in range.

2.4 SAR Interferometry

SAR interferometry (InSAR) is a signal processing technique that combines two or more SAR images over the same area recorded by radar system onboard satellite platform. InSAR operates on the principle of extracting the phase change between two images over the same area taken from different positions to measure the different in path length. The differences can then be related to important parameters such as terrain height, deformation of the Earth surface and excess atmospheric delay (Goldstein et al., 1988). Figure 2.6 shows illustration of the basic geometrical configuration of InSAR. Both of two radar system S_1 (master) and S_2 (slave) illuminate the same ground patch of the Earth. B is the distance between two antennas, called baseline. θ is the look angle, r_1 and r_2 are slant ranges to a point P on the ground, and α is the angle between baseline and the horizontal.

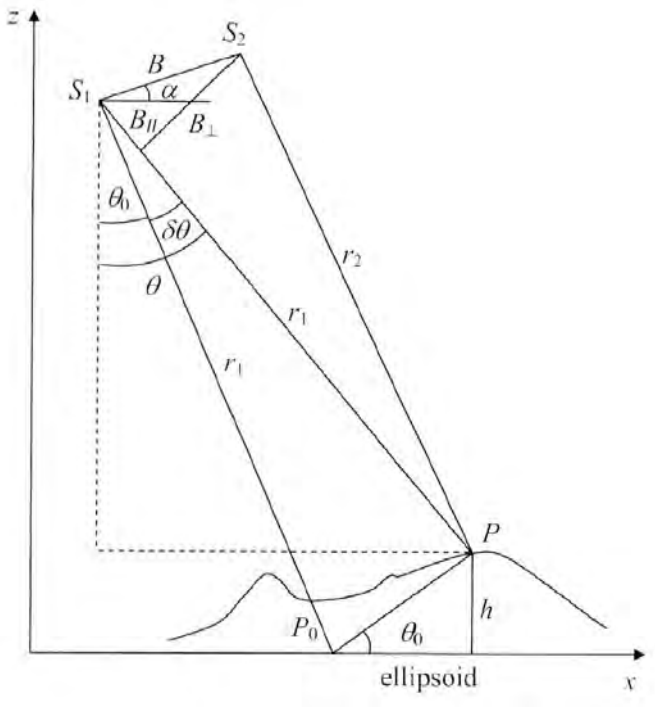

Figure 2.6. Geometrical configuration of InSAR

If no ground movement accurs between two observations, the observed values Φ_1 and Φ_2 in the two images for a resolution cell P can be considered as equal to the sum of the following components: (1) phase delay due to traveled round-trip distance $2r_1$ or $2r_2$ between the target P and the sensor S_1 and S_2, (2) atmospheric variation, (3) scattering due to the interaction of the wave with the multiple ground scatterers within an image resolution element, and (4) additive noise.

Thus the phase from antenna 1 and 2 can be expressed as

$$\Phi_1 = -2\pi\left(\frac{2r_1}{\lambda}\right) + \Phi_{atm1} + \Phi_{scat1} + \Phi_{noise} \tag{2.16}$$

$$\Phi_2 = -2\pi\left(\frac{2r_2}{\lambda}\right) + \Phi_{atm2} + \Phi_{scat2} + \Phi_{noise} \tag{2.17}$$

Suppose the two images have been acquired in the same atmospheric conditions and the backscatters of the objects are also the same, the interferometric phase is written as

$$\Phi = \Phi_1 - \Phi_2 = -\frac{4\pi}{\lambda}(r_1 - r_2) = -\frac{4\pi}{\lambda}\delta r \tag{2.18}$$

where δr is the difference between the range r_1 and r_2.

Applying the law of cosines to a triangle S_1S_2P, we have

$$r_2^2 = r_1^2 + B^2 - 2r_1 B\sin(\theta - \alpha) \tag{2.19}$$

So, we have

$$\sin(\theta - \alpha) = \frac{r_1^2 - r_2^2 + B^2}{2r_1 B} = \frac{(r_1 - r_2)(r_1 + r_2)}{2r_1 B} + \frac{B}{2r_1} \tag{2.20}$$

As $r_1+r_2=2r_1$ and $r1>>B$, we have approximately from (2.20)

$$\delta r = r_1 - r_2 = -B\sin(\theta - \alpha) \tag{2.21}$$

Then the equation (2.18) for repeat pass become

$$\phi = -\frac{4\pi}{\lambda} B\sin(\theta - \alpha) \tag{2.22}$$

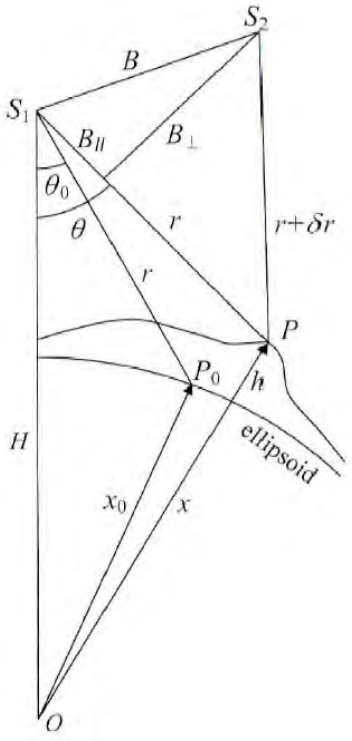

Figure 2.7. SAR geometry related to the reference ellipsoid

Applying the law of cosines to a triangle S_1PO in Figure 2.7, the look angle θ to a point on the ground surface is expressed as

$$\cos\theta = \frac{H^2 + r^2 - x^2}{2rH} \tag{2.23}$$

Where r is the range to the point *P*, and *H* and *x* are the distance of the satellite and the point *P* from the center of the Earth *O* respectively. To see the relation between the

interferometric phase and the local topography, let us consider a point P_0 which is located at the same range as the point on the reference ellipsoid and would appear in the same position on the SAR image from a satellite S_1 (Figure3). Let x_0 be the local Earth radius of the reference ellipsoid, θ_0 be the look angle. Then using the law of cosines, we find

$$\cos\theta_0 = \frac{H^2 + r^2 - x_0^2}{2rH} \tag{2.24}$$

Using (2.24) and (2.22) we can derive the interferometric phase ϕ_0 from the point P_0 called the flat Earth phase, as follows

$$\phi_0 = -\frac{4\pi}{\lambda} B \sin(\theta_0 - \alpha) \tag{2.25}$$

The actual distance x is usually greater than the radius of the reference ellipsoid x_0. The difference x-x_0 provides the geometric elevation. The phase due to the actual topography $\phi(x)$ can be expanded in a Taylor Series about x_0

$$\phi(x) = \phi(x_0) + \left(\frac{\partial\phi}{\partial x}\right)_0 (x - x_0) + \frac{1}{2}\left(\frac{\partial^2\phi}{\partial x^2}\right)_0 (x - x_0)^2 + \ldots \tag{2.26}$$

where $\phi(x_0)$ is the flat Earth phase ϕ_0 given by (2.25). Because the second derivative is very small, $\phi(x)$ is well approximately by the first two terms in the series.

$$\phi(x) \approx \phi(x_0) + \left(\frac{\partial\phi}{\partial x}\right)_0 (x - x_0) \tag{2.27}$$

The first term is the flat Earth phase ϕ_0 given by equation (2.25), and the second term can be derived from equation (2.22) and (2.23). From (2.22), we have

$$\frac{\partial\phi}{\partial x} \approx -\frac{4\pi}{\lambda} B \cos(\theta - \alpha)\left(\frac{\partial\theta}{\partial x}\right)_0 \tag{2.28}$$

and from (2.23), we have

$$\frac{\partial\theta}{\partial x} = \frac{x_0}{rH\sin\theta_0} \tag{2.29}$$

Substituting (2.28) and (2.29) into (2.27), we have an equation to estimate the height h from the reference ellipsoid

$$h = x - x_0 \approx \frac{-\lambda rH\sin\theta_0}{4\pi x_0 B\cos(\theta_0 - \alpha)}(\phi - \phi_0) \tag{2.30}$$

If there is no deformation between two passes, the phase for the curved earth effect,

denoted ϕ_{flat}, is given by:

$$\phi_{flat} = \phi - \phi_0 = -\frac{4\pi}{\lambda}\frac{B\cos(\theta_0 - \alpha)}{r\sin\theta_0}\frac{x_0}{H}h \tag{2.31}$$

On the other hand, if there is any deformation, d, the phase consists of topographic and deformation phase. For this case, the phase can be expressed as:

$$\phi_{flat} = -\frac{4\pi}{\lambda}\frac{B\cos(\theta_0 - \alpha)}{r\sin\theta_0}\frac{x_0}{H}h + \frac{4\pi}{\lambda}d \tag{2.32}$$

2.5. Differential SAR Interferometry and Interferometric stacking technique

The basic idea of the differential SAR interferometry is to separate the effects of surface topography and coherent deformation, allowing to retrieve differential deformation maps. In the so-called two-pass differential interferometry approach, the topography-related phase term is calculated from a DEM. Alternatively, in the so-called three-pass and four-pass approaches, the topographic-related phase term is estimated from an independent interferometric pair with a short acquisition time interval. In many cases, the use of a DEM turns out to be more robust and operationally practicable.

Phase distortion caused by spatially heterogeneous atmospheric condition limit the accuracy of differential SAR interferometry. Large atmospheric distortions can often be identified by their specific shape, by cross-comparison of interferograms, or possibly based on meteorogical data. It is not clear, though, how to best integrate such test in an operational processing chain.

Stacking is a method that reduces the atmospheric effects on SAR interferometry by averaging independent SAR interferograms. Assuming that atmospheric effects are uncorrelated between the interferograms and the displacement velocity is constant in time, averaging N independent interferograms will reduce the atmospheric signal to $1/\sqrt{N}$ fold. Because the displacement increases with increasing acquisition time interval, interferometric pairs with long acquisition time intervals are preferred to reduce the effect of the atmospheric distortions. In order to map faster displacement velocity, shorter intervals are preferred to study the temporal dynamic of the displacement.

Chapter 3

Subsidence Monitoring of Bandung Basin using Differential SAR Interferometry

Abstract — *This chapter describes the land subsidence monitoring of the Bandung Basin based on Synthetic Aperture Radar (SAR) data of ALOS/PALSAR. Since the subsidence has occurred in most of urban regions, differential SAR interferometry (DInSAR) technique is suitable to estimate the subsidence for long time duration between two observations. We generated 32 interferograms from 21 ascending SAR images over a period from January 1, 2007 to March 3, 2011. In order to remove topographic phase, we used the 3-arc-second Shuttle Radar Topography Mission (SRTM) digital elevation model (DEM). This chapter also demonstrates capability of DInSAR to estimate and describe land subsidence history with time series of interferograms. However, an individual differential interferogram may be deteriorated by atmospheric phase. Assuming the displacements are stationary, we estimated the subsidence rate by averaging the interferograms which is the so-called interferogram stacking technique. The technique eliminates atmospheric phase and other uncorrelated noise phases. The maximum subsidence is about 12 cm per year which occurred in Cimahi city. The use of groundwater for the industrial and residential activities has significant effects to the land subsidence. Moreover, the subsidence expansion depends on the geological structure over Bandung basin. Besides using the stacking differential InSAR, we also applied the interferometric point target analysis. We have successfully described the seasonal characteristics of the land subsidence.*

We conclude that using the InSAR technique we have successfully estimated and characterized the land subsidence in Bandung basin. Therefore, this technique has great potential to monitor the phenomena of the subsidence in Bandung basin.

3.1 Introduction

Vulnerability and exposure of people and assets to natural hazards in the Indonesian big cities have caused a growing impact of natural hazards in these cities. Some factors increasing their vulnerability are (1) a growing concentration of people and economic activities in conurbations; (2) an increase in the land use changes with an inadequate land-use zoning and planning and (3) a fast industrial development, environmental

degradation and urban expansion. These factors are inter linked each other.

The Bandung basin is located in the West Java Province, Indonesia. The basin has an elevation ranges between 660 and 2,750 m above sea level (Figure 3.1). Bandung basin, which has a total area 2,340.88 km^2 consisting of 77 sub-districts, covers four administrative areas, including two regencies (a part of Bandung and Sumedang) and two cities (Bandung and Cimahi). The population of Bandung Metropolitan was 6,080,981 in 2003 and it is predicted to increase to 9,706,363 in 2025 (Wangsaatmaja, et al., 2006). The growth in population and industry caused an increasing in groundwater demand. Therefore, the biggest consumers of groundwater in this area are the domestic and industrial sectors. Nearly 50% of industries in Bandung Basin are textile industries. Converting land use from agriculture to some purposes, such as for housing, industrial, road construction, and waste disposal site, has worsened environmental impacts (Suhari and Siebenhuer, 1993).

Excessive groundwater extraction in Bandung Basin has induced land subsidence. The subsidence is a type of regional geological hazard, which slowly develops to serious impacts on society, economy, and the natural environment. The subsidence may cause serious problems, such as (1) changes in elevation and slope of streams, canals, and drains; (2) damage to roads, railroads, bridges, and canals; (3) damage to private and public buildings; and (4) failure of well casings; (5) changes in the groundwater flow system. According these impacts, it is very important to monitor the land subsidence in Bandung Basin.

Global Positioning System (GPS) observation is a traditional geodetic technique for land surface leveling with an accuracy in order of millimeter. Studies of subsidence due to groundwater extraction using GPS observations were carried out in Bandung, Indonesia (Bitelli et al., 2000, Abidin, et al., 2008) and in Tianjin, China (Lixin et al., 2011). Abidin et al., 2008 also investigated the characteristics of Bandung subsidence estimated from GPS surveys and InSAR. However, they focused on GPS measurements in detail and did not explore in detail the capability of InSAR to estimate the rate of the subsidence. They estimate the Bandung subsidence from InSAR during the period between June 2006 and March 2007. Furthermore, although the GPS surveys can provide subsidence information with high accuracy, it is costly, time consuming and sparse spatial resolution for a large and inaccessible area. Of course, both GPS surveys

and InSAR technique have advantages and disadvantages. Therefore, in order to obtain an accurate and cost-effective technique for the land subsidence monitoring it should be considered InSAR technique as main tool, otherwise GPS surveys is as a validity data. This study however demonstrates InSAR, which is a modern geodetic technique, for subsidence monitoring method as a stand-alone tool over period from 2007 to 2011.

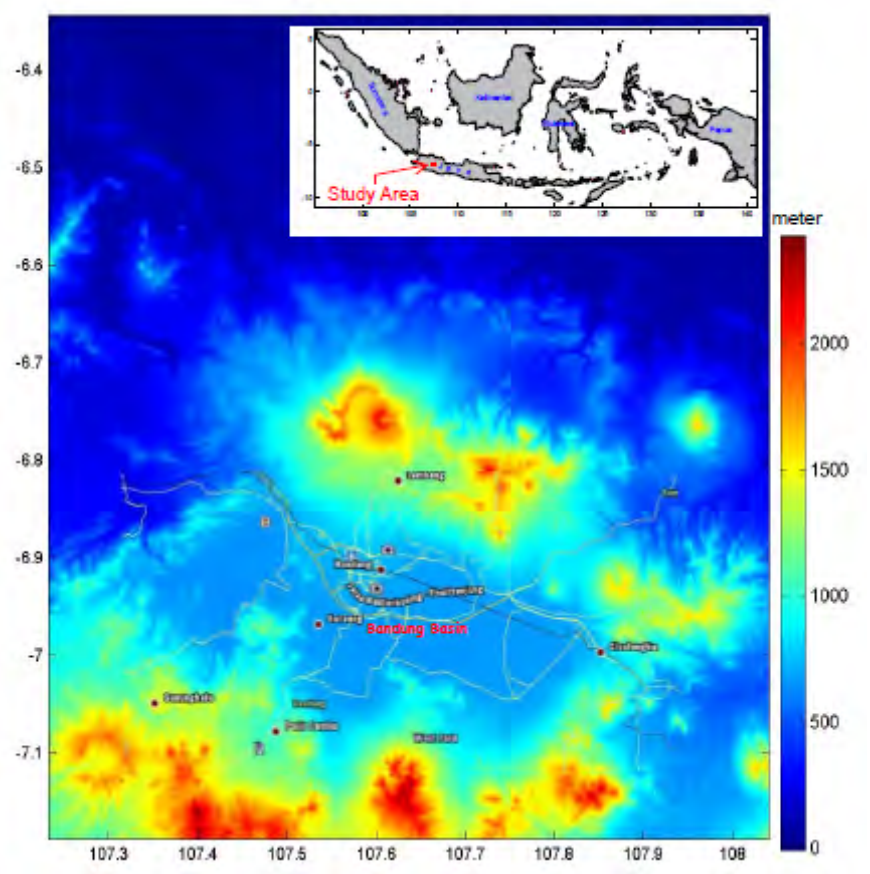

Figure 3.1. Topography of study area, Bandung Basin.

Synthetic Aperture Radar (SAR) is a microwave-coherent imaging system that has day, night and all weather capabilities. In repeat-pas SAR interferometry (InSAR) datasets of the same area acquired from almost identical perspective are co-registered and combined into a so-called interferogram. Differential InSAR which is a development of the basic InSAR allows the detection of very small (cm, mm level) movement of land surface feature. Therefore, the differential InSAR is suitable to monitor the land subsidence in the Bandung Basin

The objectives of this study are (1) to demonstrate the use of differential

interferometry for observing land subsidence within the Bandung Basin region; (2) to measure subsidence rates by stacking interferograms.

3.2 Study area

The Bandung basin is part of a chain of depressions in West Java, which is the so-called Bandung zone. This zone can be regarded as a graben-like longitudinal belt of intramontane depressions, extending through the center of West Java. The Bandung basin is located in the central part of this zone and encircled by mountains. Initially a large volcano was located to the north of the present Bandung Basin, which is called the Sunda volcano. Geologically, the development of the Sunda Volcano into Mount Tangkuban Parahu had been an important factor in the history of the Bandung Basin. Bemmelen (1949) recognized three eruption phases of Mount Tangkuban Parahu after first collapse, separated by two other phases of collapse and faulting along the Lembang Fault.

In the Bandung Basin, the aquifer mostly comprises deposits of channels and lenses. Some shallow aquifers can be found in the floodplain deposits. Deeper aquifers are located in the foot slope of the hilly are which encircle the Bandung Basin. In the center of the basin, the deeper aquifer should be very scarce with very low transmissivity.

Delinoma and Suriadarma (2010) identified the groundwater flow system in the Bandung Basin using subsurface temperature, hydraulic head, and D and 18O stable isotope composition. Three types of flow system exist within the Bandung Basin i.e., shallow, intermediate and deep groundwater flow system (Figure 3.2). The two shallow systems mostly recharged in the lower part of the mountainous slope in the North, East and Southeast of the basin, and discharged in the shallow area within the basin. The intermediate system mostly recharged in the upper part of the Northern Mountainous Slope and flowed from the Western part of the basin (Cimahi area), passing through Bandung City and discharged in the Southern part of Rancaekek. The deep system recharged from the top of the Malabar Mountainous Complex in the South, passing through Banjaran and Margahayu and discharged in the area around the Citarum River Valley in the vicinity of Dayeuhkolot and Soreang. Some of the groundwater then joined the intermediate groundwater flow and together discharged in the Rancaekek

area. No indication was found of higher elevation water recharged in the Northern part of the basin which means the water recharged in the Mount Tangkuban Parahu area did not reach the Bandung Plain.

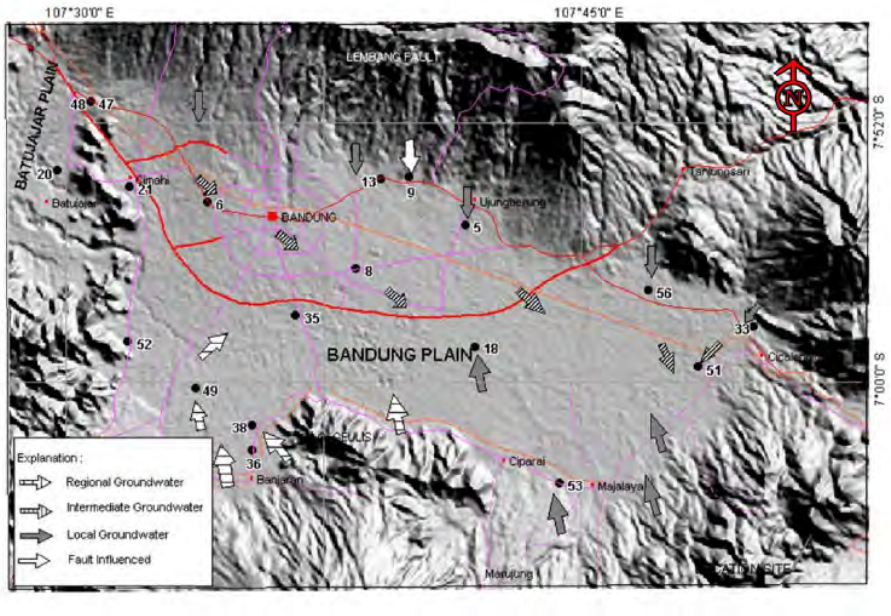

Figure 3.2. Horizontal Groundwater flow Direction of Bandung Basin.

3.3 Methodology

3.3.1 Data

In this study we use image data level 1.0 for the period from 2007 to 2011 (Table 3.1). The data are the high-bandwidth (FBS, 28 MHz) and low-bandwidth (FBD, 14 MHz) modes from ascending orbits with an off-nadir 34.3 deg. Main advantages of the L-band (23.6-cm wavelength) over C-band (5.6-cm wavelength) are deeper penetration of vegetated areas results in less temporal decorrelation enabling interferogram to have longer time separation and longer baseline increases the critical baseline resulting more usable interferometric pairs. Stacking differential SAR interferometry is applied in this study to derive subsidence maps. In short, two SAR images acquired from two slightly different positions, at different times, are used to estimate the phase difference, or so-called interferogram, between the two acquisitions.

Table 3.1. List of PALSAR data used in this study

No	SLC Images (yyyy/mm/dd)	Mode	fdop (Hz)
1	2007/01/14	FBSH	34.235
2	2007/03/01	FBSH	59.554
3	2007/07/17	FBDH	80.497
4	2007/09/01	FBDH	77.100
5	2007/12/02	FBSH	40.822
6	2008/01/17	FBSH	61.818
7	2008/03/03	FBSH	65.032
8	2008/04/18	FBSH	71.928
9	2008/06/03	FBDH	83.145
10	2008/07/19	FBDH	99.337
11	2008/09/03	FBDH	79.694
12	2008/12/04	FBSH	29.759
13	2009/07/22	FBDH	85.695
14	2009/10/22	FBDH	47.774
15	2010/01/22	FBSH	53.718
16	2010/03/09	FBSH	65.401
17	2010/04/24	FBSH	65.238
18	2010/07/25	FBDH	66.632
19	2010/09/09	FBDH	66.570
20	2010/12/10	FBDH	46.977
21	2011/03/12	FBSH	51.846

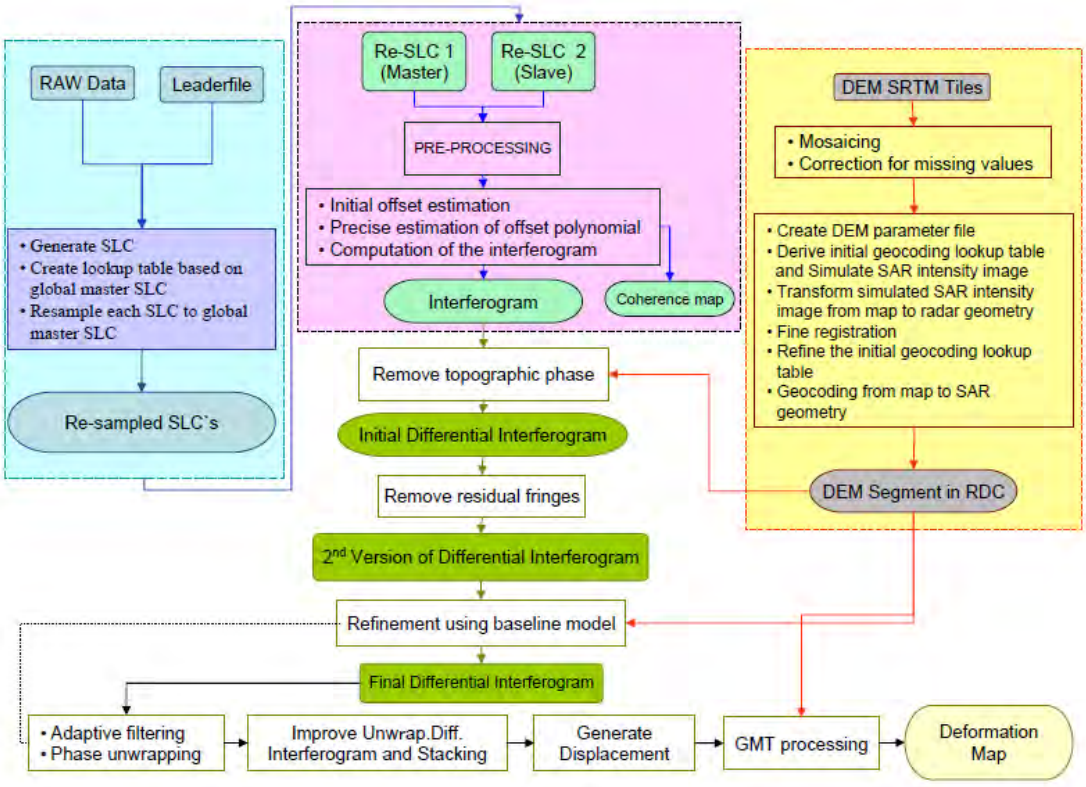

Figure 3.3. Differential InSAR processing flow for estimation of Bandung Basin subsidence.

Some phases in the interferogram are related to topographic information, land deformation occurred between the acquisitions, atmospheric disturbances, orbit errors and decorrelation noises. The topographic phase is simulated by using a 3-arc-second SRTM digital elevation model (DEM), which is removed from the interferogram. In the differential interferogram a complete 2π phase change is equivalent to a height displacement of half the wavelength of the radar signal in the slant range direction. For ALOS L-band data that is 11.75 cm. In order to eliminate atmospheric disturbances we calculate average of the unwrapped differential interferograms with different temporal baselines. Therefore, the subsidence estimate is in cm/year. Generally, our InSAR processing flow can be described as in Figure 3.4.

3.3.2 Interferogram generation

Before generating interferogram, we generated twenty-one Single Look Complex (SLC) images from PALSAR raw data. In order to eliminate the potential of slightly different azimuth imaging geometry and maintain coherency, all images were processed using a common Doppler centroid frequency of 63.465 Hz. Using the same Doppler centroid SAR processing can maximize the fringes visibility (Werner et al., 200). A global master SLC (No. 2 in Table 3.1) was selected with 9640 pixels wide and 24705 pixels long. All other SLC images were then co-registered to the global master SLC in order to make all SLC images having the same geometry. In the interferogram generation, co-registration between master and slave SLC in each interferogram pair was in sub-pixel accuracy.

To remove parts of the image spectrum which do not contribute to the interferogram, we applied common-band filtering in both range and azimuth direction. Therefore, these filtering can improve the coherence of the interferogram. Once interferogram has been generated, coherence that is the complex correlation between the master and co-registered slave image was calculated over 5x5 pixel window in the pair interferogram. In addition, this coherence is a measure of interferogram quality.

For interferogram generation, we have constructed from images not only in FBS-FBS pairs but also in FBS-FBD combination pairs. Table 3.2 shows the temporal baseline (Btemp) and perpendicular baseline (Bperp) between two acquisitions for each pair. Interferometric processing of two images needs to estimate relative offsets and a slave image must be resampled to a master one. Initial range and azimuth offsets

between two SLC images are estimated based on orbital information for a first guess of the offsets. It is then improved based on cross-correlation function of the image intensities. In order to avoid ambiguity problems and still to achieve an accurate estimate first we run with multi-looking 4 in range and 4 in azimuth, followed by a second run a single look. The SNR threshold of intensity correlation used is at least 7.0 for accepting/rejecting the offset estimates and the subset for cross-correlation is put in the middle of the image with a dimension of 1024x1024 pixels.

Table 3.2. Temporal and spatial baseline for interferograms

No.	**PAIR** (yy/mm/dd_yy/mm/dd)	**Btemp** (days)	**Bperp** (meters)
1	070301_070717	138	-35
2	070301_070901	184	59
3	070301_071202	276	-445
4	070301_080303	368	-368
5	070301_080603	460	-667
6	070301_080903	552	173
7	070301_081204	644	371
8	070301_090722	874	-26
9	070301_091022	996	54
10	070301_100122	1058	-216
11	070301_100725	1272	-235
12	070301_100909	1318	-561
13	070301_101210	1410	-808
14	070301_110312	1472	-604
15	070717_080719	368	-6
16	070901_080303	184	-427
17	071202_081204	368	816
18	080117_081204	322	711
19	080303_080719	138	326
20	080418_090722	460	336
21	080603_090722	414	640
22	080719_090722	368	15
23	080903_091022	414	-120
24	081204_100122	414	-588
25	090722_100725	368	-208
26	100122_101210	322	-592
27	100309_110312	368	-456
28	100424_110312	322	-169
29	100725_110312	230	-370
30	090722_100309	230	-122
31	100309_100909	184	-413
32	100909_110312	184	-43

For precise (sub-pixel accuracy) estimation of range and azimuth offset polynomials we used a method based on the image intensity The more important parameters are number and size of the offset estimation windows in range and azimuth, and the offset estimation threshold. The co-registration accuracy required is typically 1/5 the of pixel or 1/8 th of a resolution (Balmer and Just, 1993).

The bilinear registration offset polynomial was determined based on the field of registration offsets and SNR threshold. The quality of registration between images can be looked at the estimate standard deviation of the offset in range and azimuth. Once the co-registration polynomial has been obtained and the slave SLC has been re-sampled to the reference geometry using 2-D SINC interpolation, generation of the interferogram can be performed. Range spectrum filtering is applied to account for the spectral shift induced by the difference in incidence angles between SLC-slave and SLC-master due to baseline. The azimuth common band filtering prior to interferogram generation is also applied to retain only the common segment of the azimuth image spectrum for the correlation optimization.

3.3.3 Creating look-up table for geocoding

In the creation of the look-up table for geocoding we have to prepare Digital Elevation Models (DEM). In this study DEMs are freely obtained from SRTM (Shuttle Radar Topography Mission) at 3 arc-second resolution. In order to cover all target area from InSAR scene four DEM tiles are mosaiced. The DEM size is 2401 x 2401 pixels and -8.333333e-04 decimal degrees for the longitude and latitude posting in EQA projection. The creation of geocoding look-up table can be seen the processing flow in Figure 3.3. A critical step of this processing is the refinement of look-up table. The refinement look-up table needs a sub-pixel accuracy of offset estimes between a simulated SAR intensity image derived from DEM and a real SAR intensity image. Standard deviation below 0.3 is required to run geocoding reasonably well.

3.3.4 Differential Interferogram

In differential interferometry processing we used a 2-pass approach which is based on an image interferometric pair and a DEM in SAR coordinate. The DEM transformed

from the EQA projection to radar map was used to generate a simulated unwrapped interferometric phase corresponding to topographic (including the curved earth trend) called topographic phase. This process requires the baseline information obtained from orbit data. The differential interferogram was generated by subtracting the simulated unwrapped phase from the interferogram. The differential interferogram is called an initial differential interferogram which still exhibits a few fringes across the image because of small error in baseline model.

3.3.5 Improvement of Differential Interferogram

There are two steps to improve the differential interferogram i.e., (1) based on fringe rate and (2) based on Ground Control Points (GCP's) and baseline model.

Based on fringe rates

To improve the differential interferogram we improved the baseline estimate by estimating the residual baseline not accounted in the initial baseline estimate from the orbits using the fringe rate and then added the residual baseline to the initial baseline to obtain an improved version of baseline. Once obtaining the improved version of baseline we re-simulated the topographic phase which was used to generate the improved version of the interferogram (the 2^{nd} version of differential interferogram). The systematic fringe pattern will apparently slightly disappear and differential phase is clearly more visible.

Baseline estimation based on GCPs and a baseline model.

We refined the differential interferogram by estimating the baseline based on ground control points (GCPs) and baseline model. This estimation requires an unwrapping interferogram and DEM in radar geometry. Unwrapping interferogram was generated by adding the unwrapped differential phase to the unwrapped simulated phase. This unwrapped interferogram is the unwrapped version of the original interferogram. The resulting interferogram represents the original interferogram however with the baseline as estimate so far from orbits and fringe rate. In other words, if this baseline is not the true baseline the interferogram will contain residual systematic fringes that will be estimated with the baseline model. The following steps used to unwrap differential phase are (1) an adaptive filtering, (2) estimation of the degree of coherence, (3) generation of phase unwrapping validity mask, (4) adaptive sampling reduction for

phase unwrapping validity mask, (5) unwrapping phase with minimum cost flow (mcf) technique, (6) interpolation of gaps in unwrapped phase data, (7) phase unwrapping using model of unwrapped phase.

This filtering is to reduce the phase noise thereby reducing the number of residues which is problematic location for phase unwrapping. There are some methods of the interferogram filtering. In this study we used a modified Goldstein filter (Z.W.Li.,et.al., 2006). The modification can prevent an area with high coherence from being over-filtered, while at the same time allow strong filtering in applications.

We computed the coherence image from the differential interferogram using a 5x5 window. From the coherence image the phase unwrapping mask was obtained with variation of thresholds depending on the quality of interferogram. This threshold is rather high in order to be sure to unwrap only areas with reliable phase information. Phase unwrapping of differential interferogram was done using a minimum cost flow (*mcf*) method. To start unwrapping the phase we chose a point of high coherence in the middle of an area with valid points to be unwrapped. Each differential interferogram has different point to start unwrapping depend on coherence of the image.

Because an effect of validity mask in unwrapping process is gaps, we filled them by interpolation. Once the differential interferogram is unwrapped using mcf method, we need to apply the phase unwrapping using model of unwrapped phase. Since we can assume that the interpolated phases are close to the correct unwrapped phase, at least within an interval $(-\pi,\pi)$, they can be used as phase model in the sense that the unwrapped phases are re-calculated from the complex valued interferogram assuming that the phases values in the model correspond to the correct unwrapped phase within the interval $(-\pi,\pi)$. After completion of the unwrapping a phase constant is subtracted from all unwrapped phase value such that the unwrapped phase at the indicated reference location corresponds to the indicated reference phase value.

Once generating unwrapping interferogram we selected the number of GCP points in range and azimuth using the coherence mask to indicate whether a candidate point has sufficiently high coherence, i.e. sufficiently reliable phase information. The refined baseline estimation was done using least squares fit for a number of control points of the known height. This new precise baseline was used to generate a simulated phase image of the curved earth and topographic components which we then subtracted

from the original interferogram to obtain a new version of the interferogram (final differential interferogram).

3.3.6 Height-dependent atmospheric phase removal

Depending on atmospheric conditions there is an altitude dependence of the path delay with respect to altitude caused by changes in the atmospheric water vapor and preassure profiles between the acquisitions of the interferometric image pair. The parameters of a linear model of the residual phase with respect to the altitude values in the input height data are estimated. The model consists of a phase constant a_0 in radians and phase slope a_1 in unitis of radians per meter. The phase model has the height dependent unwrapped phase as determined from the linear regression. Since the model is estimated based on the regression, it is removed from the unwrapped differential interferogram.

3.3.7 Compensation of Unwrapped Differential Interferogram for Residual Quadratic Phase

In case for large baseline changes along-track due to the squinted orbit some residual phase components still appear across the image. It needs to correction of such quadratic phase components. The first step is estimation of a coherence image from the differential interferogram from which we generated a mask with a threshold value of coherence. The mask was then applied to determine the model phase function. Finally, the model fit was applied to the differential interferogram to obtain the refined version of the interferogram.

3.3.8 Stacking differential interferograms and Generation of Surface Displacement Map

Once the unwrapped differential interferograms were improved, a single unwrapped differential interferogram can be constructed by the stacking technique. Since all interferograms were resampled to the global interferogram, they have a same geometry that the stacking is easily implemented to generate a displacement rate. The differential Interferometric phase corresponds to the displacement along the SAR look vector. As a consequence the 3-dimensional displacement of a surface element cannot be completely

described. Under the assumption of a predefined surface displacement direction a conversion to vertical or horizontal displacement is possible. To map vertical displacement in meters with positive signs corresponding to increasing surface height and negative signs to subsidence.

3.4 Results

3.4.1 Co-registration of images

In this study we have required three co-registration analyses during DInSAR processing i.e., re-sampling SLC images to global master SLC image, generating interferograms and creating a geocoding look-up table. These processes are actually required before resampling one image to a reference one. The quality of the co-registration is relied on offset measurement between the images. The co-registrations have accuracy variation depend on the quality of the images which are applied the process. In this study we tried to obtain in sub-pixel accuracy. Based on Balmer and Just (1993), the co-registration accuracy required is typically 1/5 the of pixel or 1/8 th of a resolution. Some parameters used to obtain optimal accuracy are search window size in range and azimuth, SNR threshold, number of tie points, and standard deviation. We have tried to apply lower search window in order to have efficient processing time. The lower search window is not only faster processing required but also higher accuracy. However, some images are quite hard to estimate the offsets. We have therefore applied higher search window in order to obtain the suitable offsets with good accuracy.

In our script of InSAR processing, we have generated graphs that can be used to determine some parameters such as the number of tie points between master and slave images, SNR threshold and standard deviations in range and azimuth. For example, in co-registration between SLC images for the date of March 1, 2007 and March 3, 2008, we have used the search window size of 128 pixels both in range and azimuth and number of samples of 32 samples both in range and azimuth in co-registration for interferogram generation. From these input parameters, we have generated two graphs that describe relationships between the standard deviation and SNR threshold and between the number of fit offsets and SNR threshold, Figures 3.5 (a) and (b) respectively. The SNR of the offset measurement is obtained by taking the ratio

of the peak value divided by the average correlation level outside the 3x3 peak region.

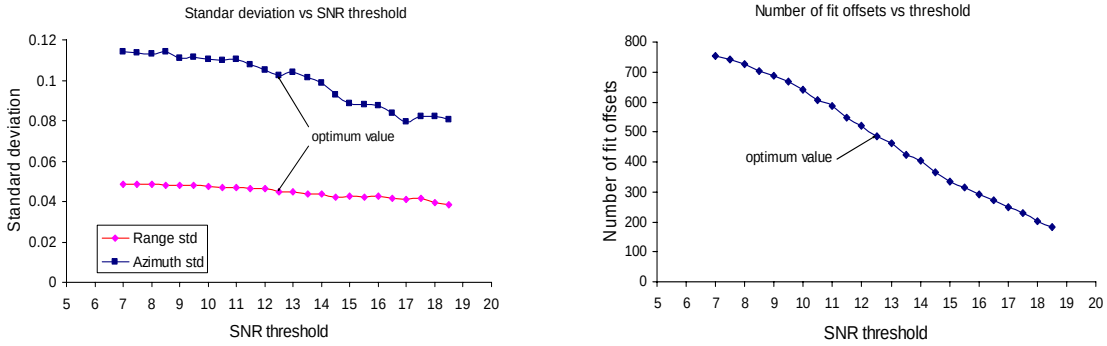

(a) (b)

Figure 3.4. Standard deviation and number of offset estimates as a function of SNR threshold in co-registration of SLC images for interferogram generation of 070301_080303

Figure 3.4a shows that the standard deviation less than 1/8 pixels in both range and azimuth for SNR threshold 7. Higher SNR threshold we can obtain better standard deviation. However, the number of fit offsets decrease as higher SNR threshold. If the number of fit offset is not enough to estimate a polynomial offset function, the co-registration will be not good. Therefore, we define the optimal SNR threshold so that the standard deviation and number offsets are suitable for the co-registration. From the graphs we chose the SNR threshold 12.5 so that the standard deviations are 0.0449 and 0.1026 pixels in range and azimuth, respectively. Otherwise, a number of fit offsets (tie points) are 486 samples.

A summary of the offset estimation in the interferogram generation is shown in the Table 3.3. and the resulting intereferogram of 2007/03/01 – 2008/03/03 in Figure 3.5. Fringes in urban region are very clear with high frequency due to long baseline. Contrary, the interferogram in agricultural area is dark due to strong decorrelation.

In addition, the accuracy of co-registration between the simulated intensity image derived from DEM and the SAR intensity image for look-up table refinement can be achieved in sub-pixel as well. Figure 3.6 shows graphs of the resulting standard deviation and number of tie points with variation of SNR correlation coefficients. These graphs were interactively used and generated in the geocoding look-up creation in order to obtain high accuracy. From these graphs, we defined the SNR threshold 21.5 and the obtained standard deviations are 0.0635 pixels in range and 0.0368 pixels with 780 offset estimates. The values of the resulting standard deviations indicate that geocoding

run very well.

Table 3.3. Description of co-registration accuracy for interferogram generation

No.	PAIR yy/mm/dd_yy/mm/dd	Search Window		Number of Tie Points	Standard Deviation (pxl)		SNR Threshold
		Range	Azimuth		Range	Azimuth	
1	070301_070717	128	128	550	0.0799	0.0887	11
2	070301_070901	128	128	420	0.0833	0.1021	12
3	070301_071202	128	128	595	0.0397	0.0904	11
4	070301_080303	128	128	486	0.0449	0.1026	12.5
5	070301_080603	256	256	715	0.0657	0.0906	12
6	070301_081204	512	512	709	0.0466	0.1926	18
7	070301_080903	256	256	645	0.0343	0.0877	15
8	070301_090722	256	256	696	0.0687	0.1023	12
9	070301_091022	256	256	703	0.0747	0.1092	11.5
10	070301_100122	256	256	692	0.0357	0.1114	13
11	070301_100725	256	256	620	0.0719	0.1105	13.5
12	070301_100909	512	512	752	0.0534	0.0827	14
13	070301_101210	512	512	758	0.0504	0.0813	14
14	070301_110312	256	256	707	0.0419	0.0942	12
15	070717_080719	256	256	682	0.0601	0.0715	12.5
16	070901_080303	256	256	629	0.0632	0.0853	13.5
17	071202_081204	256	256	732	0.0302	0.0811	13.5
18	080117_081204	256	256	679	0.0346	0.0906	15
19	080303_080719	256	256	640	0.0604	0.0748	14
20	080418_090722	256	256	575	0.0574	0.0744	15.5
21	080603_090722	256	256	692	0.0554	0.0822	12.5
22	080719_090722	256	256	611	0.0486	0.0711	15
23	080903_091022	512	512	787	0.0424	0.1956	14
24	081204_100122	256	256	683	0.0254	0.1067	15
25	090722_100725	256	256	654	0.0491	0.0744	14
26	100122_101210	256	256	692	0.0587	0.1109	13
27	100309_110312	128	128	508	0.0450	0.0997	12
28	100424_110312	256	256	785	0.0272	0.0652	11
29	100725_110312	256	256	680	0.0512	0.0639	14
30	090722_100309	256	256	715	0.0671	0.0805	12
31	100309_100909	256	256	662	0.0520	0.0652	13
32	100909_110312	256	256	675	0.0505	0.0746	14

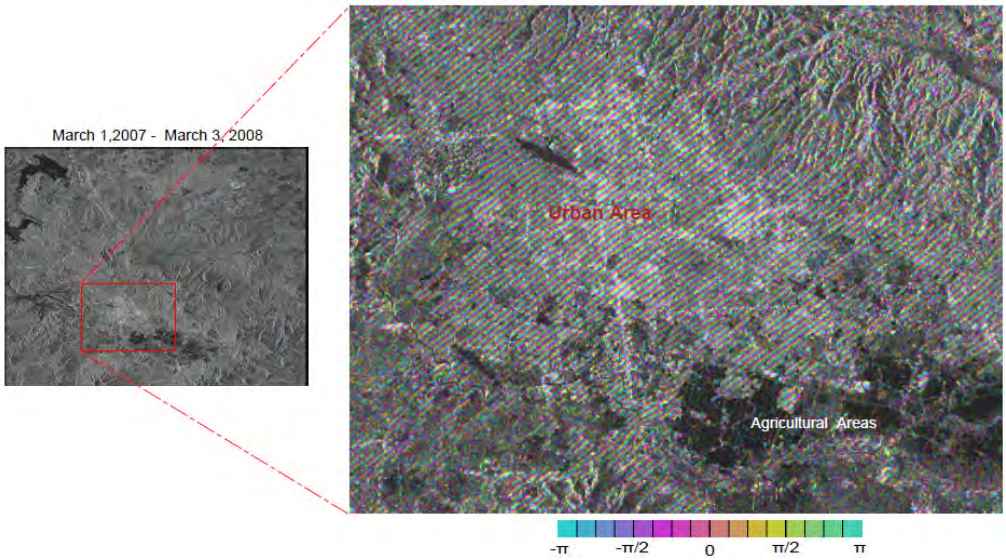

Figure 3.5. Interferogram showing urban area has clearer fringes than mountainous area and also farmland area.

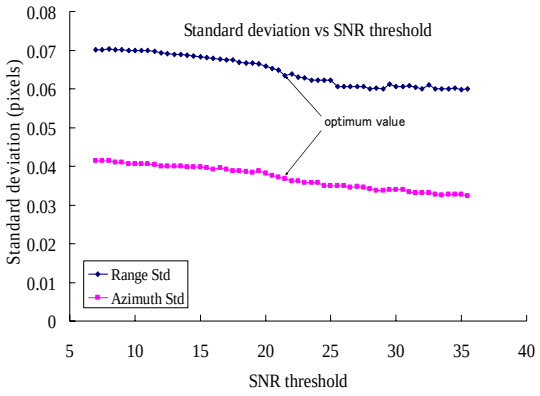

(a)

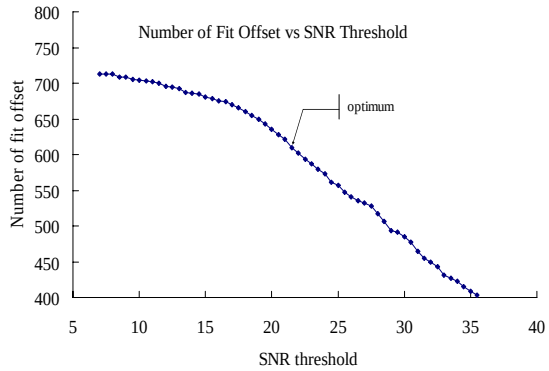

(b)

Figure 3.6. Standard deviation and number of offset estimates as a function of SNR threshold in co-registration between the simulated SAR intensity image derived from DEM and the real SAR intensity image for creating the geocoding look-up table.

3.4.2 Interferogram coherence

Quality of the resulting interferograms can be assessed by measuring the correlation between the pixels. It is commonly called as coherence which is a direct measure for the similarity of the dielectric properties of the same scatterers represented by pixels between two SAR acquisitions. Figure 3.7 shows a coherence comparison of the resulting interferograms with the master image of 2007/03/01 for the variation of the temporal and perpendicular baselines. Mean coherence is calculated over all area in the interferogram including farmland, lake, rivers, vegetative and hilly regions. Although mean coherence values of each image are quite low, we can see that urban region, where subsidence occurred, has a quite high coherence. It means that although two SAR observations to generate an interferogram are in a long time interval, the estimation of the subsidence using the differential InSAR technique is reasonably performed.

Low correlation regions correspond mainly to steep reliefs. Furthermore, the farmland and flooding areas can also be easily identified with a lower coherence. Satisfactory correlation coefficients are obtained over flat urban areas. The feasibility of radar interferometry for monitoring the ground surface displacement depends on the subsidence rates, i.e., displacement gradient, in combination with the influence of decorrelation due to land use or vegetation and of atmospheric signal in the interferograms. Although the temporal decorrelation poses a significant limitation for obtaining continuous displacement maps, it is observed that urban areas remain coherent for extended time intervals as shown in Figure 3.7.

A critical factor which determines the feasibility of SAR images to generate an interferogram to reveal surface deformation is a perpendicular baseline. The increase of the perpendicular baseline leads to lower coherence which results in a decorrelation of phase value. Although the coherence in Figure 3.7h has a larger temporal decorrelation (874 days) than that of Figure 3.7g (664 days), it has a higher coherence due to shorter baseline (-26 m). Figure 3.8 shows a relationship between mean coherence and the variation of perpendicular baselines with the same time interval (368 days) of two SAR observations. As baseline increases, the mean coherence decreases. Therefore, the existence of baseline decorrelation limits the number of image pairs suitable for interferometric application.

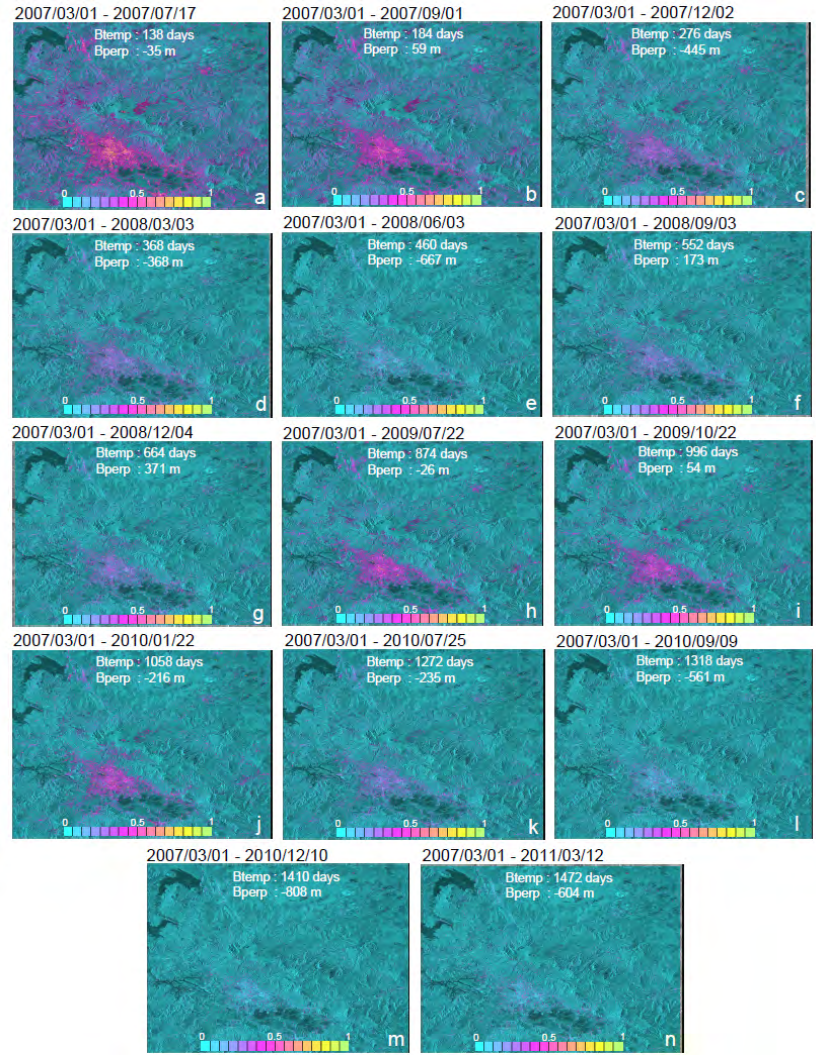

Figure 3.7. Coherence comparison with the master image of 2007/03/01 for the variation of temporal and perpendicular baseline.

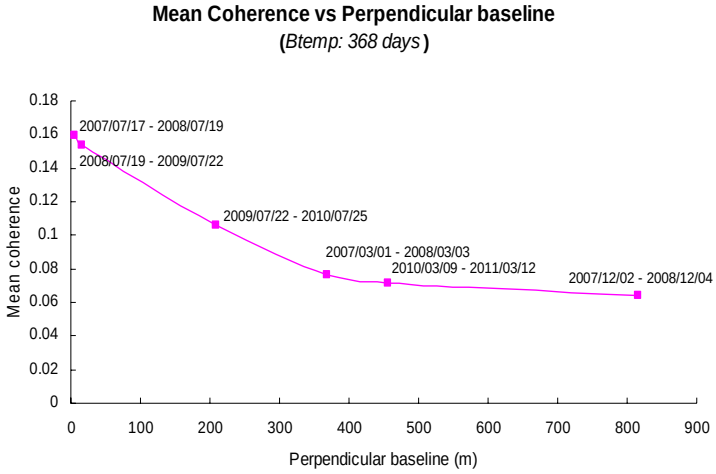

Figure 3.8. Relation between mean coherence and the variation of perpendicular baselines with the same time interval of two SAR observations.

3.4.3 Improving the differential interferogram

Figure 3.9 shows a differential interferogram comparison between before and after improvements. From the initial baseline estimate and the DEM in SAR geometry, we have generated a simulated phase image consisting of curved Earth and topographic fringes. The initial differential interferogram (Figure 3.9a) has been obtained by removing the simulated phase from the interferogram. The differential interferogram shows clearly residual fringes across the image. The systematic residual fringes are due to the inaccuracies in the baseline estimate from orbits as well as on the baseline model used.

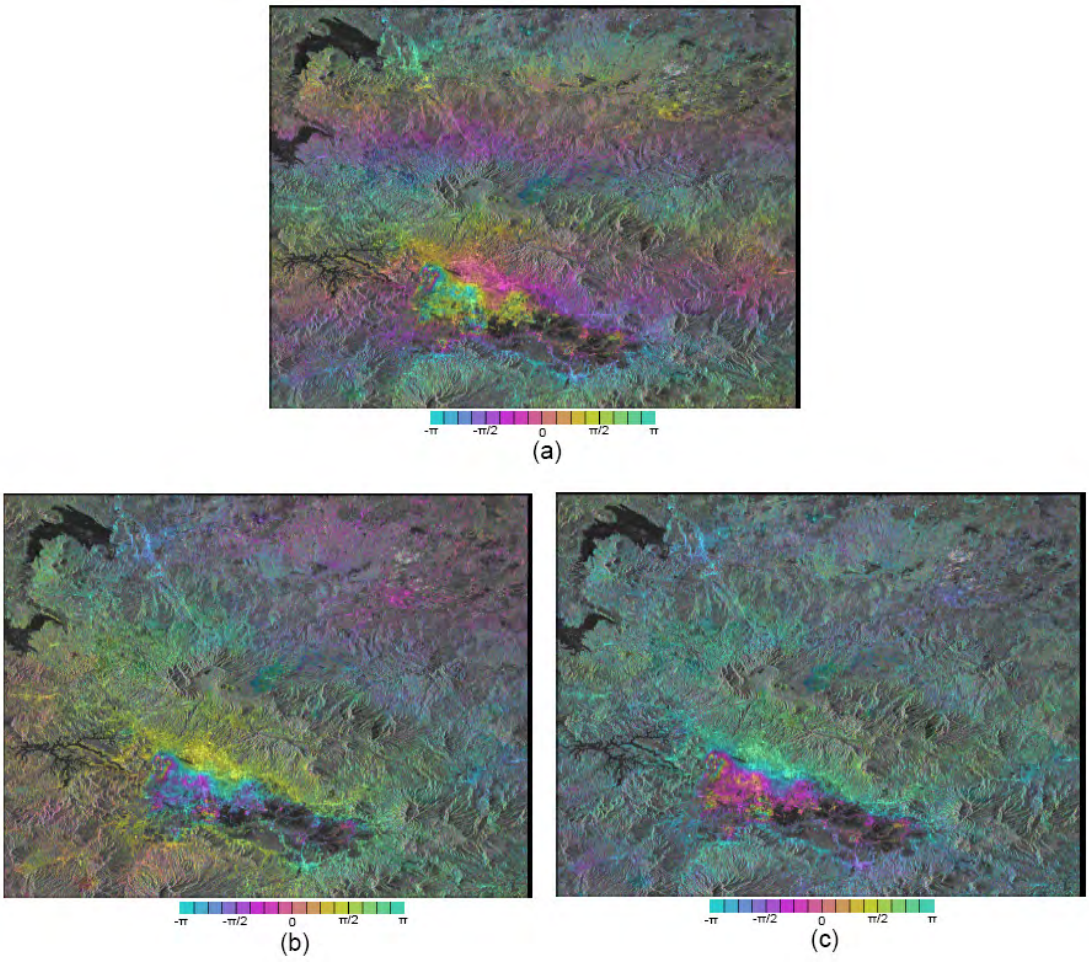

Figure 3.9. Differential SAR interferograms with a temporal baseline of 368 days, between March 1, 2007 and March 3, 2008. (a) Original one obtained after removing from the original interferogram the curved Earth and topographic phase components based on the initial interferogram, (b) Improved differential interferogram after improving baseline using fringe rate and (c) Improved differential interferogram after improving baseline using precise baseline estimation based on least square method.

We have improved the differential interferogram by improving the baseline estimate. Using fringe rate, we have estimated the residual baseline not accounted in the initial baseline estimate from orbits. By adding the residual baseline to the initial baseline, we have obtained an improve version of the baseline. The difference between the baseline estimates is 0.897 m. We have then re-simulated the curved Earth and topographic phase using the improved baseline version. Finally, we have obtained the improved version of the differential interferogram (Figure 3.9b) by subtraction the new simulated phase from the initial interferogram. The improved interferogram seems to present fewer fringes than the initial differential interferogram.

After improving differential interferogram using fringe rate, some phase trends still exist related to an imperfect estimate baseline as shown in Figure 3.9c. We have used GCPs and baseline model to refine the differential interferogram. In order to estimate baseline based on GCPs, we needed an uwrapped interferogram and a DEM in SAR geometry. We have generated the coherence image from which a mask was obtained by using the threshold of 0.7 in order to avoid that the baseline is determined based on GCPs with unreliable phase value. This value was also applied to mask the low coherence while unwrapping the differential interferogram. Beside the threshold, we have also masked the area indicating the subsidence occurred. Figure 3.9c shows that the improved differential interferogram seems to present slightly less spatial variations to the previous version in Figure 3.9b. The validity of the baseline model is certified by the RMS altitude error, 15 m. The error corresponds to the mean difference between the true elevation and the elevation estimated through the baseline model at the GCPs. The difference between the baseline estimate and intial version is 0.6 m.

Figure 3.10 shows filtered interferogram of the images in Figure 3.9b and 3.9c. The filtered interferogram in Figure 3.10b is much better than that of in Figure 3.10a. Residual phases in Figure 3.10b after the baseline improvement using GCP from DEM and baseline model are much less than the version in Figure 3.10a. However, phase trend which is not related to deformation still presents over the interferogram. In order to eliminate this deformation-uncorrelated phase, we improved the unwrapped version of the differential interferogram in Figure 3.10b. Figure 3.12 shows a comparison of the unwrapped differential interferogram between original and improved versions. The interferogram which is uncorrected the baseline using GCP and baseline model clearly

shows the presence of the deformation-uncorrelated phase trend over the image.

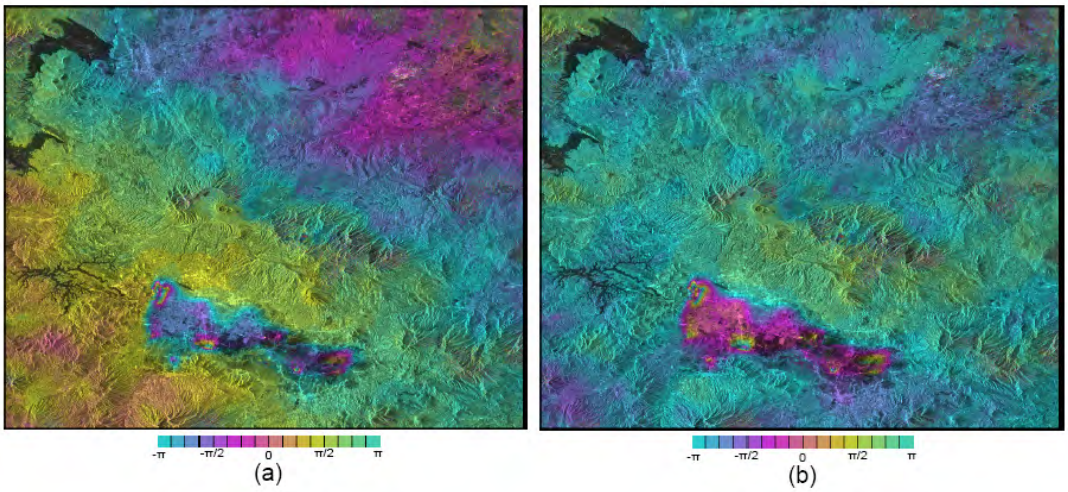

Figure 3.10. Filtered differential SAR interferograms (a) filtered version of the image in Figure 3.9b and (b) filtered version of the image in Figure 3.9c.

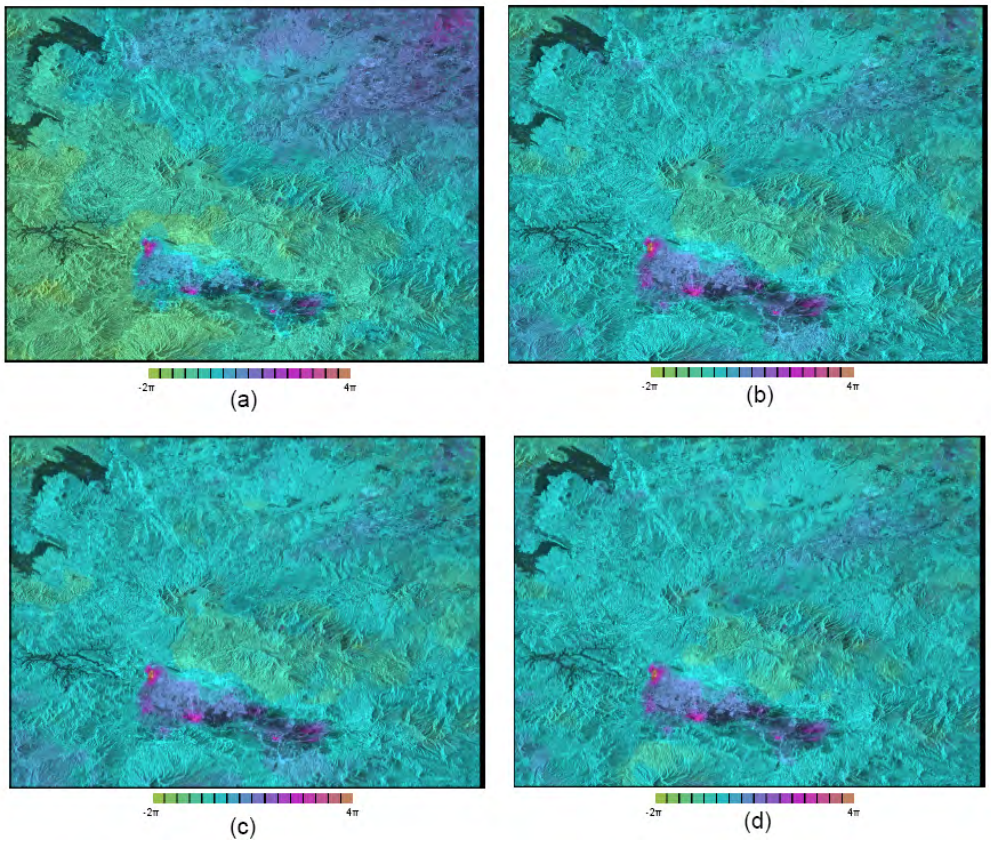

Figure 3.11. Unwrapped differential SAR interferograms. (a) corresponding to image in Figure 3.9b, (b) corresponding to image in Figure 3.9c, (c) after atmospheric as height function removal and (d) after quadratic phase trend removal.

3.4.4 Land subsidence history

Once the unwrapped differential SAR interferograms are improved, they are converted into vertical displacements. Negative values of displacements are indicated as land subsidence.

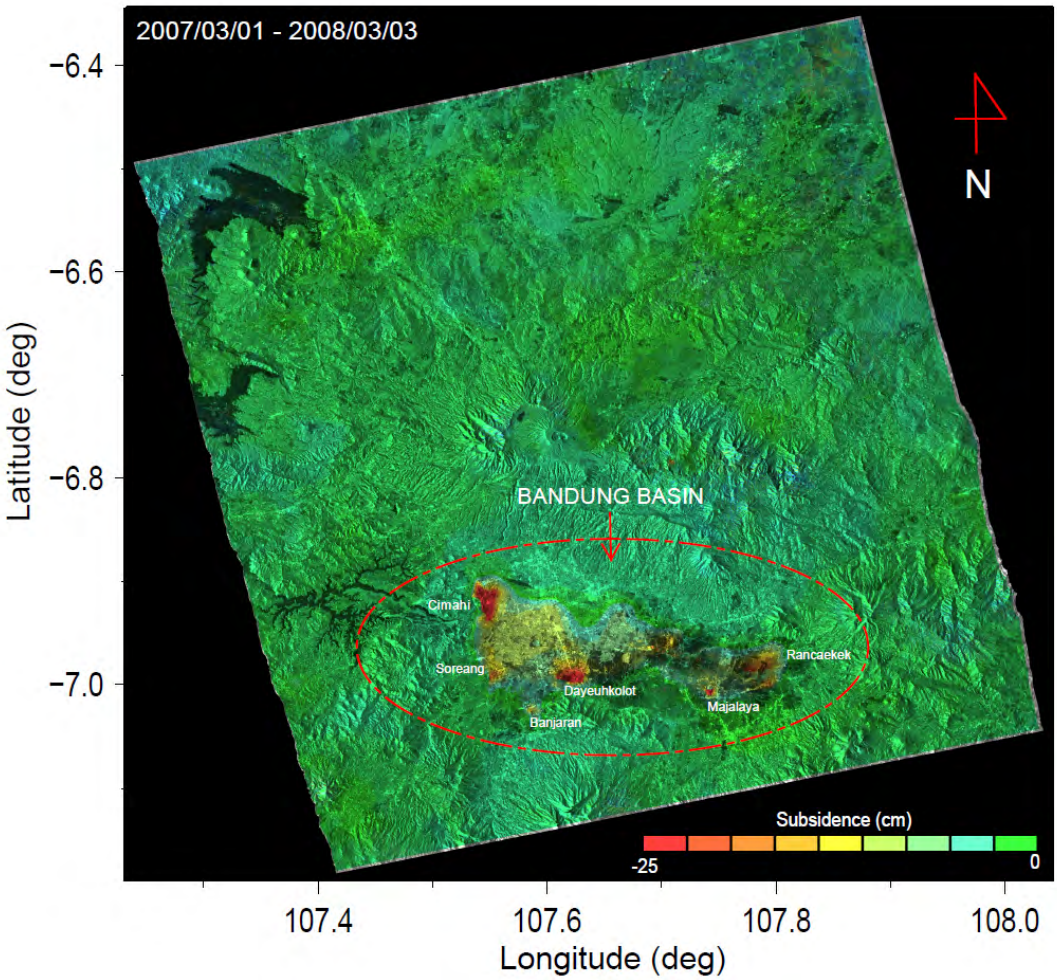

Figure 3.12. The DInSAR derived estimate of the ground subsidence at the Bandung Basin, over the 368 days from March 1, 2007 to March 3, 2008.

Figure 3.12 shows DInSAR-derived land subsidence spanning from March 1, 2007 to March 3, 2008. Subsidence patterns are very clearly indicated in urban regions in Bandung Basin, which most of industries are established and consuming in a large amount of groundwater. Cimahi city experienced the largest land subsindence with a magnitude of about 12 cm. In other cities, such as Dayeuhkolot, Rancaengkek, Majalaya, Banjaran and Soreang, land subsidence also occurred up to about 10 cm. The subsidence history is getting larger for the longer time intervals as shown in Figure 3.13.

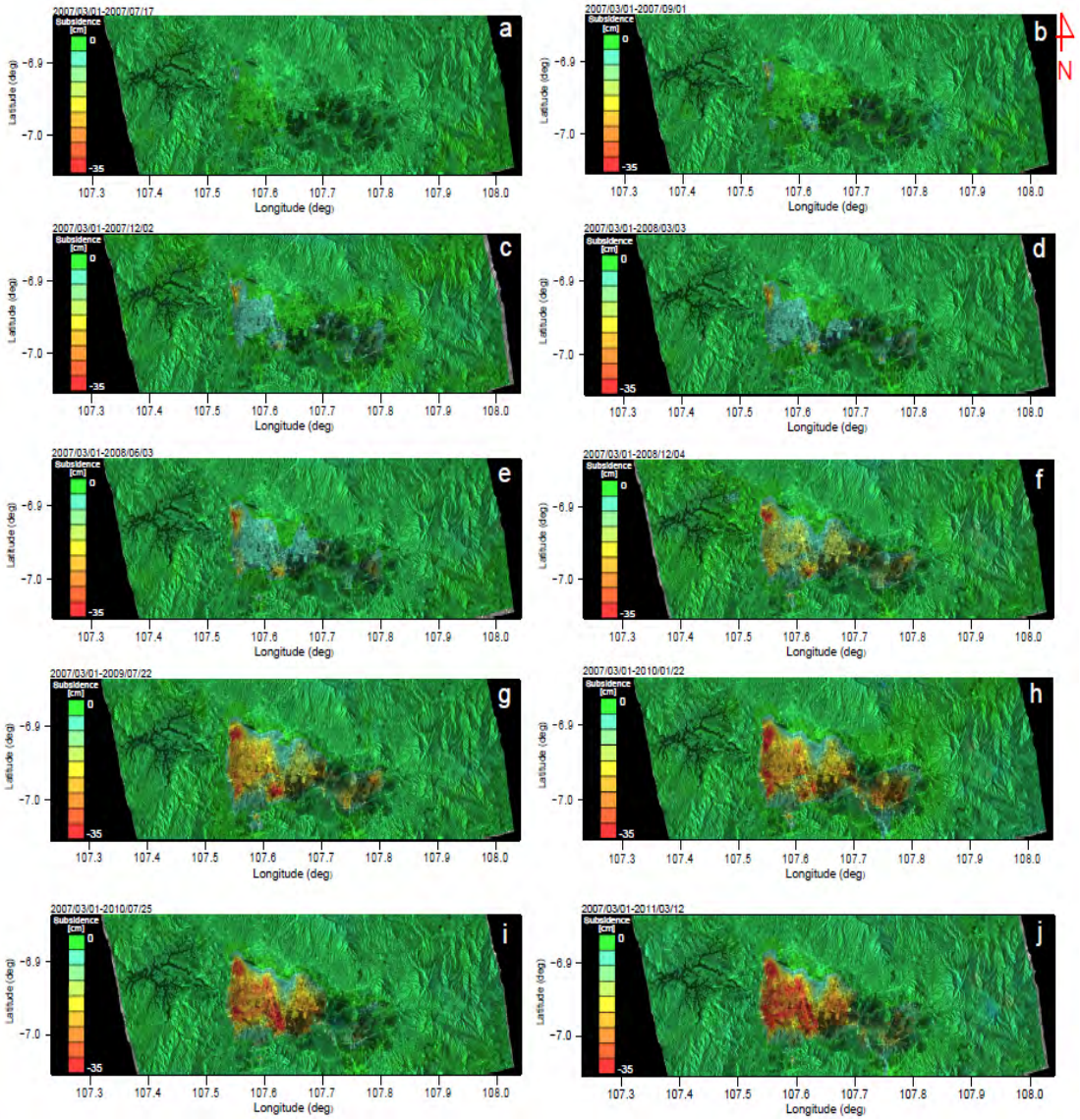

Figure 3.13. Historical subsidence patterns in Bandung Basin with increasing temporal baselines between 138 days and 1472 days over the period from March 1, 2007 to March 3, 2011. In order to make comparable the level of the subsidence, the color scale of each map is made in the same scale from 0 to -35 cm.

3.4.5 Stacking differential SAR interferograms

Atmospheric signals may deteriorate single interferograms, making an interpretation of a single interferogram cumbersome. By cross-comparison of the interferograms, we can identify atmospheric signals by their specific shape and magnitude. Figure 3.14 shows that two series of interferograms can easily identify that influence of atmospheric artifacts is present. Although phase trends due to inaccuracy baseline are removed from interferogram, the phase trend which is uncorrelated to deformation phase still presents

in these intereferogram. Fortunately, the trends are in opposite sign (plus and minus) so that they can be removed by averaging the interferograms, so-called stacking technique.

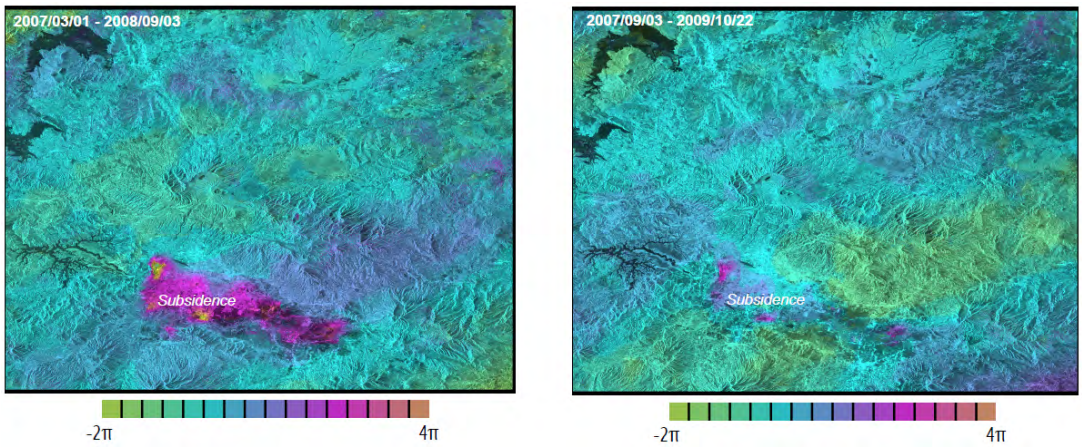

Figure 3.14. Identify atmospheric effects from two differential SAR interferograms which have overlapping observation times.

From Figure 3.14, it can be identified that the levels of the atmospheric phases seem to be same in the consecutive interferograms with the overlapping times but the deformation phases are smaller in the interferograms with smaller time interval than those of larger interval. The phase noise level and pattern of images in the left and right sides of Figure 3.14 are similar although their time intervals are different. In contrast, the displacement level in left side of Figure 3.14 with the time span of 552 days is much larger than that of right side of Figure 3.14 with the time span of 414 days. Therefore, in order to increase displacement signal and suppress the atmospheric and random phases, the stacking technique is prefer to use the interferogams with longer time interval between two acquisitions for area which has less effect of the temporal decorrelation, such as urban area. In this study, the longest time interval is 1472 days (about three years) from March 1, 2007 to March 12, 2011. However, in order to estimate faster displacement rates, shorter intervals are preferred to suppress atmospheric phase.

The stacking technique is intended not only to suppress the atmospheric phase but also random phase noises, especially phase component due to temporal decorrelation. The result of the stacking is presented by centimeter per year shown in Figure 3.15 with the largest subsidence about 12 cm/year in Cimahi city. The rate is a good agreement with that of GPS measurement (Abidin et al., 2008). From this subsidence map, we suspect that the largest amount of groundwater extraction is in Cimahi city.

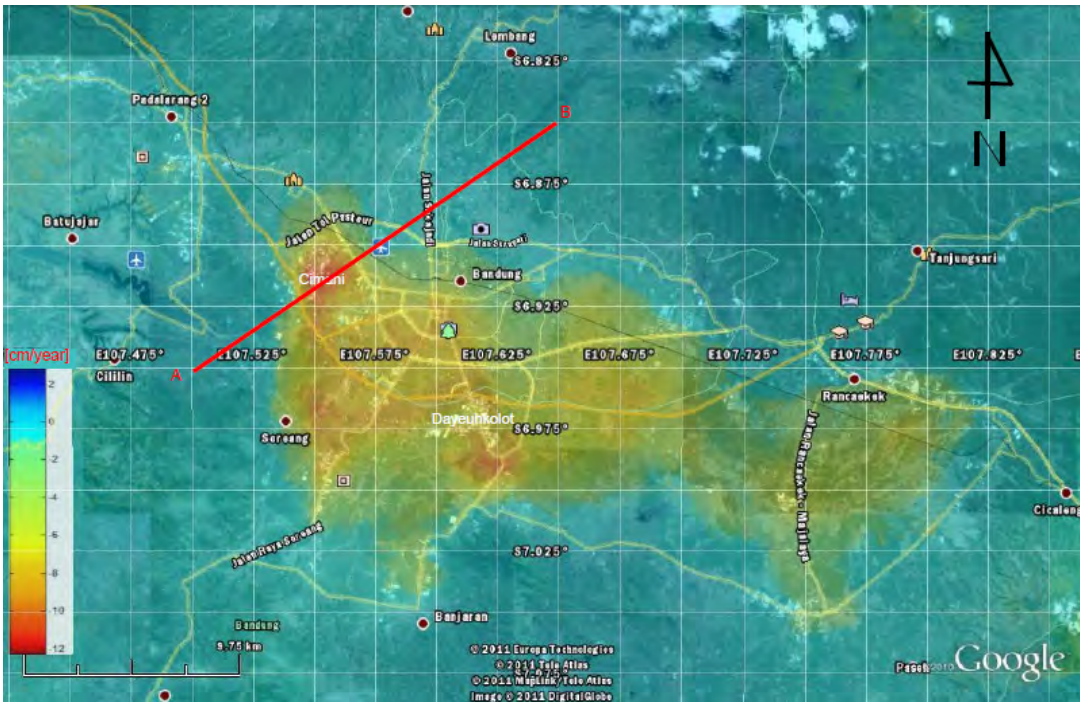

Figure 3.15. Subsidence rate in Bandung Basin obtained from stacking 32 differential SAR interferograms. Note that rectangular discontinuity on the right part of the image is due to the background image of the Google Earth.

3.5 Interpretation

3.5.1 Relationship between subsidence, production well distribution, and aquifer damage zones

The InSAR-estimated subsidence rate in Figure 3.15 is also correlated with the production well distribution (Figure 3.16) for most of Bandung basin. Region with the dense distribution of wells around Cimahi and Bandung have experienced the large land subsidence.

Excessive groundwater extraction can lead to largely decline in its level and in turn decrease pore fluid pressure. The decrease in the pore fluid pressure causes an equivalent increase in effective stress within the aquifer system, which causes the aquifer system skeleton to compress. This compression propagates through underlying layers up to ground surface as a subsidence. Figure 3.17 show the aquifer zoning map for Bandung Basin evaluated in year 2010. The zonation is classified into four levels based on a percentage of the groundwater level decline. The aquifer is classified as damage, critical, prone and safe zones when the percentage of groundwater decline are more than 80%, 60-80%, 40-60% and less than 40%, respectively. The damage zones

are closely related to large land subsidence zones estimated from differential SAR interferometry data, Figures 3.13 and 3.15.

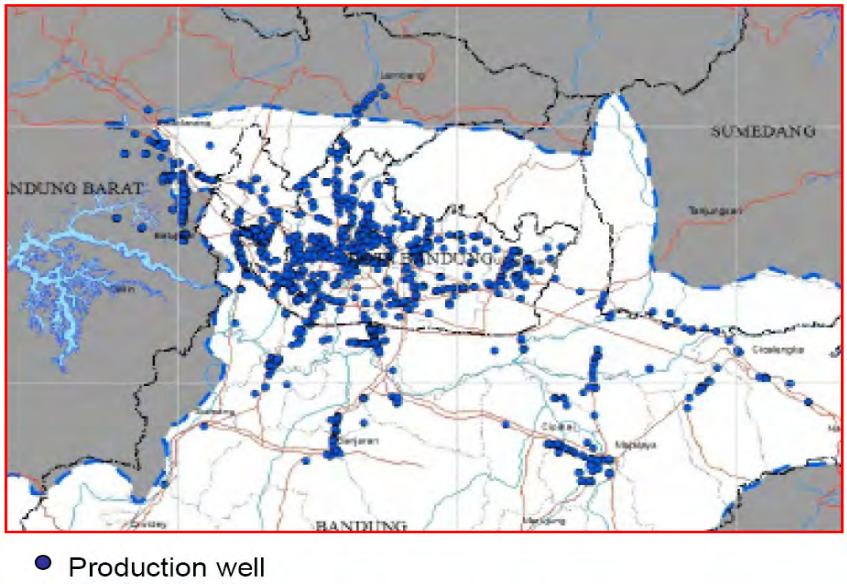

Figure 3.16. A map of well production distribution in Bandung Basin. Most of production wells are concentrate Cimahi and Bandung cities (Anonymous, 2011).

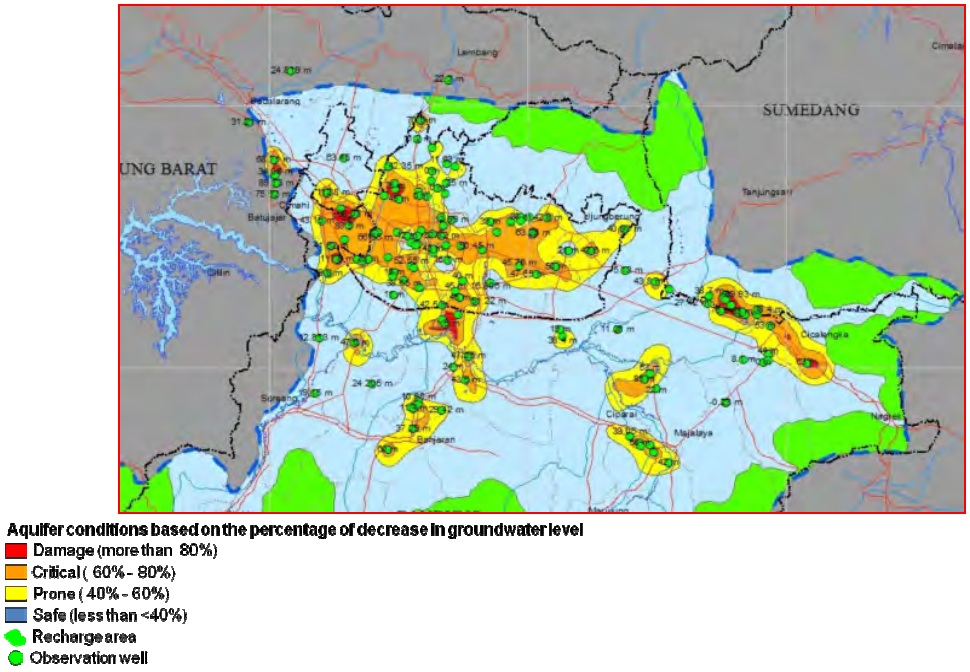

Figure 3.17. A map of aquifer zoning of Bandung Basin update in 2010 (Anonymous, 2011)

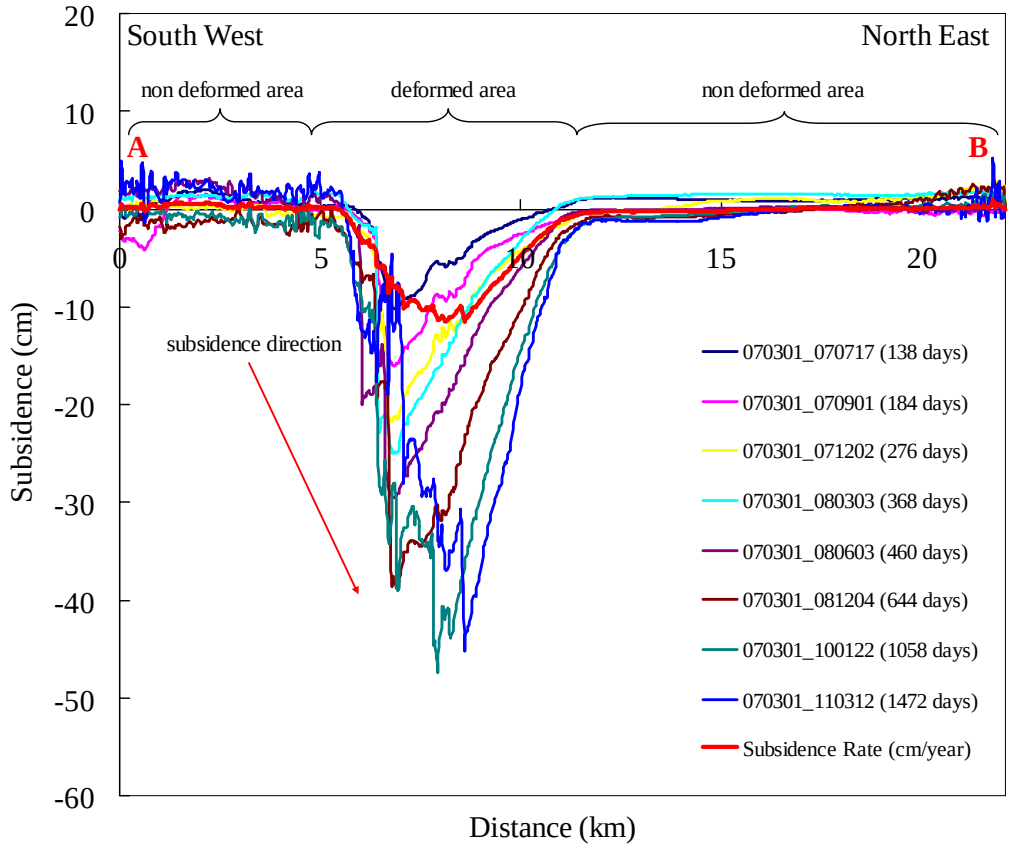

Figure 3.18. Profiles of subsidence across Cimahi city along line A B in Figure 3.15 obtained from stacking 32 differential SAR interferograms and an individual SAR interferogram with the time intervals from 138 to 1472 days with the baseline date of March 1, 2007.

Figure 3.18 shows profiles of subsidence to illustrate the magnitude and directional development of subsidence patterns and the subsidence rate across Cimahi city which has experienced the large land subsidence. From these profiles, we can show that the subsidence patterns from eight profiles obtained from differential interferograms with the time intervals from 138 to 1472 days are highly consistent each other and the subsidence propagates in the Southwest to Northeast direction. It is a very interesting phenomenon showing characteristics related to geological conditions in the aquifer and its surroundings. If the layers are homogenous horizontally the subsidence patterns should be symmetry in that direction in the historical profiles. Moreover, in the Northeast part of Cimahi city, Bandung city, the subsidence should be expected to occur due to much amount of water extracted in that area as indicated in the aquifer zoning map which is categorized as a damage area. However, the subsidence map is not always in a good agreement with the aquifer zoning map for certain area.

To investigate these phenomena, we overlaid subsidence rate with the

geological map of Bandung Basin as shown in Figure 3.19. From this geological map, it can be identified that the deformed area in Cimahi city is located between two consolidated rocks with different geological structure. A large amount of groundwater extraction in the Northeast Cimahi city does not lead to land subsidence in the compacted layer. The characteristic of the subsidence in Bandung Basin is clearly controlled by geological structure. This is also a reason that in several areas subsidence is not correlated to the distribution of production well distribution and the decrease of groundwater level.

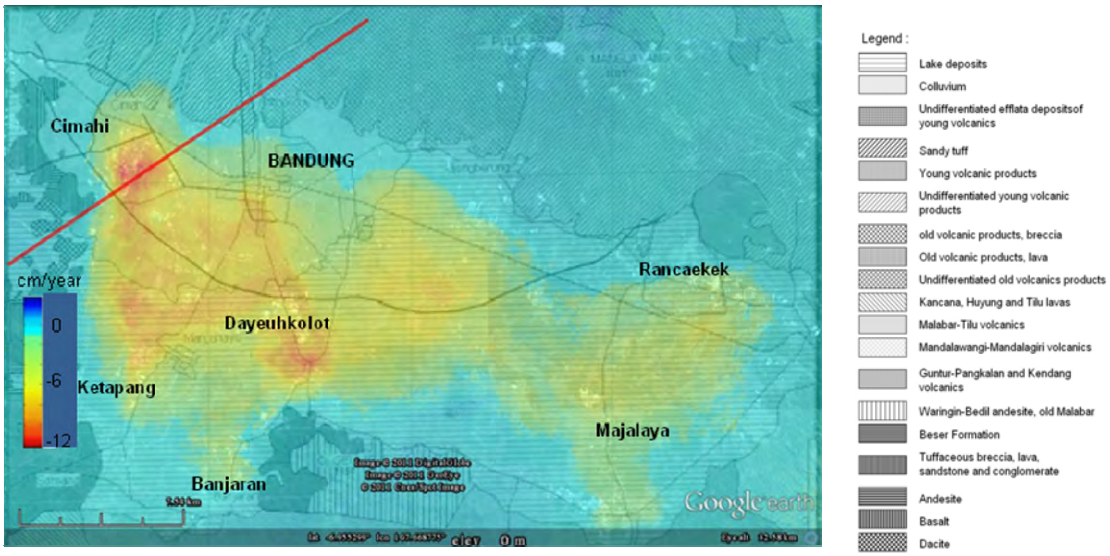

Figure 3.19 Subsidence rate overlaid with Geological map of Bandung Basin and the geological map developed by Delinom and Suriadarma, 2010.

3.5.2 Seasonal changes of land subsidence in Bandung Basin

Through the interferometric point target analysis (IPTA), we have not only suppresd atmospheric artifacts but also divided the displacement into linear and nonlinear components. Figure 3.20 shows the linear, nonlinear and total displacement at point 2009927 in Cimahi city. The magnitudes of subsidence rate estimated from the linear displacement component estimated using IPTA are well match with those estimated using DInSAR as previously discussed.

Furthermore, we analyzed the characteristic of land subsidence in Bandung Basin based on the nonlinear component of displacement. The temporal characteristic of the nonlinear displacement is seasonally periodic as shown in Figure 3.20b. It is in good

accordance with the weather in Indonesia which has two seasons (wet and dry season). During dry season starting around October 2007, the nonlinear component of displacement decreases. Whereas starting around June 2008, there is a significant increase in the magnitude of the nonlinear displacement component. This phenomenon occurred due to significant recharge process of groundwater from surface water to aquifer. The groundwater recharge may be from its surrounding area for shallow aquifer and from far area, such as mountainous areas, for deeper aquifer.

As consequences the seasonal process of groundwater recharge during wet season slowed up the observed subsidence. Whereas during dry, the subsidence was accelerated due to increase in imbalance between groundwater extraction and recharge rate. The similar characteristic of the subsidence is also indicated in several regions over Bandung Basin such as in Dayeuhkolot (Figure 3.21) and in Ketapang (Figure 3.22).

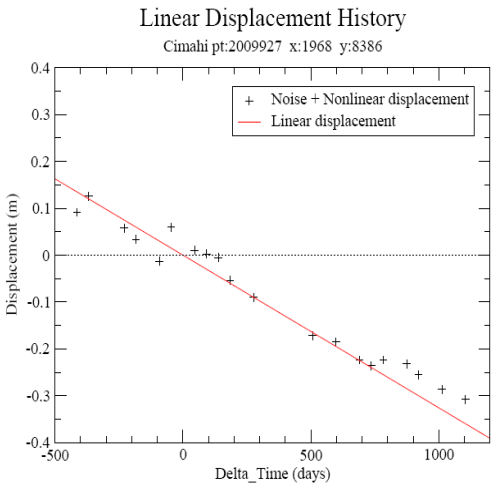

(a)

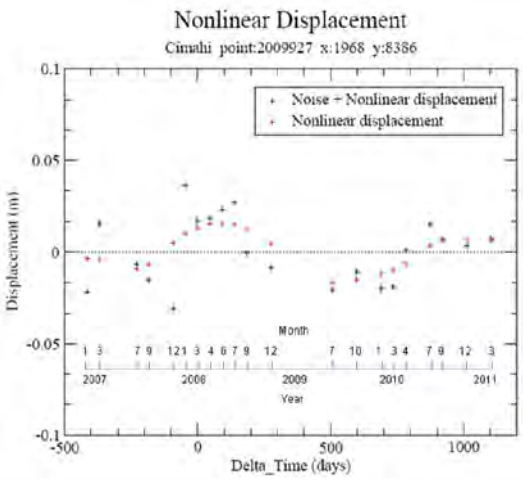

(b)

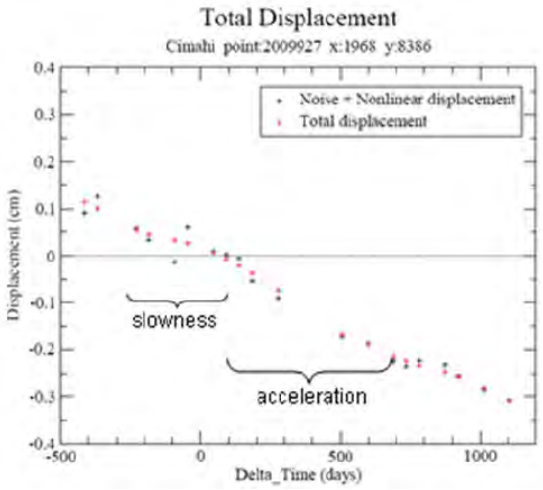

(c)

Figure 3.20 (a) Subsidence rate from linear displacement is 11.9 cm/year, (b) nonlinear displacement, and (c) total subsidence history from January 14, 2007 until March 12, 2011. Reference orbit date is March 3, 2008.

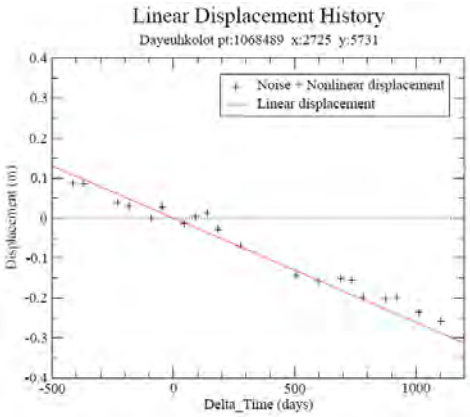

(a)

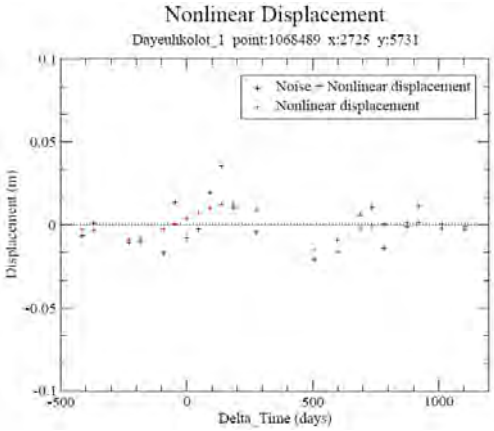

(b)

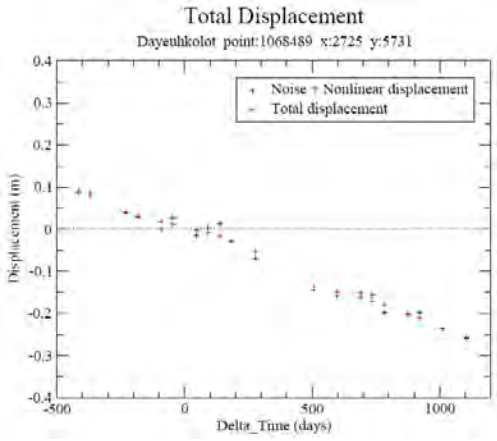

(c)

Figure 3.21 (a) Subsidence rate from linear displacement is 9.54 cm/year, (b) nonlinear displacement, and (c) total subsidence history from January 14, 2007 until March 12, 2011. Reference orbit date is March 3, 2008.

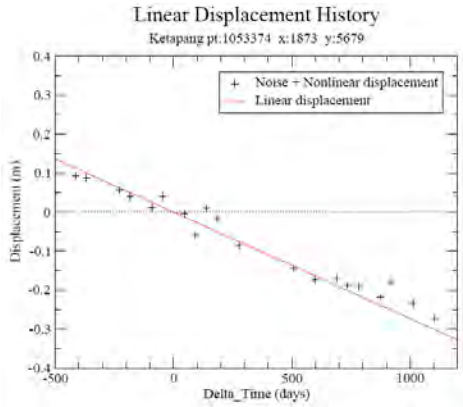

(a)

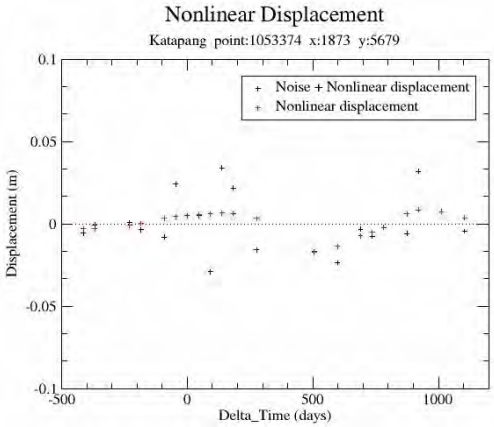

(b)

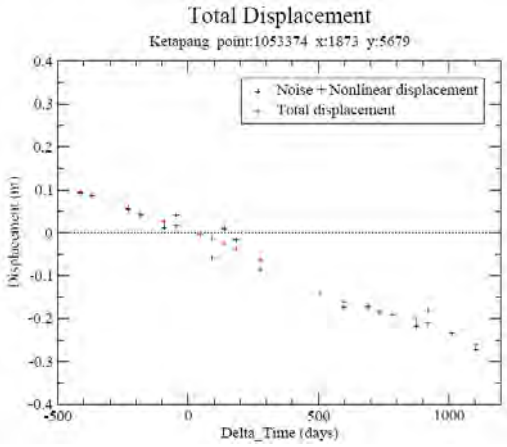

(c)

Figure 3.22 (a) Subsidence rate from linear displacement is 9.98 cm/year, (b) nonlinear displacement, and (c) total subsidence history from January 14, 2007 until March 12, 2011. Reference orbit date is March 3, 2008.

3.6 Conclusion

This chapter has demonstrated the capability of differential SAR interferometry for monitoring the development and rate of land subsidence in Bandung Basin, West Java, Indonesia over the period from March 1, 2007 to March 3, 2011. Most industrial regions that experienced larger subsidence are correlated to groundwater extraction areas. The largest rate of land subsidence derived from the stacking technique is about 12 cm/year in Cimahi city. Based on the analysis the subsidence has been governed by geological structures and seasonal changes.

References

Anonymous, 2011. Naskah akademik raperda kota Bandung tentang pengelolaan air tanah, *Laporan Akhir*, BPLH kota Bandung.

Abidin, H. Z., Andreas, H., Gamal, M., Wirakusumah, A. D., Darmawan, D., Deguchi, T. & Maruyama, Y. (2008) Land subsidence characteristics of the Bandung Basin, Indonesia, as estimated from GPS and InSAR. *Journal of Applied Geodesy*, **2**(3), 167–177. DOI : 10.1515/JAG.2008.019.

Balmer, R., Just, D., 1993. Phase statistics and decorrelation in SAR interferograms. Proceedings of the International Geocsience and Remote Sensing Symposium (IGARS 93), Tokyo, Japan 18-21 August 1993, pp. 980-984.

Bemmelen, R.W. van, 1949. The Geology of Indonesia, Vol Ia. General Geology, Martinus Nijhoff, 732 pp, The Hague.

Bitelli, G., Bonsignore, F., Unguendoli, M., 2000. Levelling and GPS networks for ground subsidence monitoring in the southern Pro Valley, Journal of Geodynamics, 30(3):355-369.

Delinom, R.M., and Suriadarma, A., 2010. Groundwater flow system of Bandung Basin based on hydraulic head, subsurface temperature, and stable isotopes. Riset Geologi dan Pertambangan 20(1):55-68.

Zebker, H.A. and Villasenor. J, 1992. Decorrelation in interferometric radar echoes. IEEE Trans. Geosc. Remote Sen. 30, 950-959.

Wangsaatmaja, S., Sutadian, A.D., and Prasetiati, M.A.N, 2006. A summary report of research on sustainable water management in Asia, Institute for Global Environmental Strategies, pp. 46-59.

Suhari, S. and Siebenhuner, M., 1993. Environmental geology for land use and regional planning in the Bandung Basin, West Java, Indonesia. Journal of Southeast Asian Earth Sciences, V. 8, 1-4, pp. 557-566.

Lixin, Y., Fang, Z., He, Z., Shijie, C., Wei, W., and Qiang, Y., 2011. Land subsidence in Tianjin, China. Environ Earth Sci. 62:1151–1161

Li, Z.W., Ding, X.L., Huang, C., Zheng, D.W., Zou, W.B., and Shea, Y.K. : Filtering method for SAR interferograms with strong noise, *International Journal of Remote Sensing*, 27, pp. 2991-3000, 2006.

Werner, C., Wegmuller, U., Strozzi, T., and Wiesmann, A., 2000. Gamma SAR and interferometric processing software, Proceedings of ERS-ENVISAT Symposium, 16-20 October, Gothernburg, Sweden.

Chapter 4

Surface Heave Estimation at Oil Sands Field by Stacking Differential SAR Interferograms

Abstract — *The surface heave rate at oil sands field due to steam assisted gravity drainage (SAGD) has been estimated by stacking unwrapped differential SAR interferometry. In lookup table creation for geocoding, the refinement of the lookup table required Landsat-7 Enhanced Thematic Mapper Plus (ETM+) intensity image for coregistration with PALSAR intensity image in order to obtain a high accuracy result. A comparison of three adaptive filtering methods has been further conducted to choose the suitable method for optimally reducing noises over differential interferograms. Once quadratic phase is removed from unwrapped differential interferogram, the stacking is performed to estimate the surface heave rate which the stacking at the same time also removes atmospheric effects. Finally, the surface heave rate estimate is validated with the result of the network of 54 monument surveys.*

4.1 Introduction

It is well known that the subsurface injection of fluid (water, gas, and vapor) can induce surface heave which is also commonly called uplift. Although the fluid injection has been started since a long time ago worldwide for a variety of purposes, e.g. to mitigate anthropogenic land subsidence, recharge overdrafted aquifer system and enhance oil recovery (EOR), the surface heave is less observed and recognized than subsidence. Thermal EOR, such as Steam Assisted Gravity Drainage (SAGD) used in oil sands reservoir containing bitumen, can lead to a surface heave as land response in term both magnitude and areal distribution due to an increase in pore pressure and temperature during injection (Collin 2005). In such case, surface heave may be relatively small so that it is not considered as environmental hazards but may not destruct the engineered structure and infrastructures in short time. Surface deformation can also be used to estimate the steam chamber growth, which is critical to optimize the heavy oil recovery,

to target the stimulation of the reservoir and to identify bypass regions. For these reasons, there is an increasing demand for accurate monitoring of surface heave. The surface deformations are able to be used by a reservoir engineer in order to improve the knowledge of reservoir behavior to enable good decisions that optimize production and mitigate risk.

From 1997 to 2008, conventional geodetic measurements, i.e. the network of 54 monuments surveys were carried out to investigate surface heaves in order to map the deformation due to SAGD process at Hangingstone's oil sand field (JACOS 2009). Even though GPS is one of the most suitable conventional techniques of surface deformation monitoring with a high accuracy, it has some limitations, such as labor intensive, time consuming, and costly. Fortunately, synthetic aperture radar (SAR) interferometry (InSAR) technology provides its capability for imaging the ground surface deformations over large area (several 10s of km) with very small (1 cm or less) surface changes all weather conditions in daylight or at night. Its potential has been proven as a technique for high resolution and high accuracy for topographic mapping (e.g., Graham 1974, Madsen *et al*. 1993, Zebker *et al.* 1994, Sansosti *et al.* 1999) and for monitoring deformation at Earth's surface (Gabriel *et al.* 1989, Massonet *et al.* 1993, Peltzer *et al.* 1995, Ding *et al.* 2004).

In this paper, we present the potential of InSAR technique for estimating accurately surface deformations at small area, i.e., Hangingstone's oil sand field with small deformations undergoing the SAGD process. We then compare our results of InSAR processing to the network of 54 monument survey. Although InSAR technique is a powerful tool, it has also limitations due to noise, which is caused by decorrelation effects and water vapor in the atmosphere. Commonly, InSAR processing for the refinement of lookup table is enough to make use of a simulated SAR intensity image in order to obtain positioning accuracies at sub-pixel level in the automatic registration with the actual SAR image. However, the topography of study area is poor. It can make a simulated SAR intensity generated from a SRTM DEM not well working used to improve the accuracy up to sub-pixel due to a high decorrelation between both images (SAR intensity from PALSAR and simulated SAR intensity from SRTM DEM). In this paper we present how to solve this problem so that the refinement of lookup table significantly improves the accuracy.

Another factor which can limit the accuracy of the deformation estimated from individual differential SAR interferometry (DInSAR) is caused by the atmospheric path delay effect. This atmospheric effect is related to the water vapor which causes error in estimate displacements. Actually, this problem can be overcome by using persistent scatterer interferferometry (PSI). However, the problem with PSI is that large data stacks, e.g. more than 20 scenes, are required (Wegmuller et al., 2009). Regarding availability of the number of scenes, we therefore reduce the atmospheric effect using a stacking technique of unwrapped differential SAR interferogram. Moreover, a main problem in the InSAR processing is presence of residues in the phase unwrapping. Residues are caused by noise over interferogram. Goldstein and Werner (1998), Baran *et al*. (2003), and Li *et al*. (2006) developed the filtering method to reduce noise. So far, no literature presents comparison among these filtering methods based on the ability of the filter in reducing residues. Therefore, we need to compare the filtering methods before unwrapping differential interferogram phase, in order to choose a suitable method for optimally reducing noises over differential interferograms. We have also used other statistical parameters, such as sum of the phase difference (SPD) and normalized standard deviation (NSD), to examine these filtering methods for the interferograms over Hangingstone's oil field which has relatively low coherence due to swampy area. In this study we have used InSAR data acquired by Phase Array type L-band (PALSAR) instrument on the Japanese Advanced Land Observation Satellite (ALOS) "Daichi". As the satellite was launched on January 24, 2006, we have investigated the surface heave from 2007 to 2008 (ERSDAC, 2006).

4.2 Methodology

The main processing steps include SAR processing, interferometric processing, geocoding, topographic phase removal, adaptive filtering, phase unwrapping, quadratic-phase removal, stacking, and conversion of the stacked unwrapped phase to vertical displacement rate. Figure 4.1 shows the processing flowchart of InSAR processing to estimate the map of surface deformation due to steam injection.

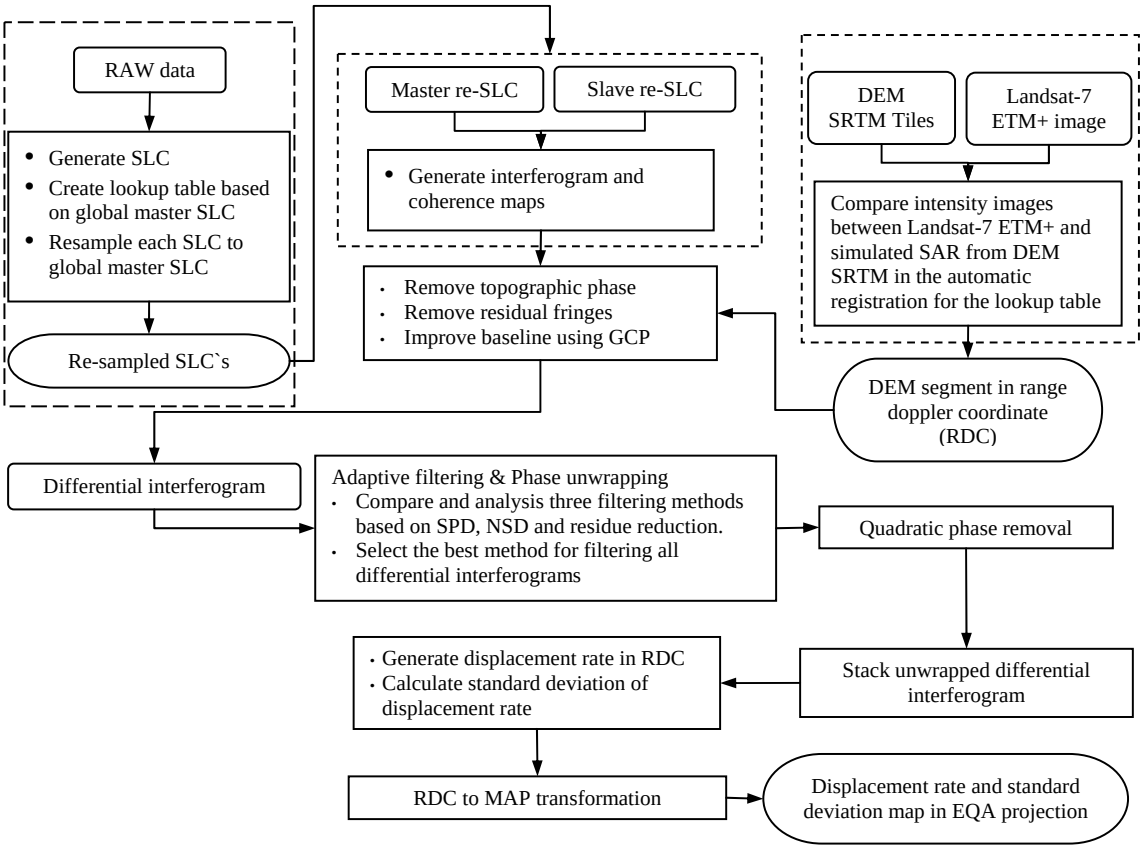

Figure 4.1. Processing flowchart for estimating surface deformations

4.2.1 InSAR Data

In this study we use nine image data level 1.0 for the period from February 9, 2007 to December 30, 2008 (Table 4.1).

Table 4.1. List of PALSAR data used in this study

No	Date acquired	Path/Raw	Mode	Doppler centroid (Hz)
1.	2007/02/09	194/112	FBS	68.6036
2.	2007/06/27	194/112	FBD	72.1220
3.	2007/08/12	194/112	FBD	81.7299
4.	2008/02/12	194/112	FBS	49.2399
5.	2008/05/14	194/112	FBD	70.2395
6.	2008/06/29	194/112	FBD	77.3937
7.	2008/09/29	194/112	FBD	70.1187

The data are the high-bandwidth (FBS, 28 MHz) and low-bandwidth (FBD, 14 MHz) modes from ascending orbits with an off-nadir 34.3 deg. Main advantages of the L-band (23.6-cm wavelength) over C-band (5.6-cm wavelength) are deeper penetration of vegetated areas results in less temporal decorrelation enabling interferogram to have longer time separation and longer baseline increases the critical baseline resulting more usable interferometric pairs.

4.2.2 Interferogram generation

Before generating interferogram, we generated nine Single Look Complex (SLC) images from PALSAR raw data. In order to eliminate the potential of slightly different azimuth imaging geometry and maintain coherency, all images were processed using a common Doppler centroid frequency of 69.1472 Hz. A global master SLC (No. 1 in Table 4.1) was selected and segmented into 4820 pixels wide and 12299 lines long around area covering the oil sands field under SAGD process. The segmentation allows less capacity of memory, less processing time, and clearer visibility of small target area. All other SLC images were then co-registered to the global master SLC in order to make all SLC images having the same geometry. In the interferogram generation, co-registration between master and slave SLC in each interferogram pair was in sub-pixel accuracy with three looks in azimuth and one look in range.

In order to remove parts of the image spectrum which do not contribute to the interferogram, we applied common-band filtering in both range and azimuth direction. Therefore, these filtering can improve the coherence of the interferogram. Once interferogram has been generated, coherence that is the complex correlation between the master and co-registered slave image is calculated over 5x5 pixel window in the pair interferogram. In addition, this coherence is a measure of interferogram quality. This coherence is also very important parameter to adaptive filtering (discussed in the section 4.3.2).

For interferogram generation, we have constructed from images in the FBS-FBS and FBS-FBD pairs. Table 4.2 shows the time interval and perpendicular baseline for each pair.

Table 4.2. Time interval and baseline relative to the master scene

PAIR	Time interval (days)	Perp. baseline (m)
070209_080212	368	3183
070627_080514	322	3079
070627_080629	368	999
070627_080929	460	3619
070812_080629	322	1212
070812_080929	414	3832

4.2.3 Geocoding

Because all images were coregistered to the global master image, we required only one lookup table for geocoding. In geocoding we used Digital Elevation Models (DEM) obtained from SRTM (Shuttle Radar Topography Mission) at 3 arc-second resolution (reference).

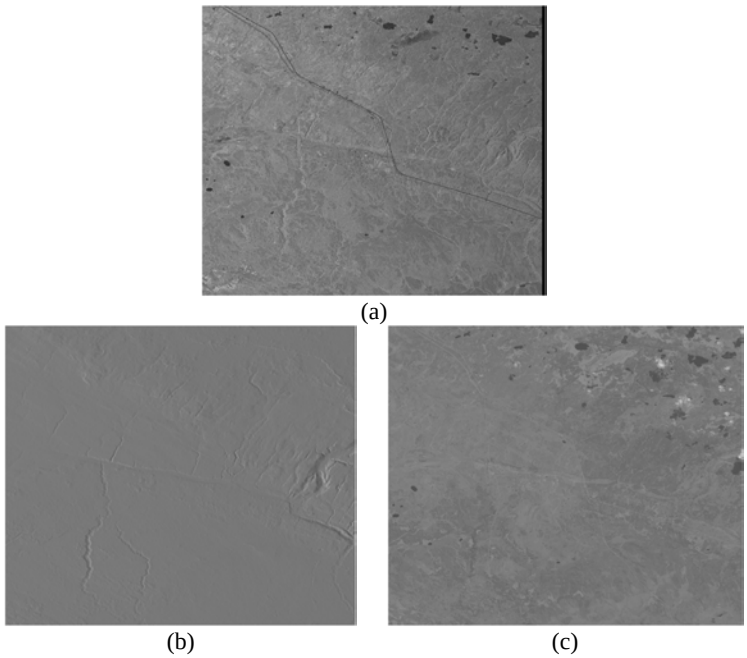

(a)

(b) (c)

Figure 4.2. Intensity Image Comparison: (a) PALSAR Intensity, (b) Simulated SAR intensity from DEM, (c) Landsat ETM+ intensity

In order to cover all target area from InSAR scene, six DEM tiles called N55W111, N55W112, N55W113, N56W111, N56W112, and N56W113 are mosaiced together. Therefore a larger DEM has dimension of 3601 wide x 2401 lines and -8.333333e-04 decimal degrees for the latitude posting and 8.333333e-04 decimal degrees for the longitude posting in EQA projection.

Co-registration between SAR intensity image and simulated SAR intensity image derived from SRTM DEM is required to refine geocoding lookup table with the accuracy of less than 0.3 pixels. In this study, we compared two intensity images between simulated SAR intensity from DEM and Landsat-7 ETM+ in co-registration with PALSAR intensity image when improving the lookup table.

4.2.4 Differential SAR interferometry and adaptive filtering

The basic idea of differential SAR interferometry approach is to separate the topography and displacement related phase term to retrieve displacement maps. We used two-pass differential interferometry approach so that the topography-related phase term was calculated from DEM that is transformed from the EQA projection to radar map. In this processing the topographic phase has to be scaled according to the perpendicular baseline component. Therefore, the precise knowledge of the baseline is very important. The various estimations of baseline applied in this study are based on the orbit data, the fringe rate of the interferograms, and ground control points (GCP).

Once the differential interferogram is generated, the adaptive filtering is applied to reduce the phase noises. If phase noises are not properly removed from interferogram, they will cause pseudo phase residues which play a decisive part in phase unwrapping. There are some filtering techniques developed, such as by Goldstein and Werner (1998), Baran *et al*. (2003), and Li *et al*. (2006). In this paper, we compared and examined their performance using one pair differential interferogram based on normalized standard deviation, sum of phase difference, and ability of residue reduction. In addition, we also visualized their filtering effect to compare smoothness of the differential interferogram from different methods.

Goldstein and Werner (1998) proposed an adaptive radar interferogram filter by multiplication of the Fourier transformed samples Z(u,v) of a small interferogram patch by its smoothed absolute value S{|Z(u,v)|} to the power of an exponent filter parameter α

$$H(u,v) = S\{|Z(u,v)|\}^{\alpha} . Z(u,v) \tag{4.1}$$

The small interferogram patches are overlapped to prevent discontinuities at the boundaries. The filter parameter α varies between zero and one. When α = 0, there is no change in the interferogram. On the other hand, when α = 1 the filtering has the

strongest smoothing over the radar interferogram. In principle, this filtering method uses a constant α for all part of interferogram and depends on noise level of interferogram. A disadvantage of this filter is a difficulty for determining a parameter α when the noise levels are not the same over the interferogram.

Based on Goldstein's filter, Baran et al. (2003) proposed a modification of the filter parameter so that the filtering is more flexible in application. The modified parameter α prevents an area with high coherence from being over-filtered, while at the same time allows strong filtering over area with low coherence. The modification of the filter parameter can be expressed by

$$\alpha = 1 - \bar{\gamma} \tag{4.2}$$

where $\bar{\gamma}$ is the mean coherence value over the corresponding effective patch. However, when no multi-looking and/or multi-looking with few pixels is performed, the interferogram phase noise is normally strong.

Li et al. (2006) developed a filtering method for SAR interferograms with strong noise based on the concept of Vondrák filter (Vondrak, 1969). They extended the one-dimensional Vondrák filter into two-dimensional image space and used the least-squares-based two-dimensional filter to smooth the spectrum $|Z(u,v)|$ in each patch window. The smoothed spectrum is then multiplied by 2D FFT samples $Z(u,v)$, and converted back into the interferogram space IFFT. The *Li* filter can be expressed accordingly as

$$Z'(u,v) = V\left\{|Z(u,v)|, \lambda_1^2, \lambda_2^2\right\} Z(u,v) \tag{4.3}$$

where the smoothing parameters which are functions of local coherence are $\lambda_1^2 = \bar{\gamma}$ and $\lambda_2^2 = \bar{\gamma}/100$. In order to measure the quality of filtered interferograms which shows performance of the filters we used the following criteria: sum of phase difference (SPD) (Li et al., 2004), normalized phase standard deviation (Goldstein and Werner, 1998), and percentage of residue reduction. We also used a coherence image to indicate the quality of interferogram.

Normalized Standard Deviation (NSD)

The standard deviation of the phase is a meaningful measure of interferometric noise and can be estimate directly from interferogram (Goldstein and Werner, 1998) as

$$\sigma_{\phi} = \left(\frac{\sum_{N} (\phi(i,j) - \bar{\phi}(i,j))^2}{N-1} \right)^{\frac{1}{2}} \tag{4.4}$$

Therefore, from Equation (6) we have calculated a normalized standard deviation instead of the standard deviation in order to make the level comparable and it can be expressed by:

$$NSD = \frac{\sigma_{\phi}}{\max(\sigma_{\phi})} \tag{4.5}$$

where $\bar{\phi}(i,j)$ is the local phase gradient over the rectangular estimation window with the edge width 5 (N=25).

Sum of Phase Difference (SPD)

Li et al., 2004 proposed the sum of the phase difference (SPD) as a good quantitative measure for the quality of interferograms. The smaller the SPD is, the better the interferogram quality is. The phase difference between two pixels in neighboring fringes should be very small and infinitesimal value in ideal condition. For a given pixel (central pixel), there are eight pixels around it. In total, there eight phase difference between the central pixel and the neighbor pixel. The sum of the phase difference over entire interferogram can be calculated as follows:

$$SPD = \sum_{x=1}^{p} \sum_{y=1}^{q} APD(x,y) \tag{4.6}$$

where the average phase difference $APD(x,y)$ is defined by

$$APD(x,y) = \frac{1}{8} \sum_{l=-1}^{1} \sum_{k=-1}^{1} \left| \phi(x,y) - \phi(x+l, y+k) \right| \tag{4.7}$$

Percentage of residue reduction

The occurrences of residues in the wrapped phase image is an indication of noise and inconsistent with the smoothness condition. It will yield global phase errors in the unwrapped interferogram (Hanssen, 2001). The most basic evaluation of the smoothness criterion in a digital image is on 2 × 2 neighboring pixels:

$$r = W\left\{\left(\varphi^{w}_{x+1,y} - \varphi^{w}_{x,y}\right)\right\} + W\left\{\left(\varphi^{w}_{x+1,y+1} - \varphi^{w}_{x+1,y}\right)\right\} + W\left\{\left(\varphi^{w}_{x,y+1} - \varphi^{w}_{x+1,y+1}\right)\right\} + W\left\{\left(\varphi^{w}_{x,y} - \varphi^{w}_{x,y+1}\right)\right\} \tag{4.8}$$

where the value of can be zero (no residue), +1-cycle (positive residue) or – 1- cycle (negative residue).

4.2.5 DInSAR stacking

The accuracy of vertical displacements from individual differential interferogram is mainly limited by the atmospheric path delay term. In order to reduce the atmospheric disturbance we use a stacking technique combining multiple observations into a single deformation map. The main assumption of stacking technique is displacements linear for certain time interval. Other assumptions are that the displacement phase is highly correlated and the error terms, such as atmospheric, signal noise, and baseline related, are uncorrelated between the independent pairs. Because the displacement increases with increasing acquisition time interval, interferometric pairs with long acquisition time intervals are preferred to reduce the effect of the atmospheric disturbances. Therefore, we preferably select interferograms with about one year or more acquisition time interval to map the displacement.

4.3 Results and Discussion

4.3.1 Refinement lookup table using Landsat ETM+ image

A simulated SAR intensity is proportional to local incidence angle according to the surface's backscattering phase function (Rosen et al., 1996). Therefore, poor offset estimation between PALSAR intensity and the simulated SAR intensity occurs in area of our study due to a moderate topography. The PALSAR image has many features that can also be observed in the Landsat ETM+ image so that the automatic registration procedure applied to the Landsat ETM+ image instead of the simulated SAR image performed with better accuracy. Comparisons among the PALSAR, the Landsat ETM+, and the simulated SAR images can be seen in Figure 4.2.

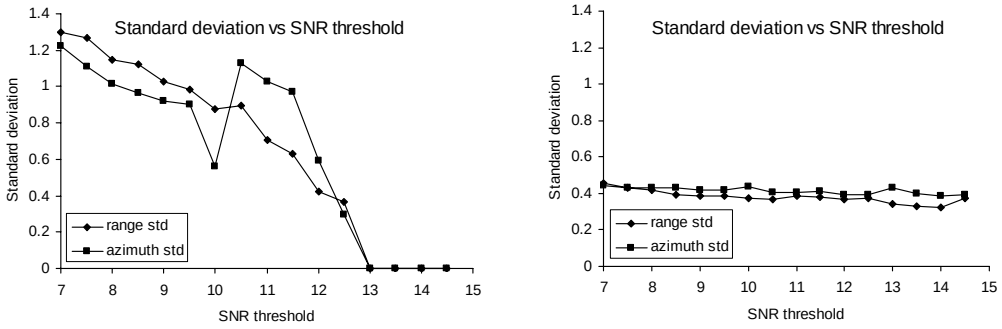

(a) (b)

Figure 4.3. Standard deviation as a function of SNR threshold (a) with simulated SAR intensity and (b) with Landsat ETM+

Standard deviations with SNR threshold variations in co-registration using the Landsat intensity are much lower than using the simulated SAR intensity. From Figure 4.3b, the standard deviation is less than 0.5 when using the Landsat intensity so that the coregistration in sub-pixel accuracy can be achieved. While the coregistration using the simulated SAR is more than one pixel accuracy as shown in Figure 4.3a. On the other hand, a number of fit offsets using Landsat intensity are also more than those of using the simulated SAR intensity. Therefore, the Landsat intensity is much more accurate than the simulated SAR intensity for the lookup table refinement. The comparison of the number of fit offsets can be seen in Figure 4.4.

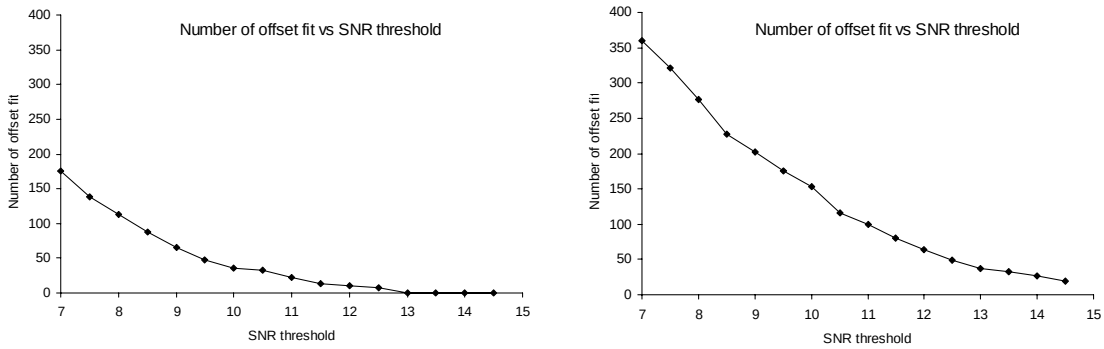

(a) (b)

Figure 4.4. Number of offset fit as function of SNR threshold (a) with simulated SAR intensity and (b) with Landsat ETM+

4.3.2 Comparison of three filtering methods

Coherence, a measure of the phase noise, is defined as the magnitude of the normalized interferogram. In order to make the coherence measure quantitative, a histogram of the coherence image was created as shown in Figure 4.5. Based on this histogram, we can also define a parameter of Goldstein's filter α = 0.7. In addition, we used the filter parameter α of 0.1 to show a performance of this filtering with different parameter α. Two filter parameters for three filtering methods are patch size of 32x32 pixels and overlapped window of 14 pixels. Another parameter for the Goldstein's and Baran's filters is a smoothing operator with a mean kernel of 3x3 pixels.

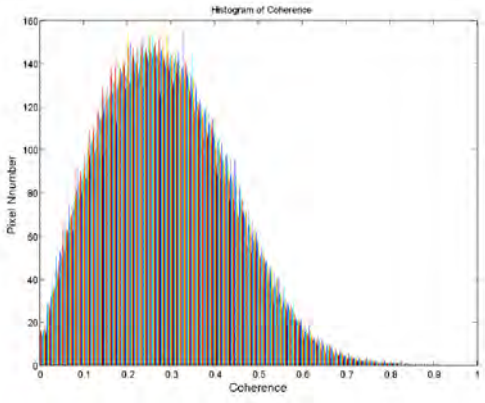

Figure 4.5. Histogram of coherence

Figure 4.6 shows the unfiltered differential interferogram and corresponding coherence respectively. This interferogram is very noisy according to coherence map which has value quite low. The noises will cause problems if they are not properly removed from the interferogram. We compared a normalized standard deviation (NSD) map of filtered differential interferograms in order to distinguish the improvement of filtering from different methods. As shown in the NSD maps, the filtered interferogram with Baran's filter in Figure 4.7c is slightly better than that of Goldstein's filter with α = 0.7 in Figure 4.7b. It can be seen that high NSD value indicated as noises (yellow and red color) over figure 4.7b is less than over figure 4.7c. If we compare the NSD of filtered interferogram using Li's filter to that of other filtering methods, Li's filter is the best filtering showing the lowest noise.

Other criteria to analyze the performance of filtering method are SPD and residue reduction. These statistical analyses are more reliable to evaluate the filtering

performance. Table 4.3 is evaluation results of filtering with different methods. From this evaluation, the reductions in the number of residues resulting from the Li's and Baran's filters are 94% and 91%, respectively. Meanwhile, the reductions resulting from Goldstein's filter with α =0.1 and α =0.7 are 16% and 90%, respectively. Moreover, based on SPD, the improvements of the interferograms filtered with Li's and Baran's filter are 74% and 64%, respectively, while the improvements with Goldstein's filter using α =0.1 and α =0.7 are 6% and 62%, respectively.

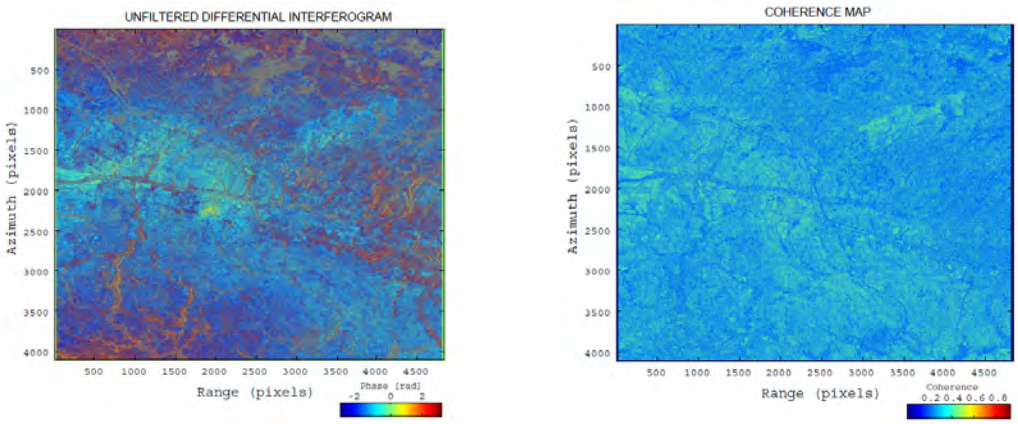

(a) (b)

Figure 4.6. (a) Unfiltered differential interferogram and (b) corresponding coherence image

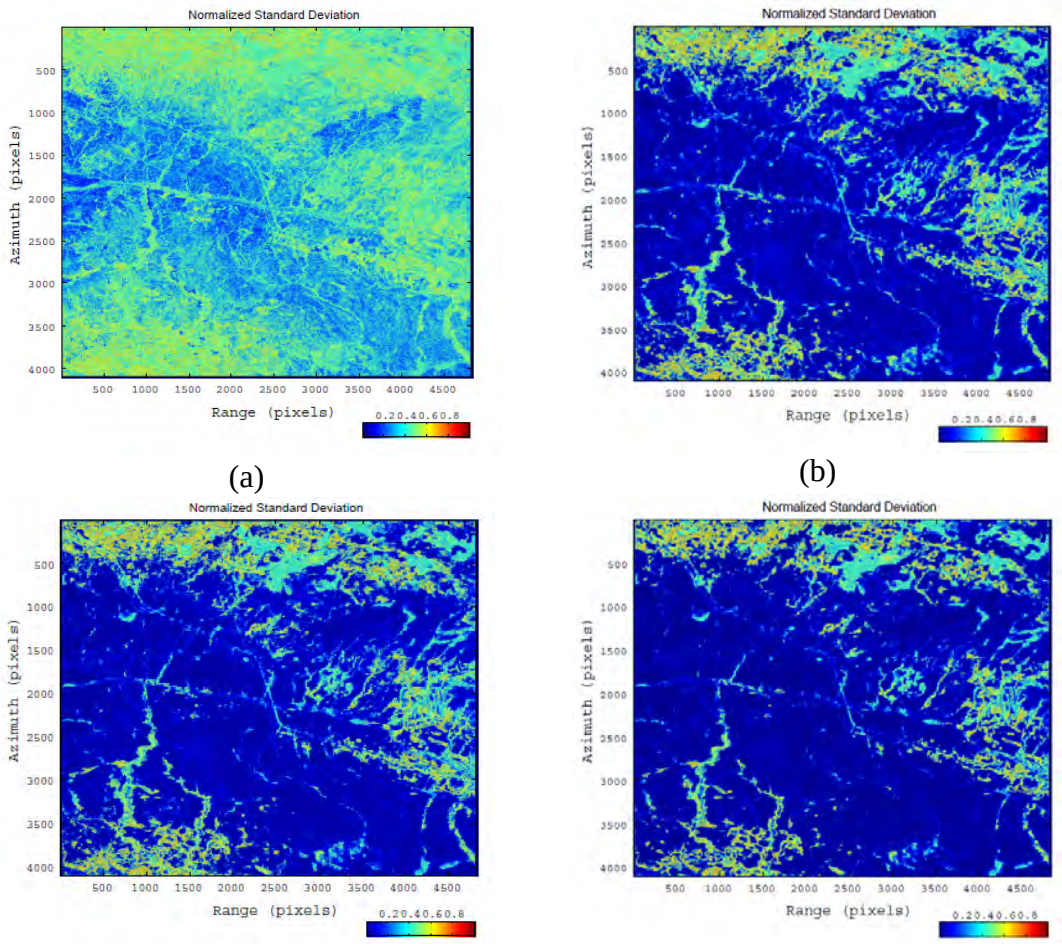

Figure 4.7. NSD for filtered differential interferogram with (a) Goldstein's filter (α=0.1), (b)Goldstein's filter (α=0.7), (c) Baran's filter, (d) with Li's filter

Table 4.3. Evaluation results of filter performance

Filter	Number of residues		Residue reduction (%)	SPD (radians)
	Negative	Positive		
Unfiltered	2560492	2560621	-	3.2965e+007
Goldstein (α=0.1)	2157709	2157799	16	3.1019e+007
Goldstein (α=0.7)	258248	258267	90	1.2466e+007
Baran	226926	226942	91	1.1903e+007
Li	150518	149531	94	8.7456e+006

Comparing Figure 4.8a to Figure 4.6a, it can be seen that Goldstein's filter with $\alpha = 0.1$ does not significantly improve the quality of interferogram. The unfiltered interferogram in Figure 4.6a is almost the same as the filtered version in Figure 4.8a which strong noises are still present. However, the filtering results with Goldstein's filter with $\alpha = 0.7$, with Baran's filter, and Li's filter in Figure 4.8b, 4.8c, and 4.8d respectively are much smoother than that of Goldstein's filter with $\alpha = 0.1$. From these evaluation based on three criteria, Li's filter is the most suitable filtering method for reduce noises in our case study.

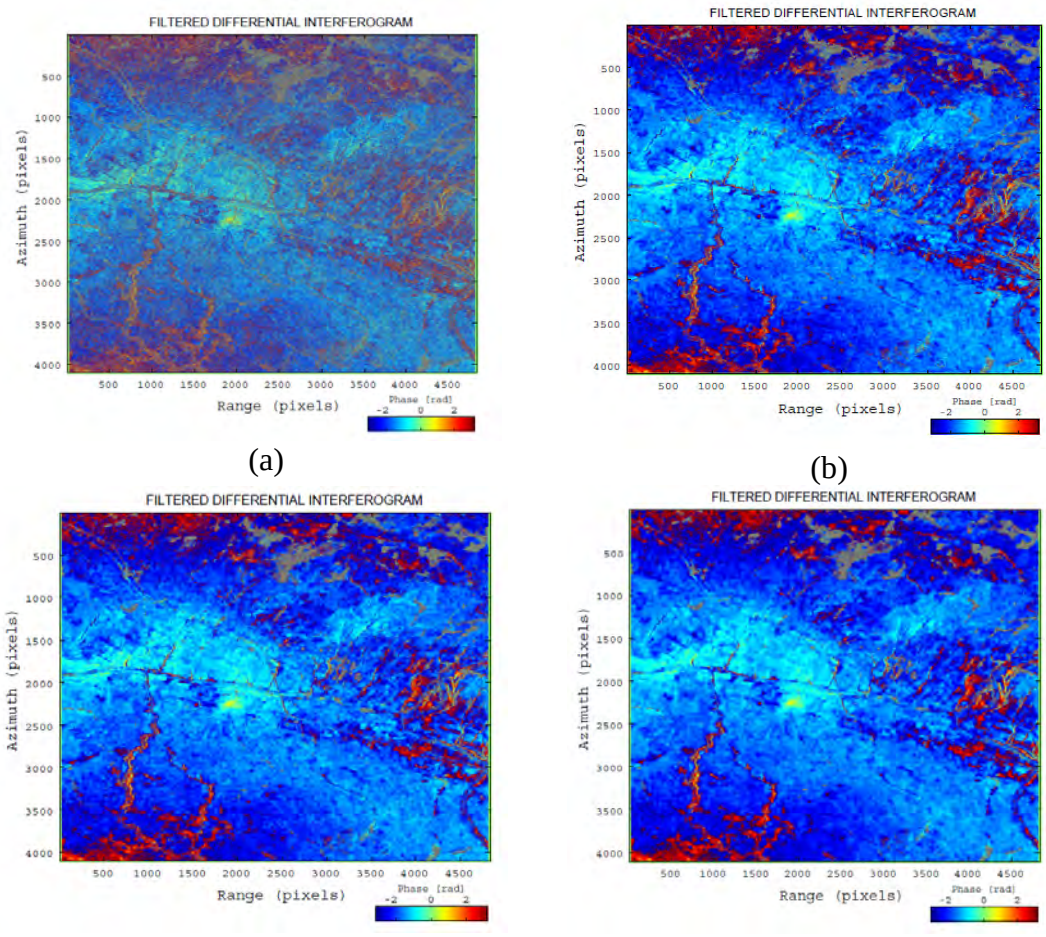

Figure 4.8 Filtered differential interferogram (a) with Goldstein's filter (α=0.1), (b) with Goldstein's filter (α=0.7), (c) with Baran's filter, (d) with Li's filter

4.3.3 Vertical displacement rate from stacking

From the available data in Table 4.1, six independent differential interferograms have been generated to estimate a vertical displacement rate by stacking technique. The vertical displacement rate has been calculated over oil sands field undergoing steam injection from 2007 to 2008. We assume that the displacement over this area is linear as a function of the time. Once quadratic phase was removed from unwrapped differential interferograms, the stacking of six unwrapped differential interferograms has been performed. A result of the stacking has then been converted into a deformation map with maximum vertical displacement of around 3.6 cm/year at the center of deforming area shown in Figure 4.9.

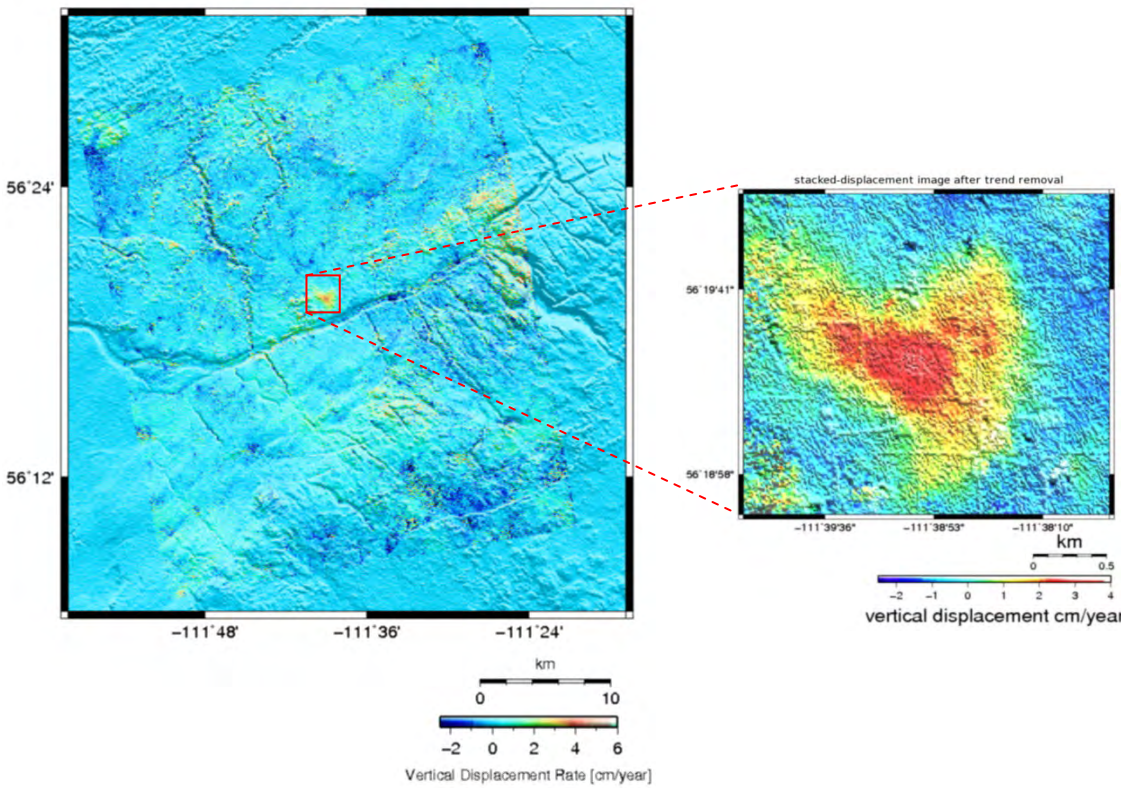

Figure 4.9. A map of vertical displacement rate resulting from the stacking of unwrapped differential interferograms

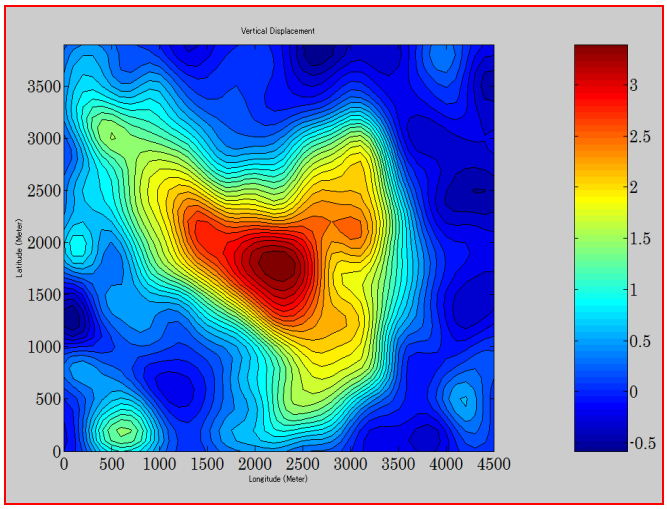

(a)

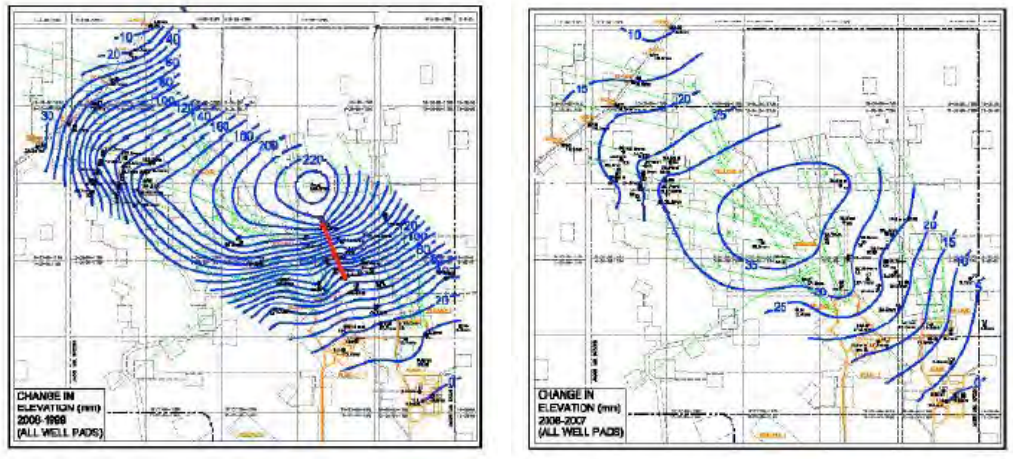

(b) (c)

Figure 4.10. Vertical displacement comparison obtained between (a) by InSAR, (b) and (c) network of 54 monument surveys with time intervals 1999-2008 : max 23.9 cm and 2007-2008; max: 3.9 cm , respectively (JACOS 2009).

A contour of the displacement from our result (upper right in Figure 4.9) has a good agreement with that of leveling surveys in Figure 4.10. This result confirms that differential SAR interferogram stacking is accurately used to estimate the surface displacement due to SAGD activity at oil sands.

4.4 Conclusion

Coregistration of PALSAR intensity with the Landsat ETM+ intensity with higher accuracy than that with the simulated SAR intensity has been performed in the lookup table refinement. The accuracy is less than a half pixels using the Landsat image so that the topographic phase can be properly removed from the interferograms. Finally, the

surface displacements can be precisely estimated.

Based on the evaluation and comparison of three filtering methods by using three criteria, Li's filter is the most suitable filtering methods to reduce noises presenting over differential interferograms, especially for strong noises due to several decorrelation effects.

Surface heave rate of 3.6 cm/year at oil sands field related to steam injection (SAGD) has been accurately estimated by stacking differential SAR interferometry. The pattern of the heave obtained from InSAR technique is a good agreement with that from GPS measurements.

References

Baran, I., Steward, M.P., Kampes, B.M., Perski, Z., and Lilly, P. : A modification to the Goldstein radar interferogram filter, *IEEE Transactions on Geoscience and Remote Sensing*, 41, pp.950-959, 2003.

Collins, P.M., Geomechanical effects on the SAGD Process, paper SPE/PS-CIM/CHOA/PS2005-97905, *the 2005SPE International Thermal Operations and Heavy Oil Symposium*, Calgary, Alberta, Canada, 1-3 Nov. 2005, 2005.

Ding, X.L., Liu, G.X., Li, Z.W., Li, Z.L., and Chen, Y.Q. : Ground subsidence monitoring in Hong Kong with satellite SAR interferometry, *Photogrammetric Engineering and Remote Sensing*, 70, pp. 1151-1156, 2004

ERSDAC, PALSAR user's guide, 1st Edition, March 2006.

Gabriel, A.G., Goldstein, R.M., Zebker, H.A. : Mapping small elevation changes over large areas: Differential radar interferometry, *J. Geophys. Res.*, 94, pp. 9183-9191, 1989.

Goldstein, R.M., and Werner, C.L. : Radar interferogram filtering for geophysical applications, *Geophysical Research Letters*, 25, pp. 4035-4038, 1998.

Graham, L. : Synthesis interferometric radar for topographic mapping, *Proc. IEEE*, 62, pp. 763-768, 1974.

JACOS : Hangingstone demonstration project, *Thermal In Situ Scheme Progress Report, Approval* No. 8788G, presented on March 23, 2009.

Li, Z.L, Zou, W.B., Ding, X.L., Chen, Y.Q., and Liu, G.X. : A quantitative measure for the quality of InSAR interferograms based on phase differences, *Photogrammetric Engineering and Remote Sensing*, 70, pp. 1131-1137, 2004.

Li, Z.W., Ding, X.L., Huang, C., Zheng, D.W., Zou, W.B., and Shea, Y.K. : Filtering method for SAR interferograms with strong noise, *International Journal of Remote Sensing*, 27, pp. 2991-3000, 2006.

Madsen, S.N., Zebker, H.A. and Martin, J. : Topographic mapping using radar interferometry: processing techniques, *IEEE Transactions on Geoscience and Remote Sensing*, 31, pp.246-256, 1993.

Massonet, D., Rossi, M., Carmona, C., Adragna, F., Peltzer, G., Feigl, K.L., and Rabaute, T. : The displacement field of the Landers earthquake mapped by radar interferometry, *Nature*, 364, pp. 138-142, 1993.

Peltzer, G., and Rosen, P. : Surface displacement of the 17 may 1993 Eureka Valley, California, earthquake observed by SAR interferometry, *Science*, 268, pp. 1333-1336, 1995.

Rosen, P.A., Hensley, S., Zebker, H.A, and Webb, F.H. : Surface deformation and coherence measurement of Kilauea Volcano, Hawaii, form SIR-C radar interferometry, *J. Geophys. Res.*, 101, pp. 109-125, 1996.

Sansosti, E., Lanari, R., Fornaro, G., Transceschetti, G., Tesauro, M., Puglisi, G., Coltelli, M. : Digital elevation model generation using ascending and descending ERS-1/ERS-2 tandem data, *Int. J. Remote Sensing*, 20, pp. 1527-1547, 1999.

Vondrak, J. : A contribution to the problem of smoothing observational data, *Bulletin of Astronomical Institute of Czechoslovak*, 20, pp. 349-355, 1969.

Zebker, H.A., Werner, C.L., Rosen, P.A., and Hensley, S. : Accuacy of topographic maps derived from ERS-1 interferometric radar, *IEEE Transactions on Geoscience and Remote Sensing*, 32, pp.823-836, 1994.

Chapter 5

The Geomechanical Inversion of Surface Deformation Data for Oil Sand Reservoir Monitoring

Abstract — *To estimate distribution of reservoir deformations and reservoir volume change in the oil sand reservoir undergoing steam injection, we apply geomechanical inversion to the surface uplift derived from a differential InSAR (DInSAR) stacking technique. As a geomechanical inversion, we propose two-step inversion scheme based on a tensional rectangular dislocation model. In the first step of the inversion, we use genetic algorithms to estimate the depth and rough deformation of the reservoir. The depth of the oil sand reservoir estimated from the inversion is well consistent with depth of injected point. Secondly, the least square inversion with the penalty function and smoothing factor is used to efficiently invert the distribution of reservoir deformation and volume change from the surface uplift data. These results demonstrate that the InSAR technology is useful to provide ground surface deformations and accurately monitor reservoir deformation using inversion techniques.*

5.1 Introduction

Underground geomechanical instabilities due to rock and fluid manipulation, such as ground water withdrawal, geothermal exploration, steam injection and waste water injection, can induce deformation in reservoirs. This reservoir deformation is largely induced by the change of reservoir pressure and consequently generates measurable surface deformations as subsidence and/or uplift. Excessive surface deformations can result in significant economic losses because of the failure of ground surface structures such as well casings, pipelines, and other underground utilities (Hu *et al*. 2004). In the oil and gas industry, one of the large subsidence cases was observed at the Wilmington field located near Los Angeles, California. The oil production at this field was started in 1936 and the total subsidence reached more than 9 m by 1968 (Nagel 2001). The deformation of reservoir in the chalk formation at the Ekofisk field in Norway resulted

in casing failures (Hermansen *et al*. 2000; Du and Olso 2001; Nagel 2001). The other examples of deformations at oil fields were compaction at the South Belridge field in California causing casing failure (Dusseault *et al*. 2002) and surface subsidence as high as 30 cm per year at the Lost Hills field causing damages of hundred of wells (Du and Olso 2001).

Teatini *et al*. (2011) presented the fundamental geomechanical processes that govern land uplift due to fluid injection in the subsurface for a variety of purposes, e.g. to enhanced oil recovery (EOR), store gas in depleted gas/oil fields, recharge overdrafted aquifer system (ASR), and mitigate anthropogenic land subsidence. The largest uplift depends on a number of factors, including the fluid pore pressure increase, the depth, thickness and areal extent of the pressurized and heated geological formation.

GPS is one of the most suitable conventional techniques of surface deformation monitoring because it has not only high accuracy, but also provides three components of surface deformation (Dixon *et al*. 1997). However, GPS surveys over a large area are labor intensive and time consuming. Fortunately, a modern geodetic method, Synthetic Aperture Radar Interferometry (InSAR) technology, provides its capability for imaging the ground surface deformations over large area with small (1 cm or less) surface changes in all weather conditions (Burgmann *et al*. 2000). Klees and Massonnet (1999) discussed the potential applications of InSAR for the monitoring of deformations related to earthquake and crustal studies, the monitoring of volcanoes and anthropogenic effects, and the monitoring of glaciers and ice sheets. Meanwhile, some examples where surface deformation monitoring using InSAR due to fluid injection were carried out are the Belridge and Lost Hills fields in California (Patzek and Silin 2000; Patzek *et al*. 2001) and the CO_2 sequestration at Krechba Algeria (Mathieson *et al*. 2009).

Because the surface uplift is induced by reservoir expansion, the surface uplift has valuable information about the dynamic reservoir and is most likely to occur in the production of hydrocarbon even if the reservoir is in kilometers deep. Characterization of the surface deformation sources based on the InSAR measurements has therefore become major importance in reservoir monitoring activity, such as EOR, carbon capture and storage (CCS) project. The amplitude and the rate of surface deformation are key parameters for optimum economical production and for minimum environmental impact.

One of the most common applications of these measurements is to numerically or analytically simulate the source of deformation.

There are some source models to be able to simulate the surface deformation, such as the point source (Mogi 1958), the ellipsoidal source (Yang *et al*. 1988), and the rectangular source (Okada 1985). The first two source types are commonly used for volcano and reservoir modeling (Delaney and McTigue 1994; Opplier *et al*. 2005; Fialko and Simons 2000). Meanwhile the last is mostly used for volcanic and earthquake events (Anderssohn *et al*. 2009; Jonsson *et al*. 2002). A pure volumetric dilation source gives rise to a distribution of monopolar vertical displacement, whereas a shear distortion gives rise to a dipole (Dusseault and Collins 2008). For reasonably well-constrained cases, such as a single flat-flying reservoir, the surface deformation can be inverted to give a distribution of volume changes at the depth of the reservoir horizon.

In this study, we propose a two-step inversion scheme from the surface uplift map obtained by InSAR measurement to estimate the distribution of reservoir deformations and reservoir volume change rates where the oil sand reservoir is undergoing steam injection, Steam Assisted Gravity Drainage (SAGD). In the first step, we estimate the geometry of reservoir deformation by inverting the uplift map measured by InSAR adopting Okada source model using genetic algorithm (GA) inversion. In the second step, we use least square method to obtain reservoir deformation, thus reservoir volume changes can then be calculated.

5.2 Methodology

5.2.1 Model of deformation source

Ground surface uplift derived from InSAR provides an excellent opportunity to analyze physical processes of steam chamber development at oil sand reservoir. In order to invert the InSAR derived data, we adopted an elastic, homogeneous, and isotropic half-space with tensile dislocation plane movements. Appling Okada's formula (Okada 1985) to this tensile dislocation model, we can calculate the surface displacements. This formula is non-linear and characterized by a large number of parameters. Also this formula is frequently used in the characterization of earthquake faults. In this study, we

applied the inversion technique to synthetic data and real one of oil sand field under SAGD.

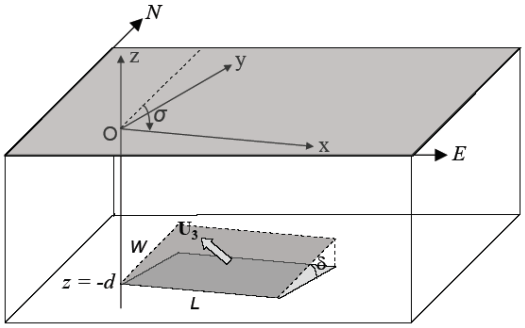

Figure 5.1. Finite rectangular plane dislocation model

Okada (1985) provided analytical expressions to describe the surface deformation due to dislocation for strike slip, dip slip and tensile fault movements. We adopt only the tensile movement of flat reservoir for surface uplift at oil sand field due to SAGD project. The component of vertical displacement (u_z) can be expressed by:

$$u_z = \frac{U_3}{2\pi}\left[\frac{\tilde{y}q}{R(R+\xi)} + \cos\delta\left\{\frac{\xi q}{R(R+\eta)}\tan^{-1}\frac{\xi\eta}{qR}\right\} - I_5\sin^2\delta\right]\Bigg\| \tag{5.1}$$

where

$$I_5 = \frac{\mu}{\lambda+\mu}\frac{2}{\cos\delta}\tan^{-1}\frac{\eta(X+q\cos\delta)+X(R+X)\sin\delta}{\xi(R+X)\cos\delta} \tag{5.2}$$

and if cos δ = 0,

$$I_5 = \frac{\mu}{\lambda+\mu}\frac{\xi\sin\delta}{R+\tilde{d}} \tag{5.3}$$

$$\begin{aligned} p &= y\cos\delta + d\sin\delta; \\ q &= y\sin\delta - d\cos\delta; \\ \tilde{y} &= \eta\cos\delta + q\sin\delta; \\ \tilde{d} &= \eta\sin\delta - q\cos\delta \\ R^2 &= \xi^2+\eta^2+q^2 = \xi^2+\tilde{y}^2+\tilde{d}^2 \\ X^2 &= \xi^2+q^2 \end{aligned} \tag{5.4}$$

"$\|$" represents Chinnery's notation, which is represented by the following expression:

$$f(\xi,\eta) = f(x,p) - f(x,p-W) - f(x-L,p) + f(x-L,p-W) \tag{5.5}$$

Notations for the formulas from Eq. (1) to Eq. (5) are listed in Table 5.1.

Table 5.1. Notations of Okada's formulas

Symbol	Quantity
u_z	Vertical displacement at surface
U_3	Vertical deformation in reservoir
$\tilde{y}$, $\tilde{d}$	Coordinates of the fault plane
ξ, η, q	Coordinates of the first point of the fault plane
R	Distance between first point of the fault plane and the origin
X	Coordinate of the point on the fault direction
L	Length of fault patch along strike
W	Width of fault patch along dip

The coordinates of the origin of the fault patch which lies at its lower left-hand corner are E, N, and d, taken positive in East, North, and down direction. We rotate by strike (σ) of the fault in degrees clockwise from North in order to transform the (x,y) coordinate system by Okada (1985).

In this study, we use a horizontal dislocation plane, with the following assumptions: (1) dip angle (δ) is zero; (2) surface deformation component is only vertical (u_z); (3) reservoir deformation component is only vertical (U_3) (Figure 5.1). It is clear that the deformation fields produced by a horizontal fault, $\delta = 0$, do not depend on the medium constants, λ and μ (Okada 1985).

5.2.2. GA inversion for geometry of deformation source

In the earth sciences, many important problems require data fitting and parameter estimation. They can be nonlinear and involve many unknown parameters. Consequently, local optimization methods, e.g., matrix inversion, steepest descent, conjugate gradients are prone to trapping in local minima, and their success depends heavily on the choice of starting model (Boschetti *et al*. 1996). In this paper, we have adopted a global optimization approach based on the use of Genetic Algorithms (Goldberg 1989) to deal with inversion problems. These algorithms are different from other optimization and search procedures in four ways: (1) the GAs work with a coding of the parameter set, not the parameter themselves; (2) the GAs search from a population of points, not a single point; (3) the GAs use payoff (objective function)

information, not derivatives or other auxiliary knowledge; (4) the GAs use probabilistic transition rules, not deterministic rules (Goldberg 1989).

In the proposed two-step inversion, firstly, we applied Genetic Algorithms to estimate reservoir deformation parameters, e.g., geometry (width and length), horizontal (x,y) position, depth, orientation (strike), and uniform magnitude of rectangular vertical deformation from the ground surface uplift obtained by SAR interferometry. GAs are based on the simulation of biological evolution in order to find the fittest individual by defining objective function. Initial population, i.e., the starting model, was randomly generated and subjected to several changes by systematically approaching the best solution among many investigated solutions. The model parameters are represented by binary digits or bit strings. Major GA operators are evaluation, reproduction, cross-over and mutation to allow modification of the population to search the best solution of the reservoir deformation parameters. The searching process is terminated when a number of iterations were achieved as a stopping criterion.

One of important aspects in genetic algorithms is how to specify the model criterion. This criterion is referred to as the misfit. The lower the misfit function, the closer an individual belonging to the population will be the optimal minimum/maximum. In this paper, we adopted the misfit function, which is more appropriate for larger N (Nunnari, 2005), as given by Equation (5.6):

$$J = \frac{\sum_{i=1}^{N} \left(P_i - O_i\right)^2}{\sum_{i=1}^{N} \left(\left|P_i - \overline{O}\right| + \left|O_i - \overline{O}\right|\right)^2} \tag{5.6}$$

In Equation 5.6, N represents the number of data points at surface while O_i and P_i are observed and calculated values of surface deformation, respectively. Furthermore, in order to evaluate the error related with the considered inverse modeling approach, we calculated the root mean square error (RMSE) using Equation 5.7.

$$RMSE = \sqrt{\frac{1}{N}\sum_{i=1}^{N} \left(P_i - O_i\right)^2} \tag{5.7}$$

5.2.3 Least Square inversion for reservoir volume change

Applying the GA inversion, we can estimate the reservoir deformation parameters as described in Section 2.2. However, simple Okada's model provides a single dislocation

with uniform vertical deformation. This uniform deformation cannot provide an adequate representation of the spatially varying vertical deformation in oil sand reservoir. In order to overcome this problem, we used least square inversion at the second step.

The reservoir deformations have discontinuities of normal displacement in homogeneous, isotropic, and elastic half-space. The uplift at a point of the ground surface induced by an arbitrary distribution of reservoir deformations can be expressed by the Volterra formula as

$$u_k(x) = \iint_{\Sigma} U_i(x') G_{ij}^k(x, x') n_j(x') \, d\Sigma(x') \tag{5.8}$$

(Du *et al*. 1992). Here u_k(x) is the ground surface displacement at *x*, U_i(x') reservoir deformation at x', n_j the normal to the surface Σ, and G_{ij}^k the Green's function relating unit reservoir deformation in the *i* direction at x' to the ground surface displacement in the *k* direction at *x*.

In order to invert surface uplift map caused by the reservoir deformation, the considering reservoir deformation plane is divided into small patches. The deformation for each small patch is assumed to be constant. The surface uplifts in Equation 5.8 are linear with respect to the reservoir deformation $U_i(x')$, but nonlinear with respect to the strike and depth of the deformation plane. The input of depth is already estimated by genetic algorithms in the first step of this proposed two-step inversion approach. Moreover, the integral in Equation 5.8 can be discretized into a set of linear equations. The discrete approximation can then be written in matrix form as (Du *et al*. 1992)

$$\mathbf{d} = \mathbf{Gm} \tag{5.9}$$

where **d** is the vector of *n* surface uplift values, **G** is an *n* x *m* matrix of discrete Green's functions, and **m** is the vector of *m* unknown reservoir deformations, which is vertical deformations.

In many cases, the inverse problem becomes ill-posed, and the solution is not unique (Menke 1984). In such case, the inverse problem can be regularized by adding information. This information is translated into a penalty function. The penalty function is added to the objective function which is minimized to estimate the distribution of reservoir deformations:

$$F = \| \mathbf{Gm} - \mathbf{d} \|^2 + \beta^2 \| \mathbf{Hm} - \mathbf{d_0} \|^2 \tag{5.10}$$

where the first term is the norm of the residuals between calculated and observed data, β is a penalty (smoothness) factor that weights a prior information $\mathbf{Hm}=\mathbf{d_0}$ ($\mathbf{d_0}$ are equal to zeros), and **H** is the discrete Laplacian operator. Many functions arising in nature are smooth to a certain degree. The penalty factor β plays the role of trade-off parameter between the fitness and roughness of model. The model roughness is defined by $\|\mathbf{Hm}\|^2$ which increases with decreasing β. On the other hand, the sum of the normalized squared differences (NSSD) is introduced as a function of the model roughness for the variation of the penalty factor β that gives the reasonable model of reservoir deformations.

Once the distribution of reservoir deformations is estimated, a map of volume change at each grid point can be obtained by multiplication the grid size and vertical reservoir deformation in each corresponding grid. From the volume change at each grid, the total volume change can be calculated by summation of individual volume change. In this calculation, only volume changes in vertical direction were assigned to each grid of reservoir.

5.3 Application to Synthetic Model

A main idea of our approach is in the first step to emphasize resolving accurately the depth of deformation source by means of GA inversion. The disadvantage with uniform deformation approach is that the specific dislocation geometry may not provide an adequate representation of the spatially varying reservoir deformation. Therefore, in the first step of our approach, the reservoir deformation is roughly estimated. We then make use of the estimated depth of deformation source as a constraint in the second step by using least square inversion in order to improve the knowledge of the horizontal distribution of reservoir deformation and reservoir volume changes as well.

In order to examine the performance of proposed two-step inversion technique, GA and least square inversion, we prepared a synthetic model of the distribution of reservoir deformation with magnitudes between 1 cm and 4 cm instead of a single dislocation with uniform deformation (Figure 5.2a). There are three uplift maxima in this model, one in the west part of the reservoir, one in the northeast part of the reservoir, and the other in the southeast part of the reservoir. The three uplift maxima are considered to three horizontal injection wells in the reservoir. A volume change due

to the deformation field in this model is 7.36 x 10^4 m^3. The synthetic model extends 2200 m long from east to west and 1600 m wide from north to south with a strike of N90^{o}W. From this synthetic model, we applied forward modeling based on Okada's formula to obtain a synthetic uplift map (Figure 5.2b) and then added a Gaussian noise with mean 0.0 and standard deviation 0.1 cm to the synthetic uplift map in order to generate a map of noisy synthetic uplift (Figure 5.2d) as an inversion input. Furthermore, in order to evaluate the error related with our inverse modeling approach, we compute misfit, root mean square error, and relative error.

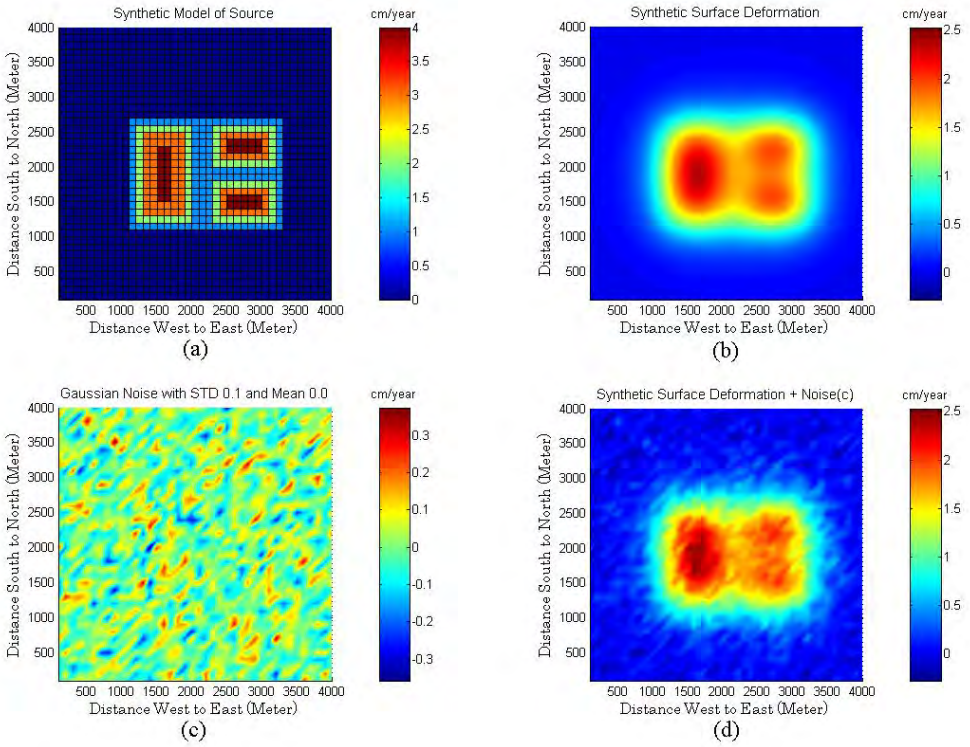

Figure 5.2. (a) Synthetic model of reservoir deformations, (b) synthetic surface uplift resulting forward modeling, (c) additive noise, (d) synthetic surface uplift with additive noise

Using random initial models (Table 5.2.III), we initially applied GA inversion to the synthetic uplift map (Figure 5.2d) in order to resolve model parameters. We evaluated individual of solutions by means of misfit between the observed and calculated surface uplift. Minimizing the misfit means maximizing the performance to find the best solution. The performance of the evaluation for 500 generation can be shown in Figure 5.3a with the least misfit of the solution 0.0324. Besides the fitness, in order to measure the accuracy of the solutions, the root mean square errors (RMSE) of

the solution for 500 generations were estimated as plotted in Figure 5.3b. The RMSE of the best solution is 0.23 cm due to the presence of the additive noise.

Moreover, the complete solutions of GA inversion with the relative error of each modeled parameters are shown in Table 5.2.II. It can be seen that the depth of deformation source has the highest accuracy of all searched model parameters. A relative error of the depth estimation with the range of space search between 100 m and 600 m is 0.2%. It means that GA inversion by using the single dislocation model can accurately estimate the source depth. For vertical reservoir deformation, it is difficult to compare between model and GA inversion solution due to the model deformation varying over reservoir. Therefore, for simplification, we use the average value of synthetic model deformation as comparison to the deformation obtained from globally GA solution. This reservoir deformation was estimated with the relative error as much as 23.4%. It is, however, not reliable due to single deformation over reservoir. The surface uplift obtained from forward modeling of GA inversion solution (Figure 5.3c) is quite different from synthetic model in the shape (Figure 5.2b). A number of uplift maxima are three in the synthetic data and one in the resolved model. We note that reservoir deformation from GA inversion is considered as a rough estimation.

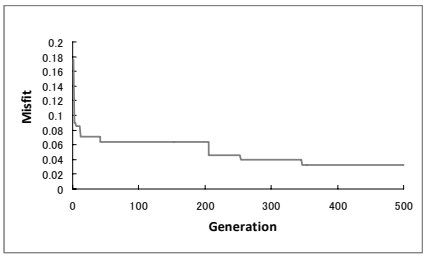

(a)

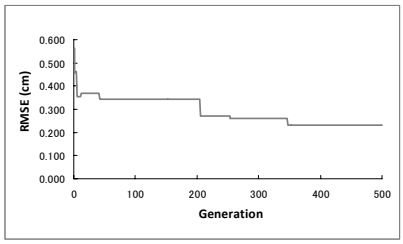

(b)

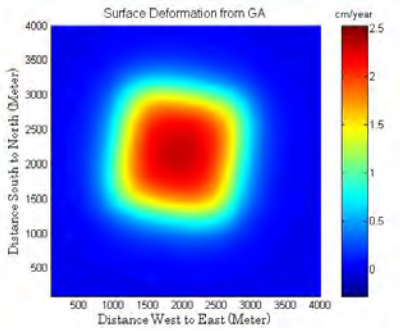

(c)

Figure 5.3. (a) Misfit, (b) RMSE, and (c) surface uplift resulting from the solution of GA inversion.

Table 5.2. Inversion parameters

I.	**Synthetic Model Parameters**	
1.	Length	2200 m
2.	Width	1600 m
3.	Depth of deformation source	500 m
4.	Vertical reservoir deformation (average value of Figure 5.2a)	2.09 cm
5.	(x,y)-position	(3300, 2700) m
6.	Strike	270 deg

II.	**Inversion Results**		**Relative Error (%)**
1.	Length	1667 m	24.2
2.	Width	1700 m	6.3
3.	Depth of deformation source	499 m	0.2
4.	Vertical reservoir deformation	2.58 cm	23.4
5.	(x,y)-position	(2887 m, 2887 m)	(12.5, 6.9)
6.	Strike	279 deg	3.3

III.	**Initial Model**	
1.	Length	500 - 3000 m
2.	Width	500 - 2400 m
3.	Depth of deformation source	100 - 600 m
4.	Vertical reservoir deformation	0 – 4.00 m
5.	(x,y)-position	(0 - 4000, 0 - 4000) m
6.	Strike	0 - 360 deg
7.	Crossover probability	0.7
8.	Mutation probability	0.4
9.	Number of generation	500
10.	Number of individual	800

In order to improve the solution of reservoir deformations from homogeneous into heterogeneous fields, we applied least square technique in the second step of the proposed inversion. The deformation distributions should become more realistic and produce good fit the model. In this step, the reservoir of the synthetic model is divided into grids of rectangular elements in W-E and S-N directions. We assumed that the deformations are uniform in each rectangular element. We used a penalty function with smoothing factors (β) in this least square inversion in order to search for the optimum distribution of reservoir deformation. From the larger smoothing factor, we obtained the smoother vertical reservoir deformation. However, normalized sum-squared differences (NSSD) become larger. Therefore, we needed to investigate a trade-off curve between the roughness of deformation distribution and the NSSD with smoothing factor variation (Figure 5.4). Based on the trade-off curve, we chose the optimum smoothing

factor of 0.19 to obtain the best solution of the distribution of reservoir deformations in this case (Figure 5.5c).

More detail results of the least square inversion are shown in Figure 5.5. When using smoothing factors (β) less than 0.19 (optimum value), we obtained three major deformed areas clearly as shown in Figure 5.5a and 5.5b. These major deformed areas can be separated each other as shown in the synthetic model (Figure 5.2b). However, the deformation distributions are quite different from that of the synthetic model. On the other hand, using smoothing factor (β) larger than 0.19, the inversion cannot resolve three major deformation areas, such as in Figures 5.5d and 5.5e.

In order to evaluate the performance this inversion, we forwarded the inversion results to obtain surface uplift maps. The calculated surface uplift map (Figure 5.6c) is closed to the synthetic model one in Figure 5.2b. We then calculated the residuals between the synthetic model and the calculated surface uplift. The residual map in Figure 5.7c is comparable to the input of noise in the synthetic model (Figure 5.2c). The root mean square errors (RMSE) are also plotted with smoothing factor variation as shown in Figure 5.4b. The RMSE with the optimum smoothing factor is 0.114 cm, meanwhile the standard deviation of the additive noise is 0.100 cm. Moreover, the residual map in Figure 5.7c is also closed to the input error in our synthetic model. These errors are comparable; therefore this approach is acceptable and we can apply it to the real data of oil sand field. Based on these two-steps inversion examination using the synthetic model, we can summarize that the proposed approach shows a good ability to estimate deformation parameters described above.

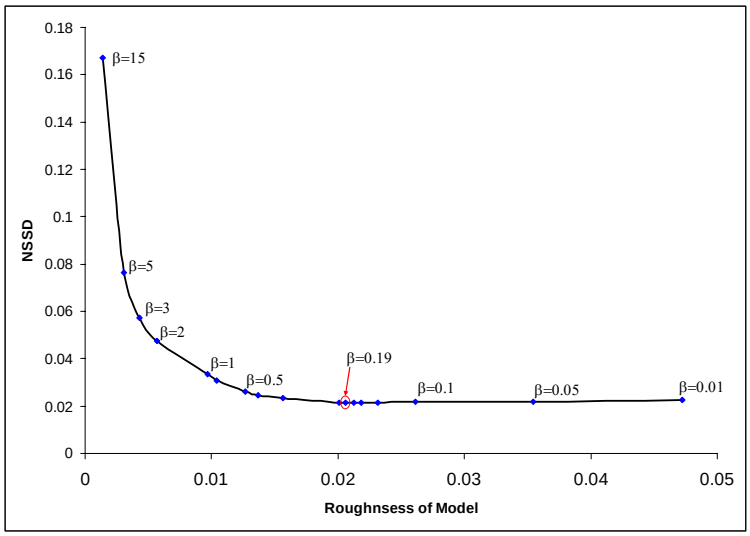

(a)

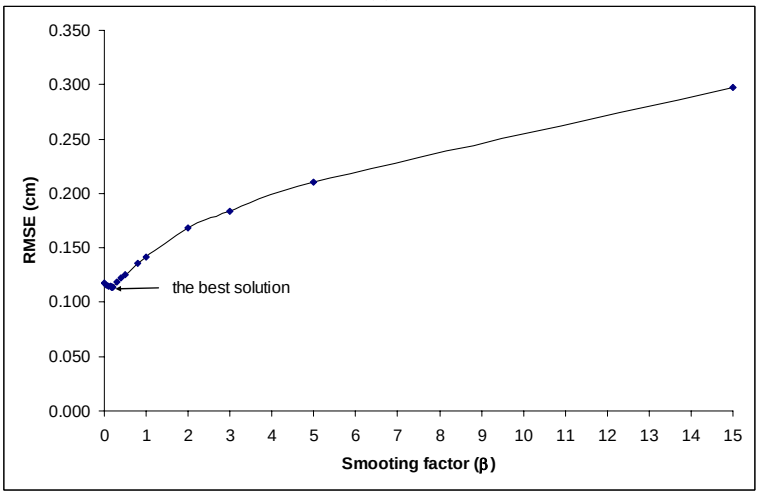

(b)

Figure 5.4. (a) Trade-off curve between roughness and NSSD of solution for synthetic data, (b) RMSE of least square inversion solution with smoothing factor variation.

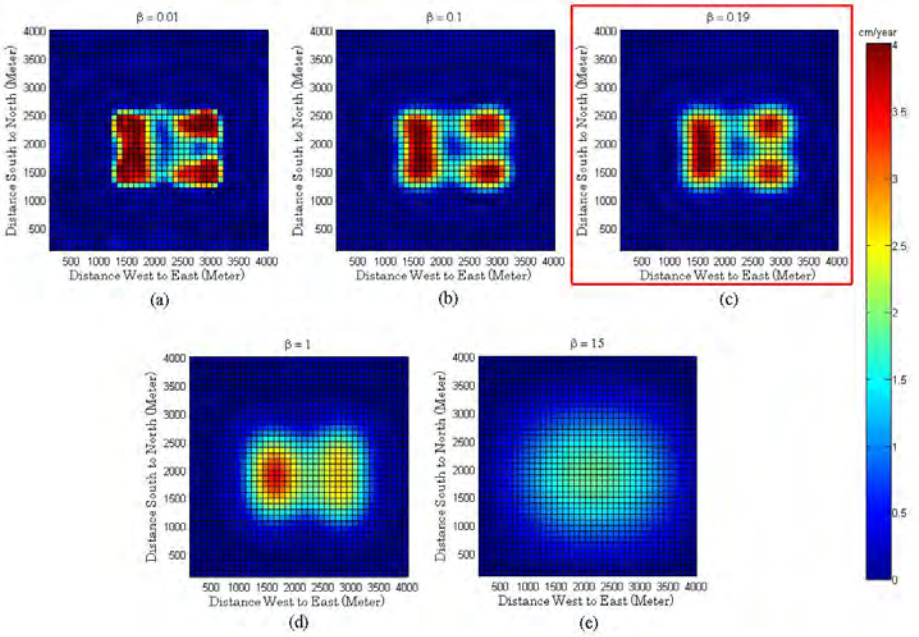

Figure 5.5. Modeled reservoir deformations resulting from least square solution with the variation of smoothing factors of (a) 0.01, (b) 0.1, (c) 0.19, (d) 1.0 and (e) 15.

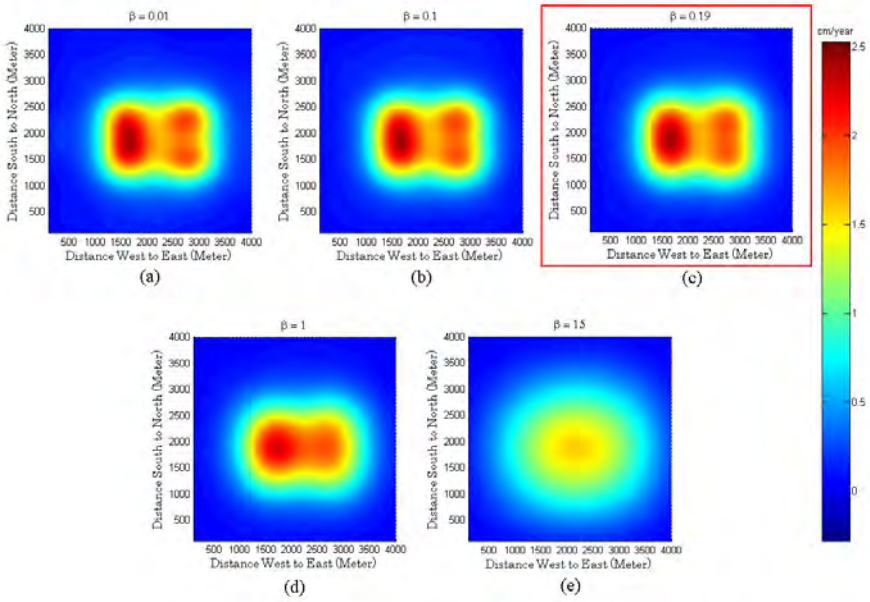

Figure 5.6. Surface uplift maps resulting from the solution of least square inversion with the variation of smoothing factors of (a) 0.01, (b) 0.1, (c) 0.19, (d) 1.0 and (e) 15.

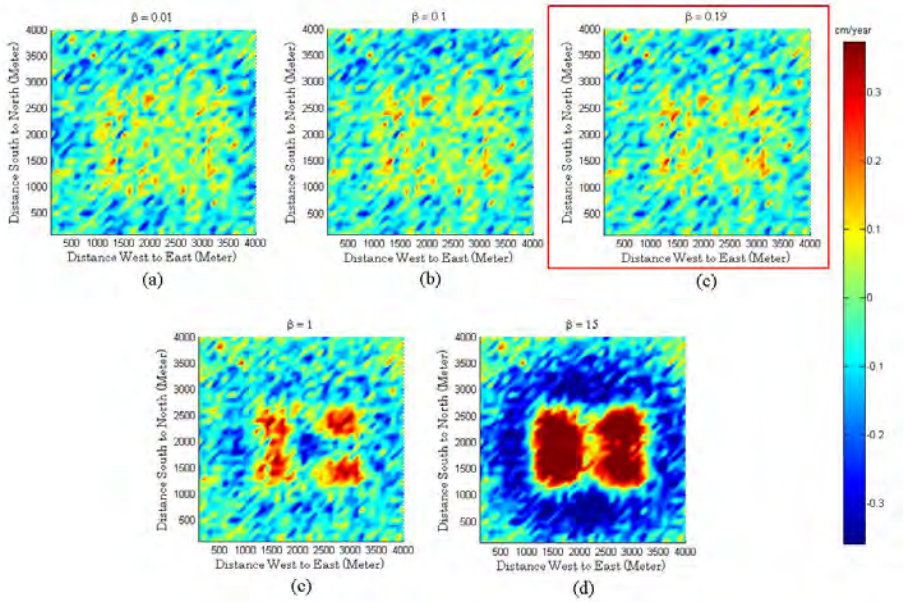

Figure 5.7. Residual between the noisy synthetic uplift and the calculated uplift from the solution of least square inversion with the variation of smoothing factors of (a) 0.01, (b) 0.1, (c) 0.19, (d) 1.0 and (e) 15.

5.4 Application to oil sand field data obtained from InSAR

InSAR deformation map estimated by the stacking technique from six interferograms was inverted by the proposed two-steps inversion method. Figure 5.8a shows the observed vertical surface displacement map and Figure 5.8b shows the modeled vertical surface displacement map which was estimated by GA inversion at first step. We constrained the lower and upper bounds of length, width, depth, chamber development and strike of the dislocation plane (considered as steam chamber in this case) to 800-3,000 m, 800-3,000 m, 200-300 m, 0-1 m and 0^{o}-360^{o}, respectively in search space. We also considered the dip angle of zero as one of the inversion parameters and used the initial population of 800 individuals and a number of generations are 500. After all parents had been paired off from selected population, a random number between 0 and 1 was generated. This random number was compared to a specified crossover probability of 0.7. If the number was less than the crossover probability, the two parents were crossed over. Position of crossover in which part of the right crossover bit-string is exchanged between parents was also randomly selected along the bit-string representation.

Like crossover operation, mutation also needed probability to maintain some random character in the search process. We specified the mutation probability of 0.4;

therefore, if a random number is less than the mutation probability, a tested bit was flipped in parity. From the genetic algorithm, we obtained the best-fit model predicted the rectangular dislocation plane with length, width and depth of 2,413 m, 1,533 m and 297 m, respectively with RMSE of 0.627 cm. The depth of deformation source is in good agreement with real data related to the depth of injection wells (Figure 5.8c).

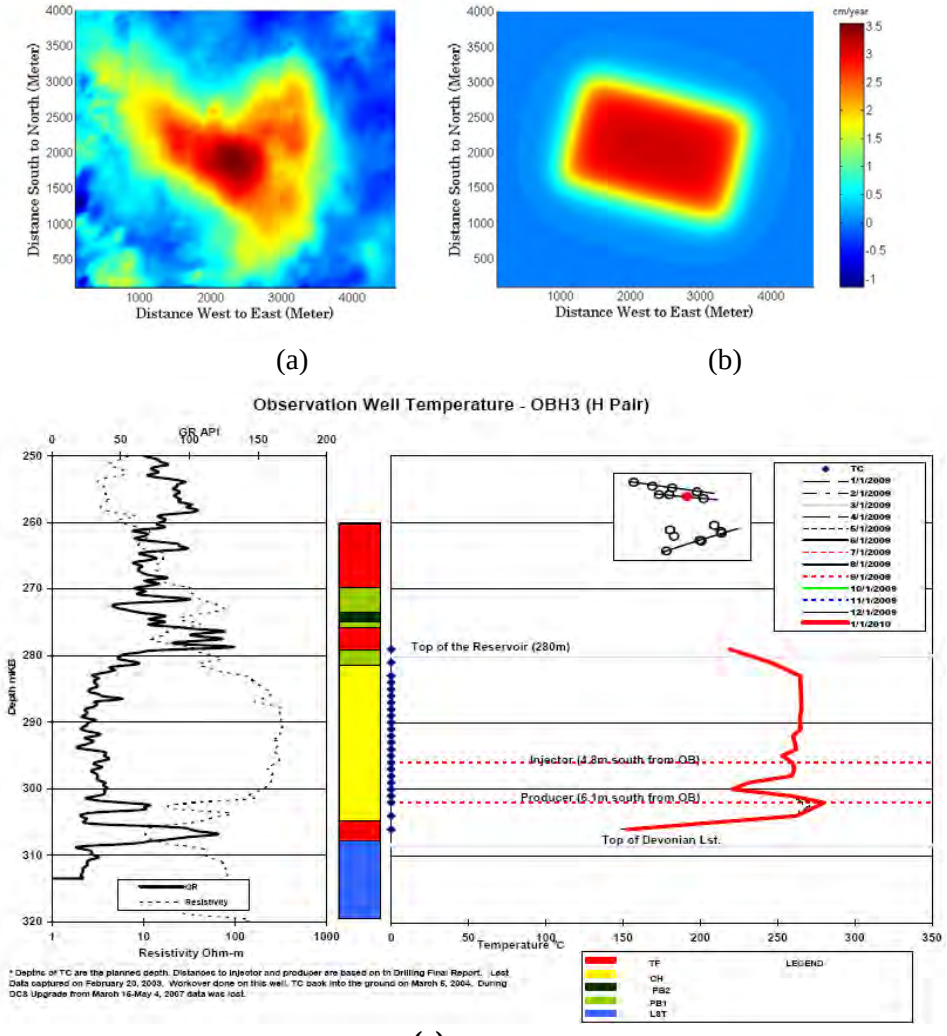

Figure 5.8. (a) Observed surface vertical displacement from InSAR data, (b) Modeled vertical surface displacement from GA, (c) Borehole data showing the depth of injection (JACOS, 2009).

To estimate the detailed deformation of the reservoir from observed-surface-uplift data obtained SAR interferometry measurement, we used a penalty function technique in least square inversion as the second step of our approach (Du *et al*. 1992). The best-fit-single dislocation plane model from the genetic algorithm inversion was enlarged to 4.6

x 4.0 km horizontal dislocation plane. The enlarged-dislocation plane was then discretized into 100 x 100 m patches for inversion of distributed-source deformation. This deformation is interpreted as steam-chamber development under SAGD process. In this study, we used penalty function technique with five smoothing factors, i.e. 0.001, 0.01, 0.1, 1, and 10. Based on analysis of trade-off curve between roughness and NSSD in Figure 5.9, the source deformation rate (Figure 5.10c) is the best solution with smoothing factor of 0.1. For a lowest smoothing factor (0.001) the reservoir vertical deformation rate is highly oscillatory as shown in Figure 5.10a. For a highest smoothing factor (10), however, the reservoir vertical deformation is overly smooth in Figure 5.10e. The reservoir deformation pattern in Figure 5.10c is closely related to well pair locations in Figure 5.10f.

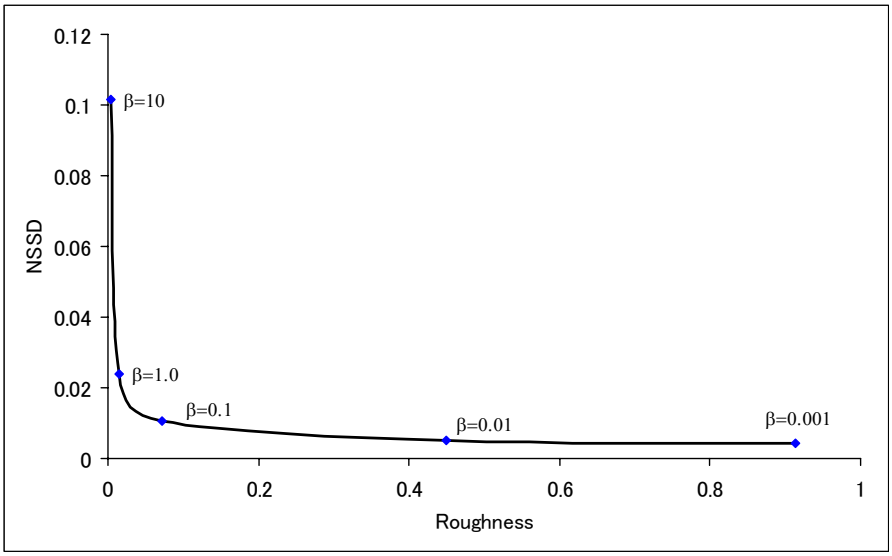

Figure 5.9. Trade-off curve between roughness and NSSD of solution for real data

The map of modeled surface displacement is comparable to the observed uplift in Figure 5.11f in which has a root-mean-square error of 0.125. These small residuals between observed and modeled displacements may be related to some noises in InSAR data. Figure 5.11 also shows the calculated uplift with the smoothing factor variation. Using the larger smoothing factor, we obtained the smoother surface uplift such as shown in Figure 5.11 d and e. On the other hand, applying the lower smoothing factor, the surface uplift becomes similar to the observed uplift. However, the NNSD becomes larger. Furthermore, a map of volume change at each grid point can be obtained by

multiplication the grid size and vertical reservoir deformation in each corresponding grid. Finally, we obtain that the total of volume change rate is 150,809 m^3 a year by summation of individual volume change.. This volume change rate is considered as steam chamber growth during SAGD process.

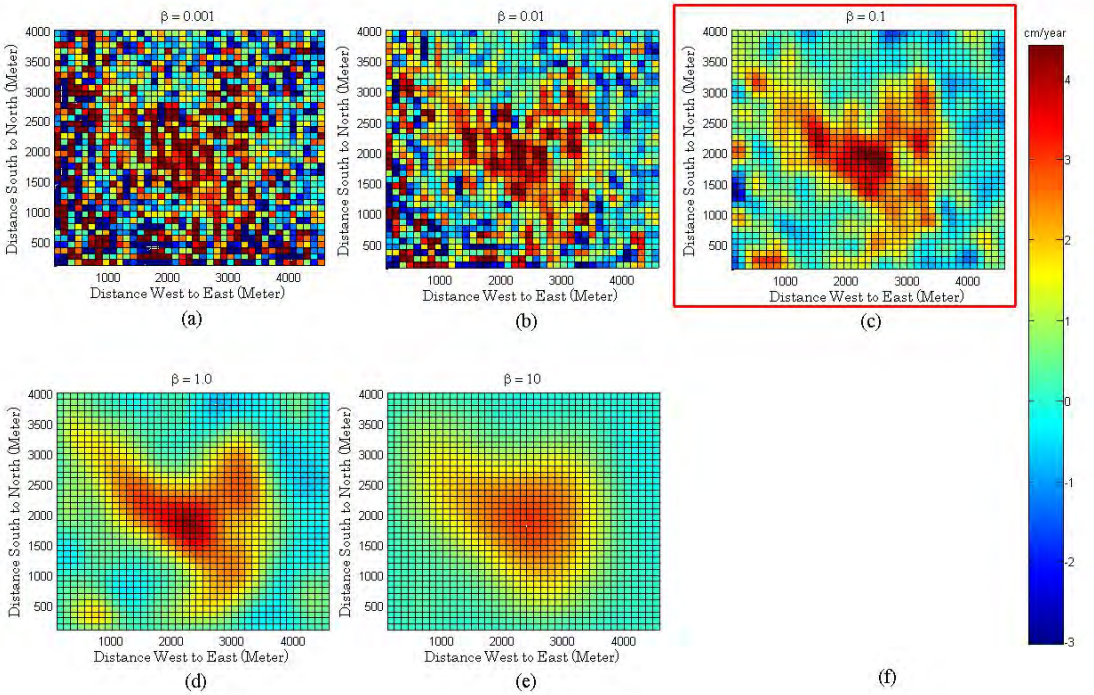

Figure 5.10. Reservoir displacements with the variation of smoothing factors of (a) 0.001, (b) 0.01, (c) 0.1, (d) 1, and (e) 10, and (f) configuration of production and injection wells (JACOS, 2009)

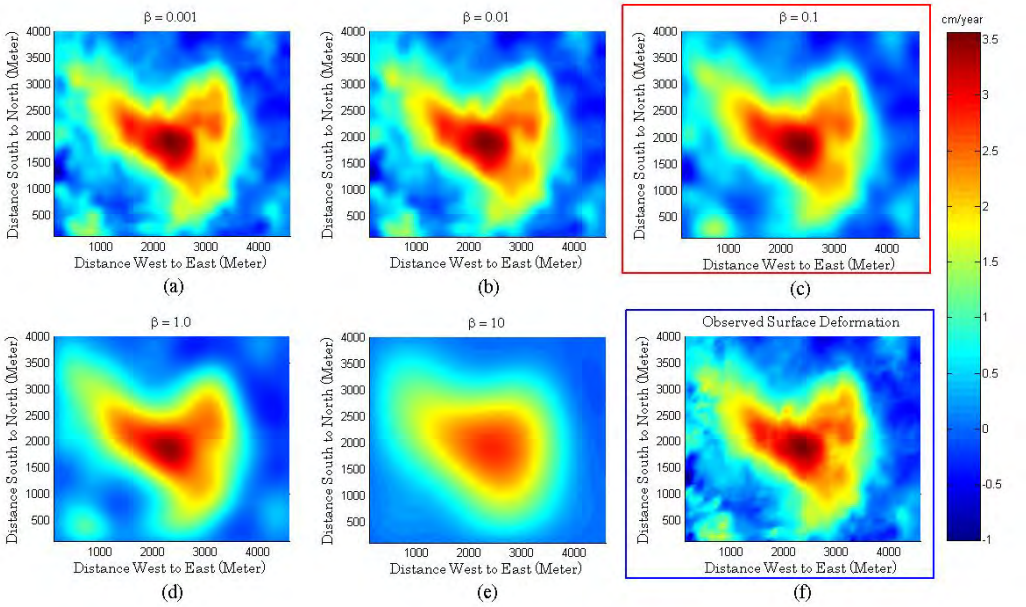

Figure 5.11. Modeled surface vertical displacements with the variation of smoothing factors of (a) 0.001, (b) 0.01, (c) 0.1, (d) 1, (e) 10, and (f) observed data from InSAR

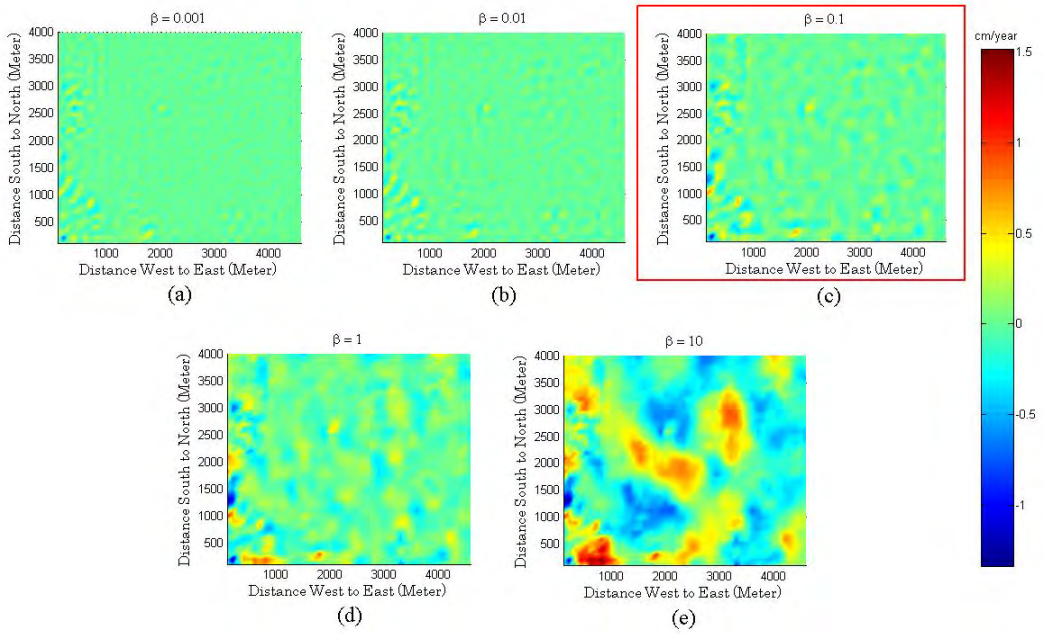

Figure 5.12. Residuals between observed and calculated surface vertical displacements with the variation of smoothing factors.

5.6 Conclusion

In this chapter, in order to evaluate the deformation of oil sand reservoir caused by steam injections, we proposed two-step inversion scheme for InSAR-derived surface deformation data, such as genetic algorithms and least-squares method. We applied genetic algorithm for estimating rough reservoir deformation based on surface vertical uplifts. The result shows that the depth of the target reservoir is a good agreement with the injected point at borehole. We then applied a penalty function technique in least square inversion with smoothing factor to estimate the best vertical deformation rate. Based on this technique, the vertical deformation distribution has a good agreement with the well pair configuration. Finally, we estimated the total volume change rate of 150,809 m^3 a year that corresponds with the growth of steam chamber. Because surface deformation map is frequently obtained from InSAR analysis, we can monitor the growth of steam chamber using our proposed approach.

References

Andersshon, J., Motagh, M., Walter, T.R., Rosenau, M., Kaufmann, H., Oncken, O., 2009. Surface deformation time series and source modeling for a volcanic complex system based on satellite wide swath and image mode interferometry: The Lazufre system, central Andes, Remote Sensing of Environment, Vol.113, pp.2062-2075.

Boschetti, F., Dentith, M.C., List, R.D., 1996. Inversion of seismic refraction data using genetic algorithms. Geophysics, Vol. 61(6), pp.1715-1727.

Burgmann, R., Rosen, P.A., Fielding, E.J., 2000. Synthetic Aperture Radar Interferometry to measure earth`s surface topography and its deformation. Annu. Rev. Earth Planet, Sci., Vol. 28, pp. 169-209.

Delaney, P.T., McTigue, D. F., 1994. Volume of magma accumulation or withdrawal estimated from surface uplift or subsidence, with application to the 1960 collapse of Kilauea Volcano. Bull. Volcano, Vol. 56, pp. 417-424.

Dixon, T.H., Mao, A., Bursik, M., Heflin, M., Langbein, J., Stein, R. Webb, F., 1997. Continuous monitoring of surface deformation at Long Valley Caldera, California, with GPS. Journal of Geophysics Research, Vol. 102, pp. 12017-12034.

Du, J., Olso, J.E., 2001. A poroelastic reservoir model for predicting subsidence and mapping subsurface pressure fronts. Journal of Petroleum Science and Engineering, Vol. 30, pp. 181-197.

Du, Y., Aydin, A., Segall, P., 1992. Comparison of various inversion techniques as applied to the determination of a geophysical deformation model for the 1983 Borah Peak earthquake, Bulletin of the Seismological Society America, Vol. 82, pp. 1840-1866

Dusseault, M.B., Collins, P.M., 2008. Geomechanics effects in thermal processes for heavy oil exploitation. CSEG Recorder, June, pp. 20-23.

Dusseault, M.B., Rothenburg, L., 2002. Analysis of deformation measurements for reservoir management. Oil & Gas Science and Technology, Vol. 57 (2), pp. 539-554.

Fialko, Y., Simon, M., 2000. Deformation and seismicity in the Coso geothermal area, Inyo County, California: Observations and modeling using satellite radar interferometry. Journal of Geophysical Research, Vol. 105, pp.21, 781-21,794.

Goldberg, D.E., 1989. Genetic algorithms in search optimization and machine learning: Addison-Wesley Publ. Co.

Hermansen, H., Landa, G.H., Sylte, J.E., Thomas, L.K., 2000. Experiences after 10 years of waterflooding the Ekofisk field, Norway. Journal of Petroleum Science and Engineering, Vol. 26(1-4), pp. 11-18.

Hu, R.L., Yue, Z.Q., Wang, L.C., Wang, S.J., 2004. Review on current status and challenging issues of land subsidence in china. Engineering Geology , Vol. 76, pp. 65-77.

JACOS, 2009. Hangingstone Demontration Project 2008: Thermal In-Situ Scheme Progress Report, Approval No. 8788G, presented on March 23, 2009.

Jonsson, S., Zebker, H., Segall P., Amelung, F., 2002. Fault slip distribution of the 1999 Mw 7.1 Hector Mine, California, earthquake, estimated from satellite radar and GPS measurements. Bulletin of the Seismological Society of America, Vol. 92 (4), pp. 1377–1389.

Klees, R., Massonnet, D., 1999. Deformation measurements using SAR interferometry: potential and limitations. Geologie enMinjbouw, Vol.77, pp. 161-176.

Mathieson, A., Wright, I., Roberts D., Ringrose, P., 2009. Satellite imaging to monitor CO2 movement at Krechba, Algeria. Energy Procedia. Vol. 1, pp. 2201-2209.

Menke, W., 1984. Geophysical Data Analysis: Discrete inverse theory. Academic Press Inc.

Mogi, K., 1958. Relations between the eruptions of various volcanos and the deformations of the ground surfaces around them. Bull. Res. Inst. Tokyo, Vol. 36, pp. 99-134.

Nagel, N.B., 2001. Compaction and subsidence issues within the petroleum industry: from Wilmington to Ekofisk and beyond. Phys. Chem. Earth, Vol. 26, No. 1-2, pp. 3-14.

Nunnari, G., Puglisi, G., Guglielmino, F., 2005. Inversion of SAR data in active volcano areas by optimization techniques. Nonlinear Processes in Geophysics, Vol. 12, pp. 863-870.

Okada, Y., 1985. Surface deformation due to shear and tensile faults in a half space. Bulletin of the Seismological Society America, Vol. 75, pp. 1135-1154.

Oppliger, G., Mark, C., Shevenell, L., Taranik, J., 2005. Elucidating deep reservoir geometry and lateral outflow through 3-D elastostatic modeling of satellite radar (InSAR) observed surface deformations: An example from the Bradys geothermal field. GRC Transaction, Vol. 29, pp. 419-424.

Patzek, T.W., Silin, D.B., 2000. Use of INSAR in surveillance and control of a large field project. Lawrence Berkeley National Laboratory.

Patzek, T.W., Silin, D.B., Fielding, E., 2001. Use of satellite radar images in surveillance and control to two giant oilfields in California. SPE Annual Technical Conference and Exhibition, New Orleans, 30 September-3 October.

Simons, M., Rosen, P. A., 2007. Interferometric Synthetic Aperture Radar Geodesy. Treatise on Geophysics..

Teatini, P., Gambolati, G., Ferronato, M., Settari, A., Walters, D., 2011. Land uplift due to subsurface fluid injection. Journal of Geodynamics, Vol. 51, pp. 1-16.

Yang, X.M., Davis, P.M., Dieterich, J.H., 1988. Deformation from inflation of a dipping finite prolate spheroid in an elastic half-space as a model for volcanic stressing. Journal of Geophysical Research, Vol. 93, pp. 4249-4257.

Chapter 6

Summary and Future Work

6.1. Summary

Subsidence due to excessive groundwater extraction in Bandung Basin has been estimated by using synthetic aperture radar (SAR) interferometry (i.e., two-pass repeat differential InSAR and interferometric point target analysis). The amount of the subsidence is more than 45 cm for the period of 4 years since March 1, 2007. The maximum rate of subsidence is about 12 cm/year for the period. Areas that have experienced larger subsidence are associated with industrial regions. Significant subsidence has also occurred in urban areas with dense population. It is assumed that in these regions much amount of groundwater has been consumed for their activities.

Characterization of Bandung subsidence has been carried out by using SAR interferometry based on the geological point of view. In general, the subsidence has occurred in the central depression zone of the basin consisting of alluvial and lake deposits. For most of areas over the Bandung basin subsidence patterns are consistent with the distribution of production wells and the decrease of groundwater level. However, they are not consistent, especially in areas comprising the consolidated bedrock even though aquifer had damages. The subsidence expansion over the Bandung Basin is also controlled by geological structure such as different type of rocks at several areas. Based on the trend of non-linear displacement estimated by using interferometric point target analysis, the characteristic of subsidence is influenced by seasonal changes. Slow subsidence occurred during the dry season, and contrarily the subsidence has been accelerated by recharge process during wet season.

InSAR processing technique for strong noise data has been successfully improved to estimate surface heave at small area of oil sands field. Coregistration of PALSAR intensity with the Landsat ETM+ intensity with higher accuracy than that

with the simulated SAR intensity has been performed in the lookup table refinement. The accuracy is less than a half pixels using the Landsat image so that the topographic phase can be properly removed from the interferograms. Based on the evaluation and comparison of three filtering methods by using three criteria, Li's filter is the most suitable filtering methods to reduce noises presenting over differential interferograms, especially for strong noises due to several decorrelation effects. Surface heave rate of 3.6 cm/year at oil sands field related to steam injection (SAGD) has been accurately estimated by stacking differential SAR interferometry. The pattern of the heave obtained from InSAR technique is a good agreement with that from the network of 54 monument surveys.

The proposed geomechanical inversion scheme to estimate the distribution of oil sands reservoir deformations and volume changes has been successfully performed. The first step, we applied the genetic algorithm for estimating the rough reservoir deformation based on the data of surface heave. The result shows that the depth of the target reservoir is in good agreement with the injected point at borehole. In the second step, we applied the penalty function technique in the least square inversion with the smoothing factor to estimate the best solution. Based on this technique, the vertical deformation distribution is in good agreement with the well pair configuration. Finally, we estimated the total volume change rate of 150,809 m^3 a year that corresponds with the growth of the steam chambers.

6.2. Future work

In this study we have successfully applied the SAR interferomety technology for estimating and analyzing the characteristics of surface deformation. Moreover, we have also performed the technology by combining with inversion technique to estimate the deformation and volume changes in oil sand reservoir. However, we need to more explore the potential of the SAR interferometry in order to analysis of reservoir characteristics by means of geomechanical model and fluid flow simulation.

Another future work is to apply the SAR interferometry technique for other natural disasters, such as landslide, earthquake, volcano eruption, mudflow etc.

Ph.D. Dissertation

Synthetic Aperture Radar Interferometry for Natural Disaster and Reservoir Monitoring

Mokhamad Yusup Nur Khakim

Laboratory of Engineering Geology
Department of Civil and Earth Resources Engineering
Kyoto University

Kyoto University, Room C1-1-118
Kyotodaigaku-Katsura, Nishikyo-ku, Kyoto, 615-8540, Japan

myusup_nkh@earth.kumst.kyoto-u.ac.jp